Thermoresponsive Artificial Cell Clusters

Formation and Dynamics of Dense Lipid Vesicle Populations in Temperature Gradients

Maivizhi Thiyagaraja

Thesis submitted for the degree of
Master of Science in Chemistry
60 credits

Department of Chemistry
Faculty of Mathematics and Natural Sciences

UNIVERSITY OF OSLO

June 2022

Thermoresponsive Artificial Cell Clusters

Formation and Dynamics of Dense Lipid Vesicle Populations in Temperature Gradients

Maivizhi Thiyagaraja

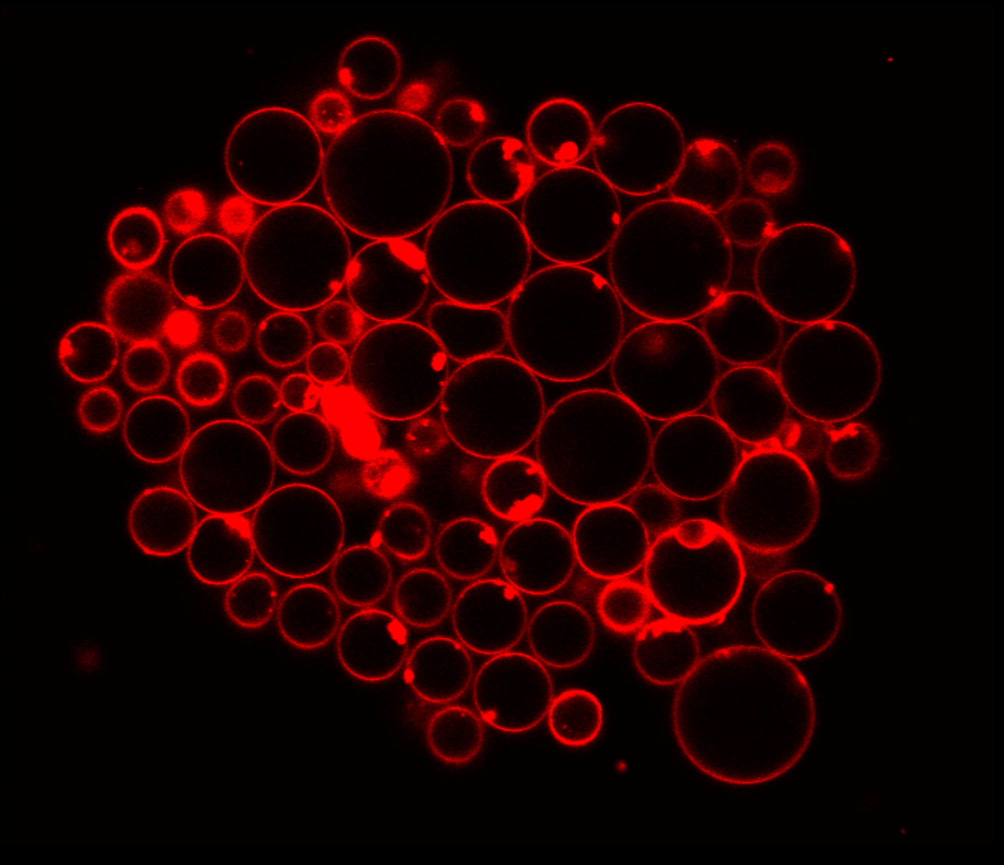

2022

Thermoresponsive Artificial Cell Clusters

Maivizhi Thiyagaraja

http://www.duo.uio.no/

Print: Reprosentralen, University of Oslo

Abstract

Artificial cells are built to mimic the characteristics of biological cells. They are applied in different fields of bionanotechnology and can be used to study fundamental problems in cell biology and early evolution. I applied a bottom-up engineering approach to build phospholipid-based model artificial cell compartments to study potential collective behavior among primitive cell compartments. In order to generate the lipid compartments, I employed continuous Droplet Interface Crossing Encapsulation (cDICE), a microfluidics-based technique known for generating giant lipid vesicles with efficient encapsulation of macromolecules with high-throughput. A key part of my thesis was encapsulating a synthetic thermoresponsive polymer inside these lipid compartments, Poly (N-isopropylacrylamide) (PNIPAAm), to study intra- and intercellular response of the vesicles containing the polymer in an environment with altering temperatures. The thermal stimulus was applied via an IR-B-laser to create a localized temperature gradient. Thermal manipulation of vesicle populations, both with and without PNIPAAm, induced their self-organization into dynamic clusters. PNIPAAm prolonged the adhesion between the vesicles in the clusters.

Preface

First and foremost, I would like to thank my supervisor, İrep Gözen, for her guidance, encouragement, and support throughout this master's project. I feel very fortunate to have gotten the opportunity to work in your lab and I am grateful for everything I have learned from you. Working on this project has been an often challenging, but immensely educational and gratifying experience.

Thanks to all my coworkers, both current and former members of Softlab Norway; Aysu, Ingrid, Jicheng, Lin, Inga and Karolina, for their company and help these last two years. I have much appreciated the friendly and collaborative work environment. I would like to give a special thanks to Ingrid for helping me with the silanization and spin coating, Lin for helping me with the IR-laser and my office mate Jicheng for all the interesting discussions.

I would also like to thank the engineers from I-lab; Hans Borg, Simen Kristiansen and Anthony Olsrud-Hansen, for their help with the experimental set-up for cDICE.

I express my gratitude to my sister, Vanathi Thiyagarajah, for proofreading the thesis.

Finally, I would like to thank my family and close friends for their love, encouragement and emotional support throughout this degree. I could not have done this without you all.

Thank you.

Maivizhi Thiyagaraja

Oslo, June 2022

Table of Contents

Abbreviations

2D	Two-dimensional
3D	Three-dimensional
ATP	Adenosine triphosphate
BM	Bénard-Marangoni
cDICE	continuous Droplet Interface Crossing Encapsulation
CGC	Critical gel concentration
DI	Deionized
GUV	Giant unilamellar vesicle
LCST	Lower critical solution temperature
IAS	Inner aqueous solution
ID	Inner diameter
IR	Infrared
LOS	Lipid-in-oil solution
LSCM	Laser scanning confocal microscopy
LUV	Large unilamellar vesicle
MLO	Membraneless organelle
OAS	Outer aqueous solution
OD	Outer diameter
PC	Phosphatidylcholine

PDMS	Polydimethylsiloxane
PE	Phosphatidylethanolamine
PEEK	Polyether ether ketone
PNIPAAm	Poly(N-isopropylacrylamide)
POPC	1-palmitoyl-2-oleoyl-*sn*-glycero-3-phosphocholine
PTFE	Polytetrafluoreten
RB	Rayleigh-Bénard
RBM	Rayleigh-Bénard-Marangoni
ROI	Region of interest
SUV	Small unilamellar vesicle

1 Introduction

1.1 Artificial Cells

Artificial cells can be defined as systems built to mimic the structural and/or functional characteristics of a biological cell, by the use of natural and synthetic chemical components[1, 2]. The first artificial cell was developed by the Canadian physician and scientist, Dr. Thomas Ming Swi Chang, in 1957[3]. He encapsulated hemoglobin and red blood cell enzymes in synthetic polymer membrane-based artificial cells. The purpose was to develop red blood cell substitutes that could be used in medicine and other areas of research. Even though the first artificial cell was created 65 years ago, it is only in the last 25 years, with the advancements in nanotechnology and material science, that the research on artificial cells has grown[4]. The ultimate goal of this field of research is to create "living" artificial cells that can perform minimal and/or pre-programmed cellular functions[5]. Although this goal is not expected to be reached in the nearest future, artificial cells are currently used to study fundamental problems in cell biology and early evolution, and serve as promising tools in various fields of biotechnology, such as biomedicine and agriculture[2].

There are two approaches in the engineering of artificial cells – the top-down approach and the bottom-up approach (**Figure 1**).

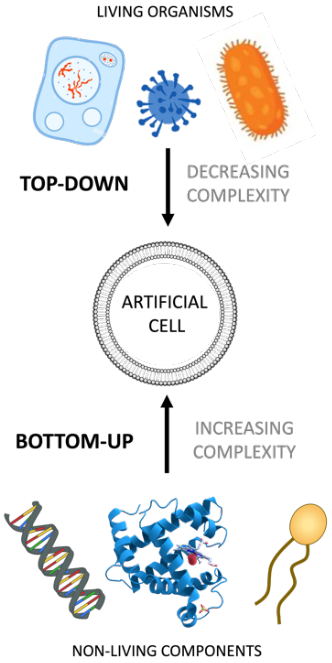

Figure 1: The two different strategies for the design of artificial cells: top-down and bottom-up.

The top-down approach involves living cells, the complexity of which are reduced by replacing or knocking out the genes of the cell. Various experimental and computational methods have been used to attempt defining a minimal number of protein-encoding genes in different bacterial species[6]. In one such study, transposon mutagenesis of *Mycoplasma genitalium* suggested that 265-350 of its 480 protein-encoding genes were essential for survival of the cell[7]. One of the drawbacks of this method is that genes that tolerate transposon insertions might be overlooked[8]. Inactivation of non-essential genes using antisense RNA to inhibit gene expression, identified 150 essential genes of the human pathogen *Staphylococcus aureus*[9]. However, this method is limited to the genes that contribute to sufficient expression of the inhibitory RNA[8]. Due to the limitations of these methods, top-down approaches have not yet fully managed to define the minimal number of cellular features necessary to create a living artificial cell from scratch[5]. The idea of altering the genome, which would supposedly lead to the cell displaying new or modified functions, led to the development of gene engineering technology. The first gene-modified organism that successfully expressed genetic sequences from a different species, was reported by Cohen et al. in 1978, when they transferred the DNA sequences coding for mouse dihydrofolate reductase into bacteria[10].

In the bottom-up approach, the starting point is non-living components which assemble to create a system of increased complexity[2]. Creating artificial cells from bottom-up is a challenging task, but the model artificial cells are structurally simpler, easier to work with and their molecular composition can be controlled with high precision. This allows us to incorporate only the key components required for specific functions, opening up for the investigation of single features of biological cells in less complex environments[2]. In a study by Loiseau et al.[11], actin filaments and the cross-linking protein anillin were encapsulated and utilized to reconstruct a cytoskeletal network inside lipid-based artificial cells. They also added Myosin II filaments to the mixture and observed shape remodeling and blebbing of the vesicles[11]. This is one example of the type of studies being done at the present, which expands our knowledge on the fundamental mechanics of cells.

As previously mentioned, one of the major objectives of artificial cell studies, is to make minimal, life-like systems that can be predicted and controlled with high accuracy[5]. The process of constructing a "living" artificial cell from bottom-up, would involve creating a protocell *de novo*. Protocell is the term used for the hypothetical precursor of the first biological cells. In the field of the origin of life, scientists use the bottom-up approach to make protocells. Through this work, they try to identify the key components and steps required for transition to life. In order to survive, the protocell should possess essential features of living cells, such as compartmentalization, metabolism, replication and division[2, 5]. The successful engineering of such an artificial cell could help provide a plausible theory for the origin of life, as well as provide information on the fundamental functions required for life and behavior of modern biological cells[12]. Despite the advancements in the field and many groups and consortia working towards this goal, an artificial cell made from non-living components that is capable of self-reproduction has not yet been observed, and is currently considered to be quite far from our reach[2].

For biomedical applications, artificial cells that only simulate one or a few specific features of natural cells, such as morphology, surface characteristics or a few functions are engineered[2]. Surface modification of polymersome-based drug delivery vehicles with target-specific antibodies, is an example of cell-mimicry in biomedicine, and has become popular in cancer therapy research due to the targeted delivery of drugs in a safe and effective manner[13]. Many of the conventional techniques, such as chemotherapy, radiotherapy and surgical removal of the cancer tissue, lack target specificity and harm the healthy cells surrounding the tumor[13]. Similarly, the delivery of therapeutic and diagnostic agents to the brain for the treatment of brain cancer is particularly challenging, due to the blood-brain barrier. Polymersomes conjugated with antibodies such as transferrin and lactoferrin, has been shown to cross the blood-brain barrier, and enhance the transport of drugs into brain tissue[14].

1.2 Collective Behavior in Artificial Cell Populations

Advancements in single synthetic cell research, and creation of functionalized artificial cells, have motivated the construction of higher-order artificial cell structures[15]. The bottom-up engineering of artificial multicellular systems that can potentially exhibit collective behavior is a major challenge in synthetic biology[16]. In multicellular organisms, the cells comprising tissues communicate and cooperate to exhibit self-organizing collective behavior[17, 18]. Self-organization and collective behavior are examples of emergent properties of complex systems and are found at different scales in nature[18]. At the cellular level, collective behavior is observed in the processes of morphogenesis, wound healing, and tumor growth within eukaryotes, and in quorum sensing in bacterial colonies[19]. At the macrolevel, it is seen among groups of animals and is present in flocks of birds, herds of sheep and schools of fish[20]. Emergent behaviors are not evident in the individual components in isolation and are hard to predict since the physical principles governing the macrostate are absent in the underlying microstate[18]. They are ruled by the interplay between the physical principles at the different levels of biological complexity, which is why understanding the characteristics of large interacting systems at the population-scale is a central problem in biology[20].

Self-organizing collective behavior on a population-scale of synthetic cells, can in principle be achieved by implementing intercellular communication via feedback loop controlled chemical reaction networks[16] or by application of external stimuli[21]. Self-organization is a process driven by energy dissipation and makes the system enter an ordered out-of-equilibrium state[21]. It is distinctive from self-assembly, which is a spontaneous process driven by minimization of free energy that leads the system towards thermodynamic equilibrium[18]. In self-organizing systems, involving chemical reaction networks, energy is consumed through fuel-to-waste conversion, typically in the form of ATP hydrolysis. The ordered, metastable structure will spontaneously disintegrate once the fuel has been consumed and return to its equilibrium state. Disintegration is prevented only by an infinite consumption of energy[21].

1.2.1 Intercellular Communication-Induced Self-Organization

In a recent example, intercellular communication-induced spatial self-organization of mouse L929 fibroblast cells was achieved by applying the synthetic notch (synNotch) juxtacrine signaling platform[22] (**Figure 2a**).

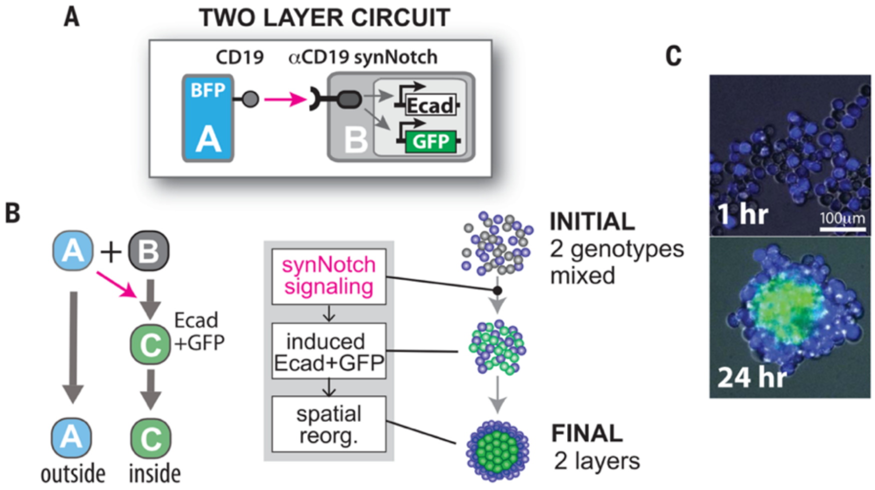

Figure 2: Intercellular communication-induced self-organization of a binary population of fibroblast cells achieved by applying the synNotch signaling circuit[22].

When the synNotch transmembrane receptor binds to its cognate ligand on an adjacent cell, it undergoes cleavage at the transmembrane domain. This causes the release of the intracellular transcriptional domain, which enters the nucleus, and stimulates the expression of specific genes. Different synNotch circuits were engineered with the following transcriptional outputs: expression of specific cadherin molecules that lead to homotypic adhesion between cells, differential gene expression or new synNotch ligands. A two-layer multicellular structure was formed by a binary cell population consisting of A-type cells expressing CD19 ligands and blue fluorescent protein, and B-type cells expressing the cognate anti-CD19 synNotch receptor, which when activated led to the expression of E-cadherin and GFP (C-type) (**Figure 2b**). Co-culturing of the two populations induced the expression of E-cadherin and GFP, generating adhesion between the C-type cells and formation of a two-layer structure (**Figure 2c**)[22].

Although progress has been made in gene-modified cells, self-organization induced by intercellular communication has not yet been achieved with artificial cells generated from the bottom-up. Microfluidics, 3D droplet printing[23], acoustic traps[24] and optical tweezers[25] are a number of the methods that have been utilized to control the spatial organization of artificial cells. In order to drive a signaling pathway like the synNotch circuit in the example above, and maintain the multicellular structure, energy is required in the form of ATP. The synthesis of biological polymers, like most life processes, are energy dissipative processes dependent on ATP hydrolysis and regeneration[26, 27]. Continuous regeneration of ATP without the accumulation of inorganic phosphates is a critical problem in cell-free expression systems[28]. Overcoming this issue can provide bottom-up artificial cells the tools to mimic the complex structures of cells and sustain out-of-equilibrium behavior[27].

1.2.2 External Stimuli-Induced Self-Organization

An alternative way of generating self-organization, that does not involve chemical fuel, is by the presence of an external stimulus, such as electric or magnetic fields[21]. Magnetotaxis in magnetotactic bacteria is an example on field-driven collective behavior found in nature. Magnetotactic bacteria are found in freshwater and marine habitats, and have organelles called magnetosomes that contain magnetic nanoparticles. The magnetosomes provide the cell a permanent magnetic dipole moment and force the swimming bacteria to align along the magnetic field lines of the Earth[29].

Magnetic field-driven self-organizing collective behavior of artificial cell populations made from bottom-up, was very recently demonstrated by Li and coworkers[30]. A stainless-steel (SS) mesh with patterned microwells was placed on top of a permanent magnet. This stimulated a paramagnetic response in the SS mesh. The interplay between the magnetic field from the SS mesh and vertical external magnetic field from the permanent magnet generated magnetic field gradient microenvironments. When sucrose-containing GUVs with paramagnetic $MnCl_2$ in the ambient solution, were deposited on the SS mesh, they aggregated into tissue-like colonies in the microwells, as shown in **Figure 3**. The structures were maintained even when the magnetic field was removed and disintegrated when being mechanically disrupted. This is a rare example of self-organization in bottom-up artificial cell populations. The formation of spatially organized lipid vesicle-based artificial cell structures that are able to communicate and maintain their out-of-equilibrium state, remains a great challenge[30].

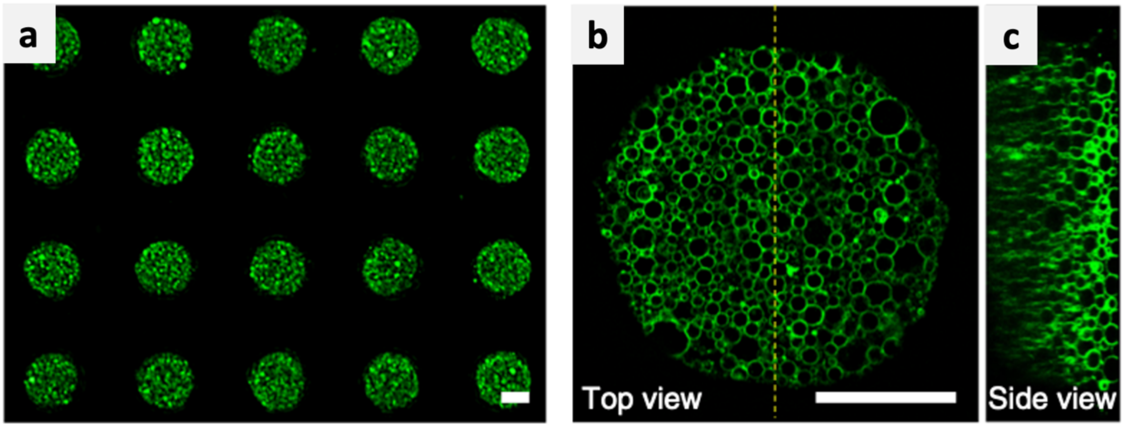

Figure 3: (a) Magnetic field-driven organization of multicellular artificial cell structures on a stainless-steel mesh with patterned microwells with diameter of 250 µm[30]. (b) Top- and (c) side view of a single microwell. Scale bars are 100 µm. Adapted with permission[30]. Copyright 2020, Springer Nature Limited.

Thermal manipulation of artificial cell populations as a way of driving self-organization, is a largely unexplored area in the field of synthetic biology. Many artificial cell models with thermoresponsive abilities have been generated[31-33], but to the best of our knowledge they have not been used as a means of inducing collective behavior. In a study by Gobbo and coworkers, artificial tissue-like structures were assembled from a binary population of thermoresponsive proteinosomes[34] (**Figure 4**). The proteinosomes constituting the spheroids exhibited collective reversible contraction when heated above the lower critical solution temperature (LCST) of the thermoresponsive polymer. However, the spheroid formation and interactions between the proteinosomes, was due to chemical coupling and not a consequence of physicochemical interactions[34].

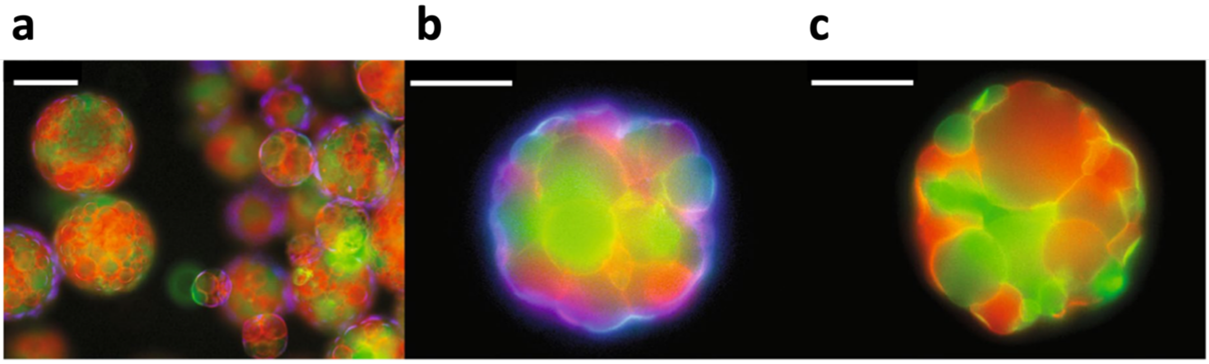

Figure 4: Multicellular structure formed by thermoresponsive proteinosomes. The tissue-like structure is formed by chemical coupling between the proteinosomes and exhibits reversible contraction[34]. (a) Multiple proteinosome-based tissue-like structures. (b) Caged spheroid with an outer proteinosome membrane (blue). (c) Uncaged spheroid. Scale bars in a, b and c are 100, 50 and 50 µm, respectively. Adapted with permission[34]. Copyright 2018, Springer Nature Limited.

1.3 Giant Unilamellar Vesicles (GUVs)

Some of the most established model systems for artificial cells are coacervates, polymersomes, proteinosomes, colloidosomes and giant unilamellar vesicles[12]. The latter is the most common model system for artificial cells made from the bottom-up, and is the model used in this thesis. A giant unilamellar vesicle (GUV) is a closed spherical lipid bilayer with an aqueous core (**Figure 5a**).

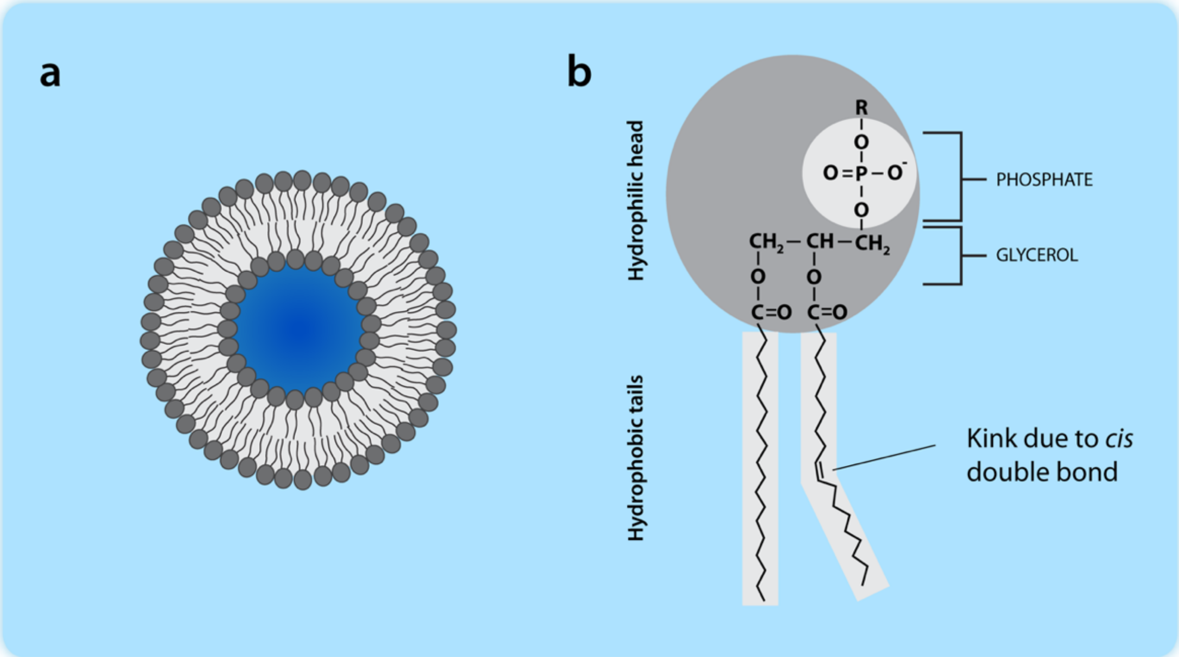

Figure 5: (a) Schematic drawing of a GUV, which is a closed spherical lipid bilayer with an aqueous core. (b) Molecular structure of a phospholipid molecule.

Lamellarity refers to the number of bilayers the vesicle is composed of, where unilamellar vesicles have a single bilayer membrane and multilamellar vesicles have several bilayers. Unilamellar vesicles are classified as small (SUV) when their diameter is <100 nm, large (LUV) when the diameter is 100-1000 nm and giant when their diameter is >1 µm. SUVs and LUVs are primarily used in biomedical applications, such as drug delivery. For artificial cell studies, GUVs are employed, as their size is comparable to that of eukaryotic cells; animal cells are on average 10-30 µm and plant cells 10-100 µm[35]. The GUV membrane is composed of phospholipids, which are the main constituents of biological membranes in all living organisms. They are therefore a commonly used tool in basic research of biomembranes. Phospholipid membrane-based artificial cells are capable of exchanging molecules with the external environment, are biocompatible and can accommodate membrane proteins more easily than the other model systems[36]. The biocompatibility and similarity of structural features between GUVs and natural cells makes them perhaps the most favorable model system for artificial cells[12].

Phospholipids are amphiphilic molecules with a hydrophobic non-polar hydrocarbon tail and hydrophilic polar phosphate head-group (**Figure 5b**). The amphiphilic nature of these molecules makes them subject to the hydrophobic effect in the presence of water[37]. Thanks to their polarity, water molecules in liquid phase form hydrogen bonds between adjacent hydrogen and oxygen atoms. Each water molecule can form up to four neighboring water molecules, creating a hydrogen bonding network. The non-polar hydrocarbon chains of the phospholipids are unable to form hydrogen bonds with the water molecules. When lipid molecules are dispersed in water, the hydrogen bonding network between water molecules becomes disrupted. This causes the water molecules surrounding the non-polar hydrocarbon chains to form a structured water "cage" around the hydrocarbons. The ordered state of the water molecules decreases the entropy of the system. To increase the entropy, and disrupt less hydrogen bonds, the lipid molecules will self-assemble into ordered structures, such as micelles or liposomes, where the hydrophobic tails are facing away from the water. This way, there are less water molecules in an ordered form, and the entropy of the system is increased[38].

The formation of a stable lipid bilayer and thus vesicle, is governed by the effective geometrical shape of the lipid molecules. The shape of the lipids determines the morphology of the self-assembled structure, which is described by the molecular packing parameter, P. The packing parameter is defined as

$$P = \frac{v_o}{a l_o}$$

where v_o is the volume of the tail(s), l_o the length of the tail(s) and a the surface area of the head group. Lipids with similarly sized head and tails are cylindrical with $P = 1$. They form planar bilayers, while lipids with conical shape can form micelles and lipids with inverted conical shape can form inverted micelles (**Figure 6**)[38].

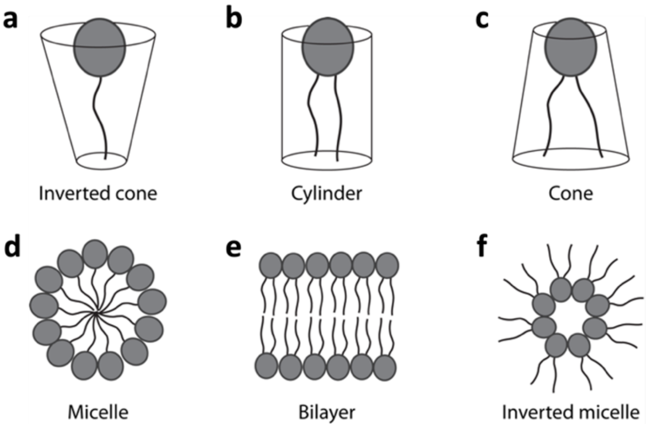

Figure 6: (a-c) The various geometries of lipid molecules and (d-f) their corresponding self-assembled structures.

The phospholipid bilayer membrane functions as a hydrophobic barrier between two aqueous environments, providing protection for the internal components of the vesicle, while still permitting exchange of specific molecules[37]. This property is known as selective permeability and is vital to the existence of biological cells. The hydrophobic nature of nonpolar molecules, such as hydrocarbons, CO_2 and O_2, enables them to dissolve in the hydrophobic interior of the lipid bilayer and cross it easily, without the assistance of membrane proteins. In contrast, the direct crossing of hydrophilic molecules, such as ions and polar molecules, is hindered by the hydrophobic barrier. When the concentration of a solute, that cannot pass through the membrane, is different inside the vesicle compared to the outside, free water will diffuse across the selectively permeable membrane. This process is called osmosis and leads to water moving from the environment of lower to higher solute concentration[17].

Another important property of the phospholipid membrane is fluidity. The fluidity of the lipid bilayer depends on the membrane composition, molecular structure of the phospholipids and the temperature[37]. Introduction of cis carbon-carbon double bonds in the hydrocarbon tails of the phospholipids generates ‘kinks’ in the tails where the double bonds are located (**Figure 5b**). Due to the kinks, phospholipids with unsaturated hydrocarbon tails cannot pack together as closely as the ones with saturated hydrocarbon tails, giving raise to increased fluidity of the membrane. The membrane fluidity also increases with increasing temperature. A membrane rich in unsaturated phospholipids will therefore remain fluid at a lower temperature compared to a membrane with saturated lipids[17, 37].

1.4 Objective of Thesis

The aim of this thesis is to use a bottom-up approach for the engineering of phospholipid-based artificial cell populations, to study their internal and intercellular/vesicular dynamics. I will encapsulate a thermoresponsive polymer, PNIPAAm, to manipulate the artificial cells by temperature. PNIPAAm is a water-soluble synthetic polymer with a lower critical solution temperature (LCST) at 32 ℃. When heated above this temperature, PNIPAAm transitions from sol to gel phase. There have been studies on single vesicles, where PNIPAAm sol was encapsulated through microinjection[39] and electroformation[40]. The contraction of the internalized polymer and phase separation inside the vesicles were observed. I aim to use a different approach to study the dynamics of PNIPAAm-encapsulated vesicles, by using the microfluidics-based technique termed “continuous Droplet Interface Crossing Encapsulation” (cDICE). It is known for its high encapsulation efficiency and high throughput generation of giant unilamellar vesicles. An integral part of this thesis work was to build and optimize the set-up for cDICE. By generating a spatially confined population of thermoresponsive GUVs instead of single vesicles, we aim to study collective behavior.

Specific scientific goals:

- Build the instrument for continuous Droplet Interface Crossing Encapsulation (cDICE)
- Achieve bottom-up construction of artificial cell populations that encapsulate PNIPAAm
- Locally apply heating by using an IR-B laser to enable the phase transition of PNIPAAm encapsulated in the artificial cells
- Provide a comparison of behavior of basic artificial cell populations to the thermoresponsive artificial cells

2 Materials and Methods

2.1 Methods for Generation of GUVs

There are various techniques to create GUVs based on rehydration of lipid films or on microfluidics. I employ a microfluidics-based technique called “continuous Droplet Interface Crossing Encapsulation” (cDICE). In this section, I will briefly discuss some of the different methods used for generation of GUVs, their advantages and drawbacks, describe the cDICE method in detail and discuss why cDICE has been selected among these methods.

2.1.1 Gentle Hydration

Gentle hydration is one of the most established and most commonly utilized techniques for generation of GUVs and is based on swelling of a lipid film in aqueous media[41]. It is an inexpensive method that relies on simple equipment. The lipid film is formed by evaporating the organic solvent of a lipid solution at reduced pressure. The lipid film is then rehydrated with an aqueous buffer, which leads to the swelling of the film over time and formation of vesicles, as illustrated in **Figure 7**. The resulting vesicle suspension contains both uni- and multilamellar vesicles of varying size.

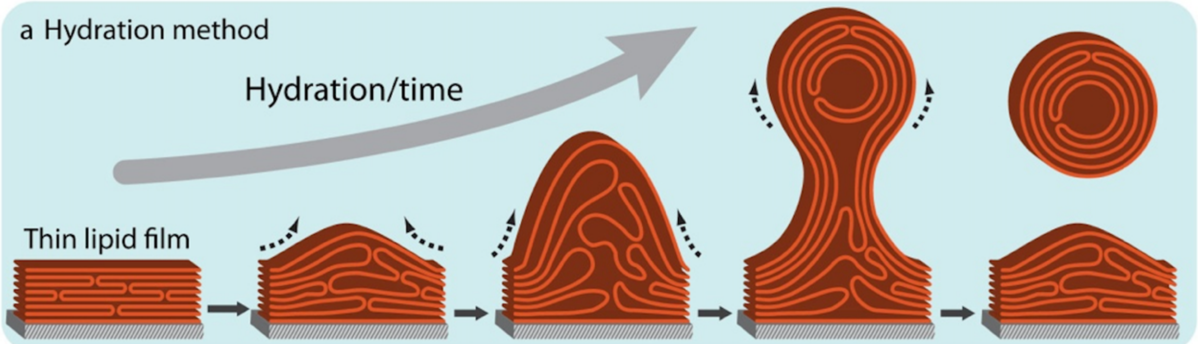

Figure 7: Gentle hydration method for the formation of GUVs. A thin lipid film is rehydrated with an aqueous buffer that initiates the swelling of the film and formation of vesicular structures. Adapted with permission[42]. Copyright 2022, Wiley-VCH GmbH.

2.1.2 Electroformation

Electroformation is another method based on hydration of lipid films, but involves application of an external electric field to facilitate the separation and bending of the bilayers (**Figure 8**)[43]. Briefly, the lipid solution is deposited on the electrodes and application of the electric field is initiated to facilitate swelling and let run for a couple of hours[44, 45]. The protocols for electroformation are straight-forward and require minimal specialized equipment. The method produces a high number of vesicles with various lamellarity and broad size distribution[46].

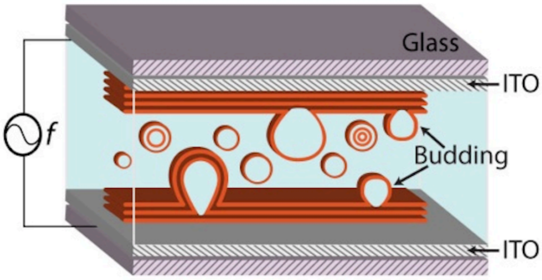

Figure 8: Electroformation method for formation of GUVs. An electric field is applied to promote vesicle formation. Adapted with permission[42]. Copyright 2022, Wiley-VCH GmbH.

2.1.3 Microfluidic Double Emulsions

Droplet-based microfluidic technologies are becoming more widespread in synthetic biology and material science applications. They are recognized for their ability to make GUVs with high-throughput generation, high monodispersity, narrow size distribution and superior encapsulation efficiency[1]. The microfluidic generation of water-in-oil-in-water (w/o/w) double emulsion droplets, followed by solvent extraction, is another method used to make GUVs[47]. The two-step emulsification process can be done in microfluidic chips made of polydimethylsiloxane (PDMS) or in glass microcapillaries. In the first step, droplets of aqueous solution are injected into an organic solvent, generally toluene or chloroform, containing solubilized lipids. The lipids form a monolayer around the aqueous droplets, which are then injected into the outer aqueous solution. In the second step, the solvent trapped in between the monolayers evaporates, over a timeframe of several hours, and the phospholipids form a bilayer (**Figure 9**)[1].

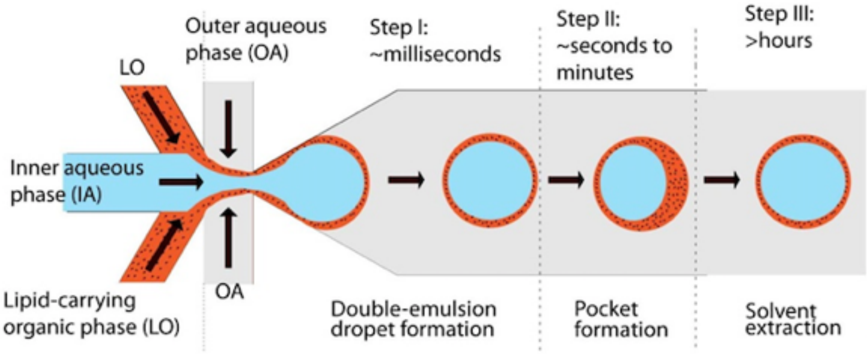

Figure 9: Microfluidic double emulsion. Adapted with permission[48]. Copyright 2016, Springer Nature Limited.

2.1.4 Microfluidic Jetting

Microfluidic jetting based on pulsed jet flow, is one of the more advanced microfluidic methods[49]. Two aqueous phases lined by a monolayer of phospholipids are in contact inside an organic phase containing dissolved phospholipids. The area of contact at the interface of the phases has a planar lipid bilayer[45], as seen in **Figure 10**. A piezoelectricity-driven jetting device jets an aqueous liquid against the bilayer, inducing membrane deformation and formation of a GUV. The bilayer at the interface between the aqueous phases remains intact after the vesicle is formed[49].

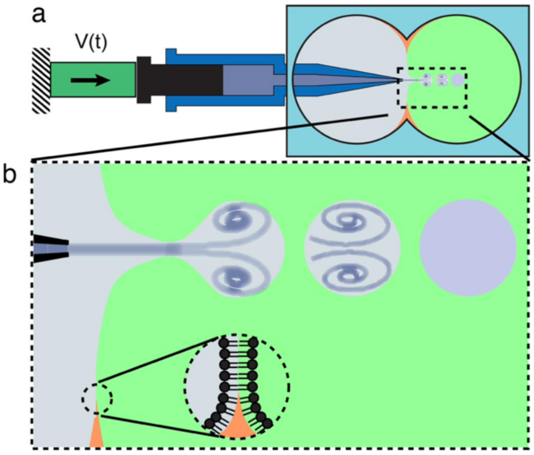

Figure 10: Microfluidic jetting. Reused with permission[49]. Copyright 2008, National Academy of Sciences.

2.1.5 Continuous Droplet Interface Crossing Encapsulation (cDICE)

The method used for production of vesicles in this thesis is "continuous Droplet Interface Crossing Encapsulation" (cDICE), developed by Abkarian and coworkers in 2011[50]. It is a microfluidic method based on inverted emulsion transfer[47]. The set-up involves a cylindrical chamber with an opening hole on top and an injection capillary. Solutions of different densities are injected through the hole while the chamber is rotating at high speed. Due to the centrifugal force, the different liquids form vertical interfaces (**Figure 11**).

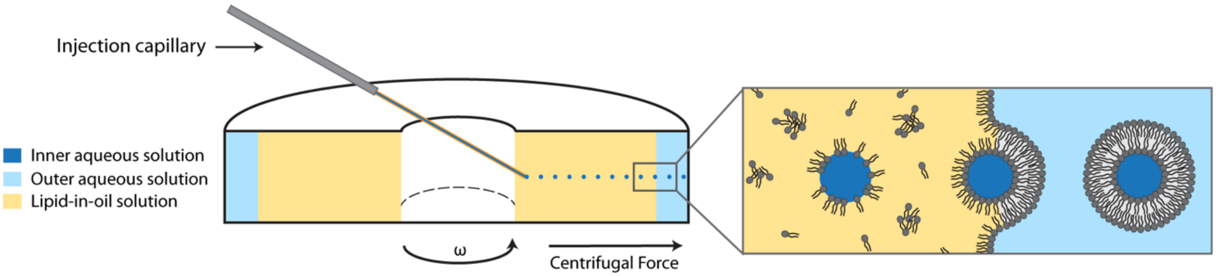

Figure 11: Principle behind the cDICE method. Adapted with permission[51]. Copyright 2021, American Chemical Society.

The outermost layer is an aqueous solution (OAS), followed by a lower density lipid-in-oil solution (LOS) closest to the center of the chamber. The capillary injects the inner aqueous solution (IAS) of the vesicle into the LOS. An alternative is to use a nonpolar solvent, such as decane, with even lower density than oil, as the medium in which the droplets form. The IAS is injected at constant pressure, and droplets drip off the capillary tip.

The centrifugal force drives the radial outward motion of these droplets perpendicular to the rotation axis. When an aqueous droplet reaches the LOS, lipids spontaneously assemble around it due to the hydrophobic effect. The droplet now surrounded by a lipid monolayer moves toward the interface between the LOS and the outermost aqueous solution, which is saturated with lipids. When the droplet crosses this interface, another monolayer forms around the droplet, resulting in a vesicle with a lipid bilayer membrane and an aqueous core containing the desired components[46, 52].

Droplet Formation

The configuration of droplet generation in cDICE is comparable to the geometry of a T-junction in microfluidic systems, as the dispersed phase (IAS) is injected into the continuous phase (LOS) orthogonally. Droplet formation in a T-junction depends on the flow rate of the two immiscible liquids. When the viscous forces overcome the IAS/LOS interfacial tension, droplets detach from the tip of the capillary. The ratio between the viscous forces and interfacial tension is described by the dimensionless parameter known as the capillary number, Ca, and is defined as

$$Ca = \frac{\mu V}{\sigma} \tag{2}$$

where μ is the dynamic viscosity of the medium in which the droplet is generated and V the velocity of this medium, and σ the interfacial tension between the two fluids. The viscous forces dominate when the capillary number is high ($Ca \gg 1$) while interfacial tension dominates at low capillary numbers ($Ca \ll 1$)[53].

There are three regimes for microfluidic droplet formation in a T-junction, depending on the relative flow rate of the two liquids: squeezing, dripping and jetting (**Figure 12**). Squeezing occurs at low capillary number, dripping at intermediate capillary numbers and jetting at high capillary numbers. Droplet formation by the dripping regime is the preferred mode for cDICE.

The droplet size is dictated by the capillary number and the diameter of the capillary. Spherical droplets form in the dripping regime, with droplet diameter increasing with decreasing Ca. With this method, the mean droplet-, thus vesicle size, is easily tuned by altering the relative flow rates of the continuous- and dispersed phase and/or changing the capillary size[50, 53].

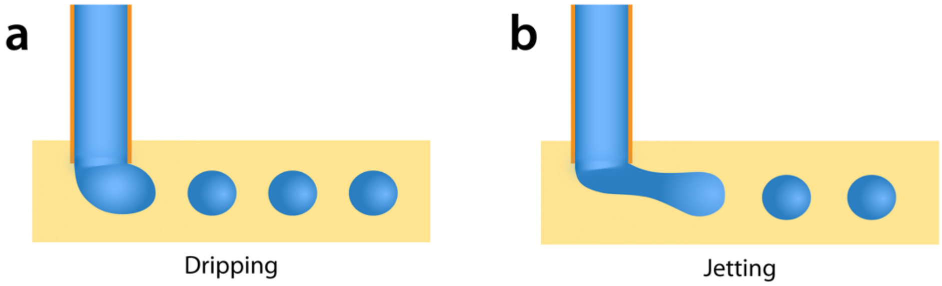

Figure 12: Droplet formation by the (a) dripping- and (b) jetting regimes.

We estimated the capillary number to be $Ca = 0.32$, using the physical properties of silicone oil and water, and the linear velocity of the LOS at the capillary tip ($r_0 \cdot \omega$), when the angular velocity (ω) is 1500 rpm (calculation in Appendix). As our LOS is a mixture of silicone oil with mineral oil and decane in the majority of the experiments, i.e. solvents with various viscosities, the capillary number might deviate from the value we determined. The study by Abkarian et al.[50], involves a much smaller capillary number ($Ca = 0.08$) than the one in our system (0.32). Both setups however lead to compatible droplet diameters. This is most likely due to the difference in the dimensions of the capillary needles utilized in these two studies. The capillary needle diameters used in the work by Abkarian et al. were 4, 6 and 13 µm leading to average droplet diameters of 8.9, 18 and 37 µm, respectively. We used capillaries with an inner diameter of 25 µm. Despite the higher capillary number in our work, average droplet diameters between 8 and 20 µm were observed.

Lipid Adsorption

After the droplets are formed, they move towards the edge of the chamber, driven by the centrifugal Force, F_c, that is expressed as

$$F_c = m\omega^2 r \tag{3}$$

where ω is the angular velocity, r the radius and m the mass of the object. The monolayer-formation on each droplet depends on the droplet flight time, τ_F, through the LOS layer. τ_F has to be longer than the time it takes for the surface of the droplet to become saturated with lipids, τ_S. Abkarian and coworkers[50] define the droplet flight time as

$$\tau_F = \frac{9\mu}{(2\Delta\rho R^2\omega^2)\ln\left(\frac{1+e}{r_0}\right)} \tag{4}$$

where μ is the dynamic viscosity of the LOS, $\Delta\rho$ the difference in density between the IAS and LOS, R the droplet radius, ω the angular velocity, r_0 the distance from the rotation axis to the capillary tip and e the distance the droplet has to travel through the LOS layer (**Figure 13**).

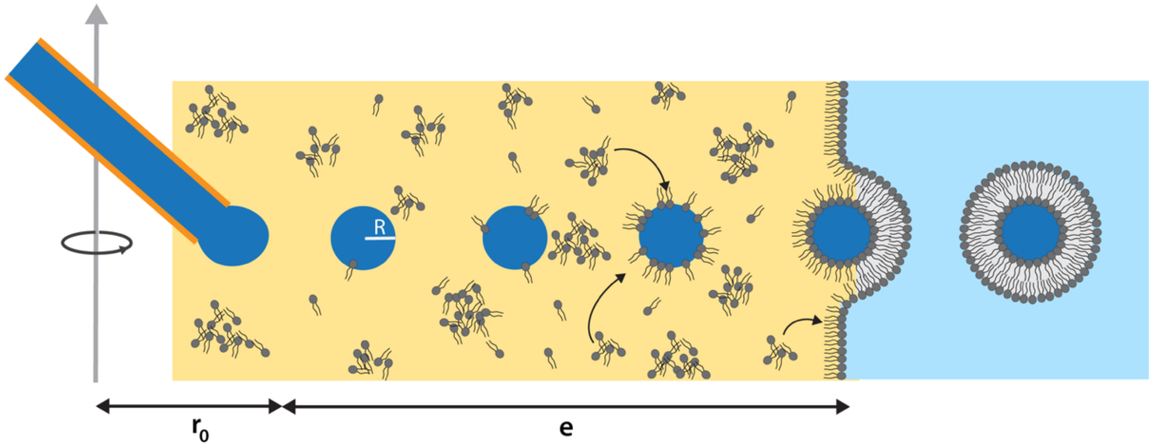

Figure 13: cDICE. Schematic depiction of r_0 and e in Equation (4). Adapted with permission[50]. Copyright 2011, The Royal Society of Chemistry.

The condition of $\tau_F \gg \tau_S$, sets an upper limit for vesicle size, as larger vesicles have lower τ_F. However, the set-up can be modified to make sure that the condition is met with certainty, permitting the formation of larger vesicles. Increasing the thickness of the LOS layer or increasing the lipid concentration, will increase the τ_F and decrease τ_S, respectively.

In our experimental set-up, the length of the different layers are approximately $r_0 = 10.5$ mm and $e = 6.5$ mm. Using a droplet radius of $R = 7.5$ µm (an average value acquired from the micrographs) and the angular velocity at 1500 rpm, the droplet flight time was estimated to be $\tau_F = 128\ s$ (calculation in Appendix). The adsorption time can be determined by pendant drop measurements[50]. For Egg PC lipids dissolved in mineral oil, $\tau_S \approx 20\ s$ at 0.5 mM lipids and $\tau_S \approx 50\ s$ at 0.25 mM lipids[50]. Although our LOS is composed of a mixture of various nonpolar solvents for most of the experiments, the aforementioned values of τ_S indicate that the condition $\tau_F \gg \tau_S$ is met in our system. The calculated value for τ_F also imply that for an injection time of 5 minutes, it is only the droplets formed in the first 3 minutes that are converted to vesicles.

Interface Crossing

When the droplets saturated with lipids cross the saturated oil-water interface, the monolayers are brought into contact, with the lipid tails facing each other, and zip together to form a small region of bilayer due to van der Waals interactions (**Figure 13**). The bilayer will grow by a zipping effect at the droplet/oil-water interface contact line[50, 54]. Ideally, there should be complete exclusion of the oil phase in between the monolayers, leading to oil-free bilayer membranes[54]. This situation corresponds to a low Bond number ($Bo \ll 1$). The Bond number relates the body forces to interfacial tension, and is

$$Bo = \frac{\Delta\rho a R^2}{\sigma} \tag{5}$$

where $\Delta\rho$ is difference in density between the two phases, a is the acceleration of the droplet, R the droplet radius and σ the interfacial tension[50]. Depending on the interaction between the lipid monolayers, there can be other outcomes than vesicle formation. The monolayers can rupture, causing the two aqueous liquids to mix, or the interfaces might repel each other. The zipping phenomena is governed not only by the nature of the lipids and fluids, but also the molecular density of the monolayers. The proper dispersion of lipids in the oil phase and fast renewal of the lipid monolayer at the oil-water interface, are therefore critical for efficient production of vesicles. The renewal of the monolayer is limited by the adsorption kinetics of the lipids dispersed in oil. In 2016, these issues were addressed by the research group of Massiera and co-workers, who are the inventors of the cDICE method. They developed a method to disperse lipids as aggregates in oil, which improved the stability of the suspension over time and the zipping of monolayers (**Figure 13**)[54]. This method is discussed further in Section 4.2.

2.1.6 Comparison of cDICE to Other Methods

The cDICE method is advantageous compared to the previously described methods for GUV generation. First of all, cDICE is an efficient way of producing monodisperse GUVs. Gentle hydration and electroformation fall short on this aspect. The poor control over exact vesicle size and lamellarity are some of the main drawbacks of both of these methods[42]. With cDICE, the vesicle size is easily tuned, and the encapsulation efficiency of macromolecules is high, and has been shown to support encapsulation of proteins and even red blood cells[50]. Moreover, the equipment is inexpensive and easy to set up and operate compared to pulsed jetting and double emulsion[51]. Some disadvantages of pulsed jetting are that the lifetime of the vesicles is limited, there might be oil in the membrane, and not all biological material might be able to survive the high shear stress of the jetting process[46, 55]. The double emulsion technique is easier to use than jetting, but solvent might be found in the membrane as well, as everything is not removed during the evaporation process[55]. There is also a chance that the membrane might rupture during the solvent removal. One drawback of cDICE is that it involves oil, and the oil might get trapped in the membrane. The advantages and disadvantages of the five techniques are summarized in **Table 1** below.

Table 1: Summary of properties of GUV generation methods

Method	Oil free	Mono-disperse	Efficiency of GUV production	Control on lamellarity	Encapsulation efficiency	Advanced equipment	Time	Ref.
Gentle hydration	Yes	No	High	Low	Low	No	Hours	42
Electro-formation	Yes	No	High	Low	Low	No	Hours	42, 44
Pulsed jetting	No	Yes	High	High	High	Yes	Minutes	46, 55
Double emulsion	No	Yes	High	High	High	Yes	Hours	46
cDICE	No	Yes	High	High	High	No	Minutes	50

2.2 Poly(N-isopropylacrylamide) (PNIPAAm)

2.2.1 Structure and Physical Properties

Poly(N-isopropylacrylamide) (PNIPAAm) is a synthetic thermoresponsive polymer with a lower critical solution temperature (LCST) at 32 ℃ in pure water. It was first described in 1968[56], and since then, it has been extensively studied, especially for biomedical applications, due to its water-soluble properties and its LCST being close to body temperature (37.5 ℃)[57]. PNIPAAm exhibits an inverse solubility behavior: it becomes phase separated when heated above the LCST and transitions from sol to hydrogel phase[58]. A ‘sol’ is a colloidal solution made of particles or polymers dispersed in a continuous liquid medium, while a ‘gel’ is a rigid network of particles or polymeric chains[59]. There are two types of hydrogels: physical and chemical. Physical hydrogels are held together by molecular entanglements between the polymer chains, and/or ionic bonds, hydrogen bonds or hydrophobic forces. Their structure is disordered, and their assembly is reversible. Chemical hydrogels are covalently cross-linked, permanent networks of polymer chains, and are chemically stable structures[60].

The gelation of PNIPAAm arises from the structure of its monomer constituents, which are characterized by the polar amide (-CONH-) group and nonpolar propyl ($-CH(CH_3)_2$) groups (**Figure 14a**)[57, 61]. In aqueous solutions, when the temperature is below the LCST, the hydrophilic amide groups form hydrogen bonds with the surrounding water molecules and become hydrated. The polymer is therefore fully water-soluble in this state[61]. When a solution of linear PNIPAAm homopolymer chains (sol phase) is heated above the LCST, the hydrophobic interactions between the isopropyl groups increase, and hydrogen bonds form between the amide groups leading to exclusion of water molecules [40, 62]. This drives the conformational change of the individual polymer chains from expanded coils to collapsed globules (**Figure 14b**)[57, 58]. If the concentration of PNIPAAm in the solution is over the critical gel concentration (CGC), the conformational change induces the aggregation of the polymer chains into clusters and subsequent microphase separation[40]. This results in the formation of a physical hydrogel, with a polymer network held together by H-bonding and hydrophobic forces[60]. The phase transition is a reversible process and makes the PNIPAAm sol change from transparent to turbid in the hydrogel phase[57]. For the cross-linked chemical PNIPAAm hydrogel, heating above the critical temperature leads to a reversible volume phase transition (**Figure 14c**)[40]. In the case of the cross-linked PNIPAAm, a major difference is the permanent network formation which does not reverse during the transition between expanded and collapsed states.

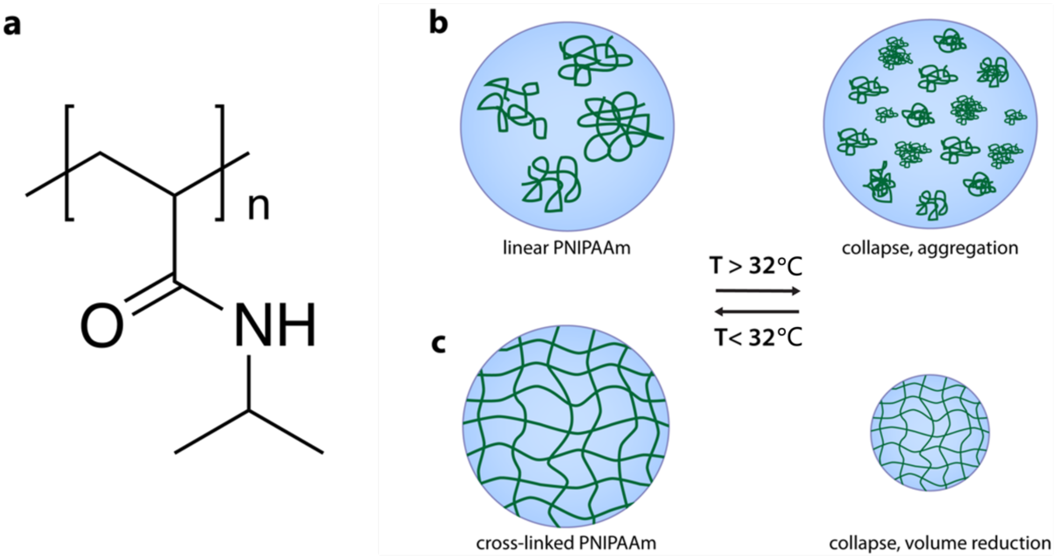

Figure 14: (a) Structure of PNIPAAm. (b) Formation of a physical hydrogel and (c) chemical hydrogel upon crossing the LCST of PNIPAAm. Adapted with permission[63]. Copyright 2018, American Chemical Society.

2.2.2 PNIPAAm Internalized in GUVs

Giant unilamellar vesicles filled with aqueous PNIPAAm solution in their interior can be used as models to investigate macromolecular crowding, intracellular phase separation and sub-compartmentalization. In the context of artificial cells, PNIPAAm is frequently used as a component of the membrane of polymersomes[64] and proteinosomes[65]. However, the encapsulation of PNIPAAm inside artificial cells, has received less attention[39, 40, 66-69]. In most of these studies, PNIPAAm was cross-linked into microgels, which were brought into close contact with free lipid molecules or liposomes by methods including freeze-thaw cycling[66], solvent-exchange[67] and centrifuging of microgels onto a lipid film[68]. Encapsulation of PNIPAAm in sol phase is rather rare, and has previously been performed by electroformation[40] and microinjection[39].

One possible application of PNIPAAm would be enabling macromolecular crowding in artificial cells. PNIPAAm can be used to achieve a macromolecularly crowded cytoplasm-like interior inside GUVs. Macromolecules occupy 20-30 % of the cell’s interior, making the cytoplasm a highly viscous, gel-like medium rather than a liquid. For many years, the crowding of macromolecules had not been considered when studying the internal dynamics of cells and crowding as a phenomenon has rarely been discussed in textbooks of biochemistry and molecular biology[70]. Studies show that the molecular crowding in the interior of the cell has a significant effect on the kinetics and thermodynamics of the macromolecules resulting from volume exclusion and hindered diffusion[71].

PNIPAAm can also provide intracellular phase separation and sub-compartmentalization. When PNIPAAm sol encapsulated in a GUV is heated above the LCST, the internal volume of the vesicle becomes phase separated and sub-compartmentalized. The polymer chains has been shown to aggregate into multiple microaggregations (**Figure 15b'**) or contract into a single aggregate (**Figure 15d'**)[39]. This could be a way of generating dynamic, higher-order artificial cells with molecularly crowded, membraneless sub-compartments. Membraneless sub-compartments have the ability to spatially separate molecules and can be used to model membraneless organelles (MLO), which are present in biological cells in the form of nucleoli, Cajal and promyelocytic leukemia bodies[72, 73]. Another system that has been more widely explored as a model for multicompartment artificial cells with membraneless subcompartments, are lipid membrane-enclosed coacervate microdroplets[74-76]. Coacervates are formed through liquid-liquid phase separation of a homogeneous solution of macromolecules[77]. In the case of complex coacervates, electrostatic interactions between polyelectrolytes of opposite charges drive the formation of a physical hydrogel known as an "isotropic" hydrogel[60].

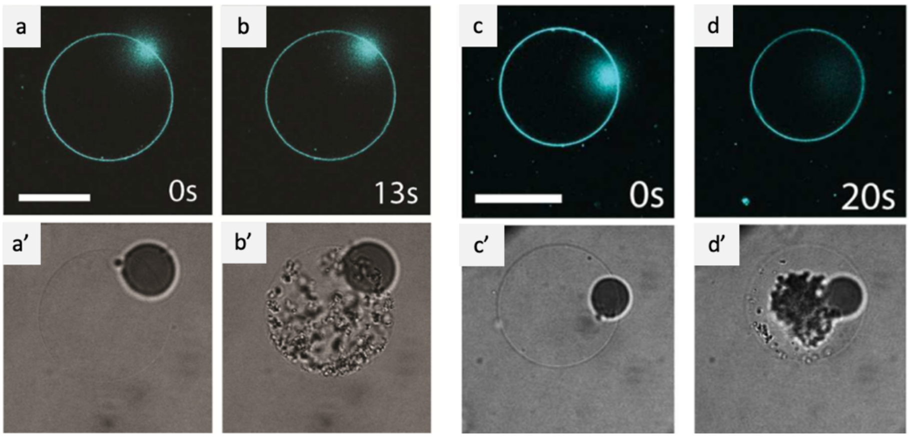

Figure 15: PNIPAAm sol encapsulated in GUVs. (a-d) are fluorescence micrographs (a'-d') are their corresponding bright field images. (b') Multiple microaggregations. (d') Single aggregate. Scale bars are 30 µm. Adapted with permission[39]. Copyright 2011, American Chemical Society.

2.3 Preparation of Aqueous Solutions

Deionized water (DI) was purified using the Millipore Milli-Q® water Gradient A10 purification system from Merk and was used for the preparation of all aqueous solutions. Unless specified otherwise, all equipment, such as the glassware and tubing for the microfluidic system, was cleaned by rinsing with isopropanol followed by DI-water and dried using nitrogen gas. Glucose, sucrose, Optiprep™ iodixanol solution and PNIPAAm was purchased from Sigma-Aldrich.

2.3.1 100 mM Glucose solution

The outer aqueous solution (OAS) was a solution of glucose in DI-water for all experiments. The osmolarity was matched to the inner aqueous solution and was 100 mOsm in all experiments. 3,6032 g glucose (powder) was weighed and added to 200 mL DI-water and then dissolved by using a magnetic stirrer for approximately 5 minutes. The solution was then filtered using a vacuum filter with pore size of 0.22 µm. The solution was divided into 50 mL tubes that were stored in the fridge (4℃).

2.3.2 100 mM Sucrose solution

For most of the experiments, sucrose (M=342.30 g/mol) was used in the inner aqueous solution (IAS) to increase the density of the IAS compared to the OAS. A density contrast facilitates the interface crossing of the droplet from LOS to OAS. The sucrose solution was made the same way as the glucose solution: 6,846 g sucrose was added to 200 mL DI-water.

2.3.3 100 mM Iodixanol solution

The second IAS was a high-density aqueous solution of 100 mM iodixanol, made using the Optiprep™ density gradient medium. In recent studies, iodixanol was used in the IAS medium to facilitate the formation of droplets[51, 78]. Iodixanol has a higher molar mass (M=1550.191 g/mol) than sucrose and therefore creates a higher density contrast. 23 mL of the stock Optiprep™ iodixanol solution (60% w/v) was diluted in 177 mL DI-water to achieve a concentration of 100 mM (11.5% v/v). The solution was mixed with a magnetic stirrer for approximately 5 minutes and then filtered using syringe filters with pore size 0.2 µm. Iodixanol was used to form vesicles for the control experiments.

2.3.4 1 mM PNIPAAm solution

We employed PNIPAAm in powder form, with a number average molecular weight (M_n) of 30,000 g/mol. The concentration was set to 30 mg/mL, which corresponds to 1 mM, as employed in the study by Wegrzyn et al.[39]. A 5 mL solution of 1 mM PNIPAAm and 99 mM sucrose was made by adding 0,150 g PNIPAAm to 4950 µL 100 mM sucrose solution and 50 µL DI water. Both the sucrose solution and DI-water was cold and had been stored in the fridge to facilitate the dissolution of PNIPAAm. The polymer was dissolved in the cold DI-water by vortexing for around 20 sec. The tube was stored in the fridge and vortexed every hour. The PNIPAAm had completely dissolved after 5 hours.

2.4 Preparation of Lipid-in-Oil Solution

Various protocols for the preparation of lipid-in-oil solution (LOS) were employed and modified. The original protocol by Abkarian et al. from 2011[50] was used for the majority of the experiments. A protocol by Loiseau et al. from 2016[11], based on the solvent shifting effect mentioned in section 2.1.5, was also employed. Vesicle formation was not consistent throughout different samples with these methods; some samples only contained a few or no vesicles. A recently published paper on optimization of the cDICE method by Van de Cauter et al.[51] was the most successful and used for the final experiments involving thermal manipulation of vesicles. In this protocol, the final lipid concentration is lower than that of the other two, and it involves the formation of a dry lipid film that is rehydrated with an oil-mixture based on the solvent shifting effect. The authors also recommend keeping the cylindrical chamber tilted for 15 min after removing the excess oil. This improved the efficiency of GUV collection and resulted in cleaner samples.

In this section, the protocol developed by Abkarian et al. will be referred to as Protocol 1, the one by Loiseau et al. as Protocol 2, and the one by Van de Cauter et al. as Protocol 3, although these protocols themselves were slightly modified, e.g. instead of dehydration of lipid films by gentle nitrogen drying, rotary evaporation was used.

L-α-phosphatydilcholine (Egg PC), 1-palmitoyl-2-oleoyl-*sn*-glycero-3-phosphocholine (16:0-18:1 PC; POPC), Liss Rhod PE, chloroform, decane, mineral oil and silicone oil were purchased from Sigma-Aldrich. Methanol was purchased from VWR.

2.4.1 Protocol adapted from Abkarian et al. 2011

Table 2: Values used for LOS with Egg-PC made following the protocol by Abkarian et al[50].

Component		Percentage %	Mass (µg)	Stock (mg/mL)	Volume (µL)	Concentration (mg/mL)
Lipid	Egg-PC	99	4574	20	229	
Dye	Liss Rhod PE	1	46	1	46	
Chloroform					187	
Total		100	4620		462	10 mg/mL
EVAPORATION						

Mineral oil					12000	
Total			**4620**		**12000**	**0.385 mg/mL**

Table 3: Values used for LOS with POPC following the protocol by Abkarian et al[50].

Component		**Percentage %**	**Mass (µg)**	**Stock (mg/mL)**	**Volume (µL)**	**Concentration (mg/mL)**
Lipid	POPC	99	4514	25	181	
Dye	Liss Rhod PE	1	46	1	46	
Chloroform					229	
Total		100	4560		456	10 mg/mL
EVAPORATION						
Mineral oil					12000	
Total			**4560**		**12000**	**0.380 mg/mL**

L-α-phosphatydilcholine (Egg PC) or 1-palmitoyl-2-oleoyl-*sn*-glycero-3-phosphocholine (16:0-18:1 PC; POPC) was used as the main lipid species to form GUVs with this protocol. L-α-phosphatydilcholine (Egg PC) in powder form was dissolved in a chloroform:methanol (9:1) mixture to make a stock solution of 20 mg/mL. 1125 μL chloroform and 125 μL methanol was added to 25 mg Egg PC powder. POPC lipids were bought dissolved in chloroform with the stock concentration of 25 mg/mL. The Egg PC or POPC lipids, Liss Rhod PE and chloroform were mixed in in a pear-shaped glass flask in the calculated quantities shown in **Table 2** or **3** above. The components were added to the flask using clean Hamilton glass syringes of 250 uL and 50 uL, in the order of chloroform – lipid – dye. The glass flask was connected to a rotavapor in water bath at 23 ℃ (**Figure 16**).

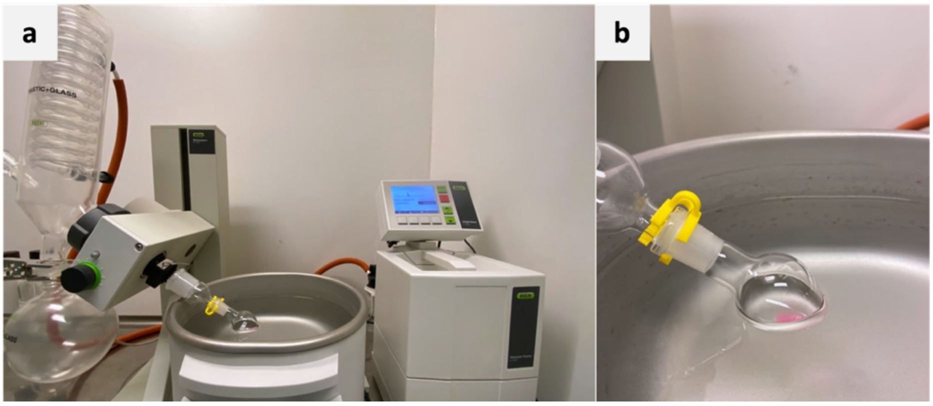

Figure 16: (a) Rotavapor instrument. (b) Formation of lipid film by rotary evaporation. The glass flask is submerged in a water bath at 23 ℃ and rotates at 24 rpm

The immersion angle was set to 35° and the rotation speed to 24 rpm. The pressure was then decreased from 100 kPa to 20 kPa by increments of 20 kPa, waiting 2 min between each step.

After reaching 20 kPa, the solution was dehydrated for 1 hour. The resulting lipid film in the bottom of the flask was rehydrated with mineral oil to get a final lipid concentration of 0.5 mM. After tightly closing the flask with a glass stopper and securing the seal with Parafilm, the LOS was sonicated for 1 hour while the bath temperature was kept under 40 °C, to form a homogeneous lipid dispersion.

2.4.2 Protocol adapted from Loiseau et al. 2016

Table 4: Values for LOS made from POPC following the protocol by Loiseau et al[11].

Component		Percentage %	Mass (µg)	Stock (mg/mL)	Volume (µL)	Concentration (mg/mL)
Lipid	POPC	99	3837	25	154	
Dye	Liss Rhod PE	1	39	1	39	
Decane					**600**	
Silicone oil					**7520**	
Mineral oil					1880	
Total		**100**	**3876**		**10193**	**0.380 mg/mL**

POPC was used as the main lipid species in this protocol. Alike Protocol 1, the lipids were added to a clean glass flask in the calculated quantities (**Table 4**). However, instead of forming a lipid film through rotary evaporation, the lipids in chloroform were directly mixed with decane and a silicone oil:mineral oil mixture (4:1). To disperse the lipids as aggregates, they must first be dissolved in a good solvent, then mixed with a second solvent that is miscible with the first one but is a poor solvent for lipids[54]. Here, chloroform and decane are the good solvents, while silicone oil and mineral oil are poor solvents (**Figure 17a**). The lipid aggregates will form when the oil mixture is added to the lipid solution and sonicated (**Figure 17b**).

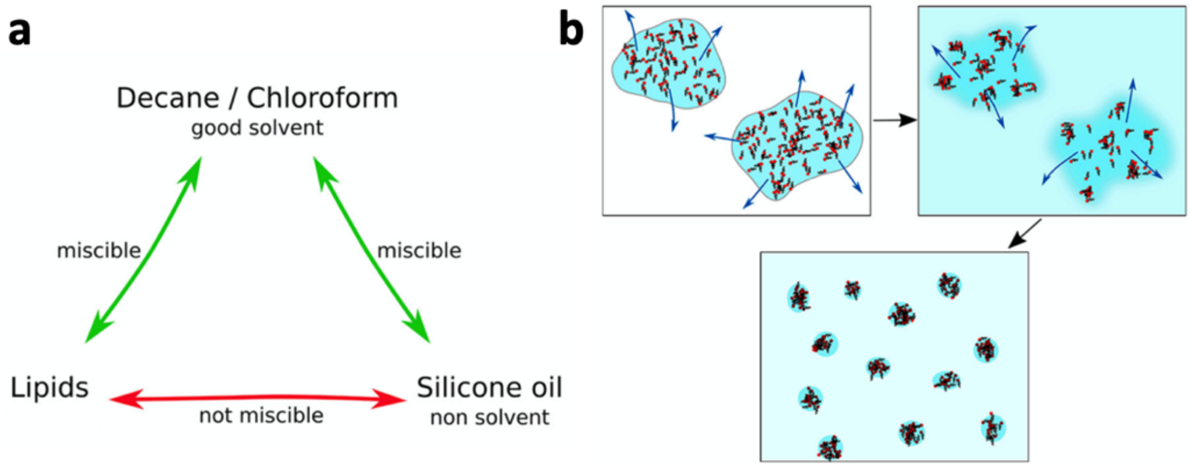

Figure 17: Key principle behind dispersion of lipids as aggregates in oil solution. Adapted with permission[54]. Copyright 2016, DP Sciences, SIF, Springer-Verlag Berlin Heidelberg.

Two pear shaped glass flasks were cleaned: one for the lipids and the other for the oil mixture. The silicone oil and mineral oil were added to the flask using serological pipettes. The oil mixture was vortexed for 1 min to acquire a homogeneous mixture. The oil mixture was then added to the lipid-chloroform-decane solution by using a serological pipette while gently vortexing. The flask was sealed and vortexed for an additional 2.5 min. The LOS was then sonicated for 15 min and used the same day. The sonication time is significantly reduced in protocols based on solvent shifting compared to Protocol 1 (15 min vs. 1 h).

2.4.3 Protocol adapted from Van de Cauter et al. 2021

Table 5: Values for LOS made from POPC following the protocol by Van de Cauter et al[51].

Component		**Percentage %**	**Mass (µg)**	**Stock (mg/mL)**	**Volume (µL)**	**Concentration (mg/mL)**
Lipid	POPC	99	2080	25	84	
Dye	Liss Rhod PE	1	22	1	22	
Chloroform					104	
Total		**100**	2102		210	**10 mg/mL**
EVAPORATION						
Decane					**830**	
Silicone oil					**10400**	
Mineral oil					2600	
Total		**100**	**2102**		**13830**	**0.152 mg/mL**

The third protocol has elements of both Protocol 1 and Protocol 2. The lipids were dehydrated by rotary evaporation to form a lipid film and rehydrated with decane, followed by a mineral oil-silicone oil mixture (1:4). POPC, Liss Rhod PE and chloroform were mixed in the calculated quantities shown in **Table 5** and dehydrated for 1 hour (same parameters as Protocol 1). After rehydrating with decane, the mineral oil-silicone oil mixture was added to the flask via a serological pipette while gently vortexing. The final lipid concentration was 0.2 mM (0.152 mg/mL), which is lower than the concentrations used in the other two protocols. The flask was closed, and the solution was vortexed for another 2,5 min. In the last step, the flask was sealed with Parafilm, and the solution was sonicated for 15 min while the bath temperature was kept below 40 °C. The bath temperature was kept at 20 °C – 30 °C by exchanging half of the water in the sonicator with DI-water that had been stored in the fridge (4 °C) before sonication. The different steps for the preparation of the LOS are shown in **Figure 18**.

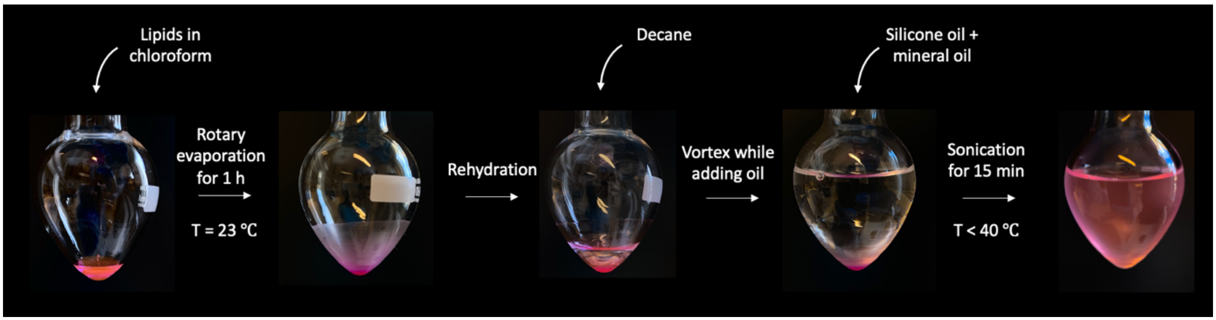

Figure 18: Steps in the preparation of lipid-in-oil dispersion by following the protocol in Van de Cauter et al.[51].

2.5 Design and Set-up of Spinning Device

The spinning device used for the cylindrical chambers in cDICE was a custom-made set-up (I-Lab, University of Oslo). The device consists of a brushless DC motor with driver (BLM230HP-AS/ BMUD30-C2) obtained from Oriental Motor USA Corp, on top of which there is a holder for the rotating chamber. The motor is enclosed by a metal box with the speed controller mounted on the side of the box (**Figure 19**). The holder has a screw lock mechanism that ensures that the chamber stays in place while rotating at high speed. The motor has a variable speed range from 50 to 4000 rpm.

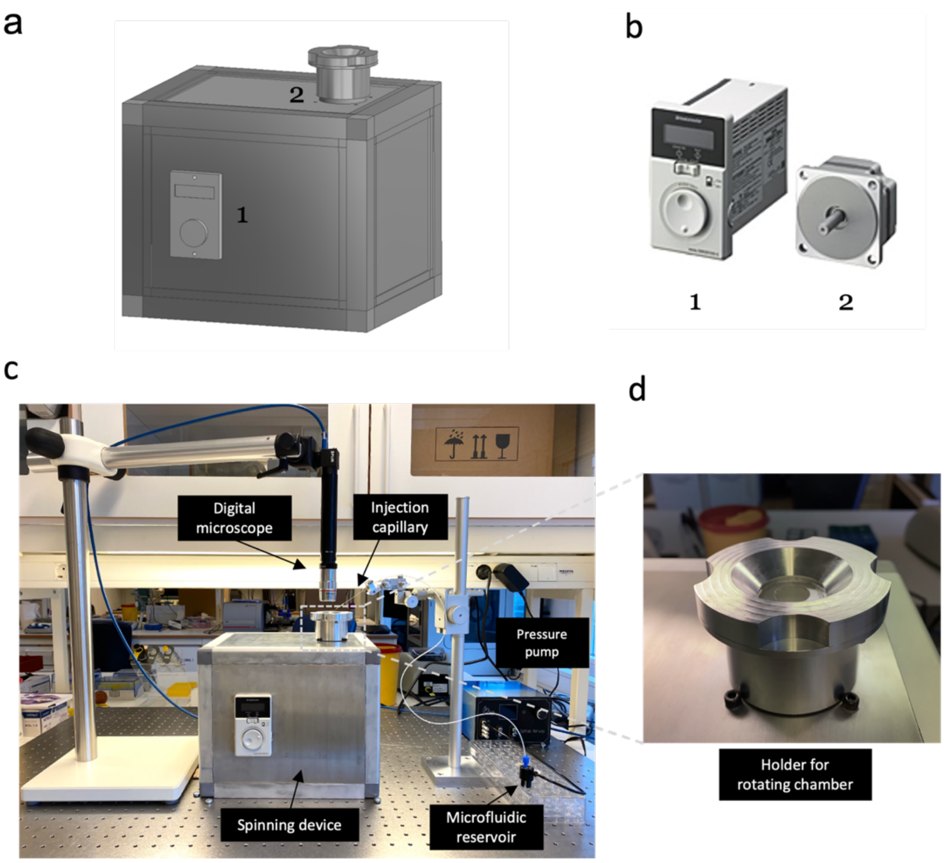

Figure 19: Experimental set-up. (a) Illustration of spinning device with (b) the brushless motor (1) and driver (2)[79]. (c) Experimental set-up for cDICE. (d) Holder for rotating chamber with screw lock.

2.6 Design and Assembly of Cylindrical Chambers

The cylindrical chambers were made by using the lids of Petri dishes (ØxH: 35 x10 mm) made of polystyrene (**Figure 20a**) and attaching these to round glass microscope slides. The inner diameter of the lid is 38 mm, while the outer diameter is 40 mm. The glass slides were purchased from Electron Microscopy Sciences and are 1 mm thick and have a diameter of 40 mm. Holes of 15 mm diameter (**Figure 20b**) were drilled in the center of the lids (**Figure 20c**).

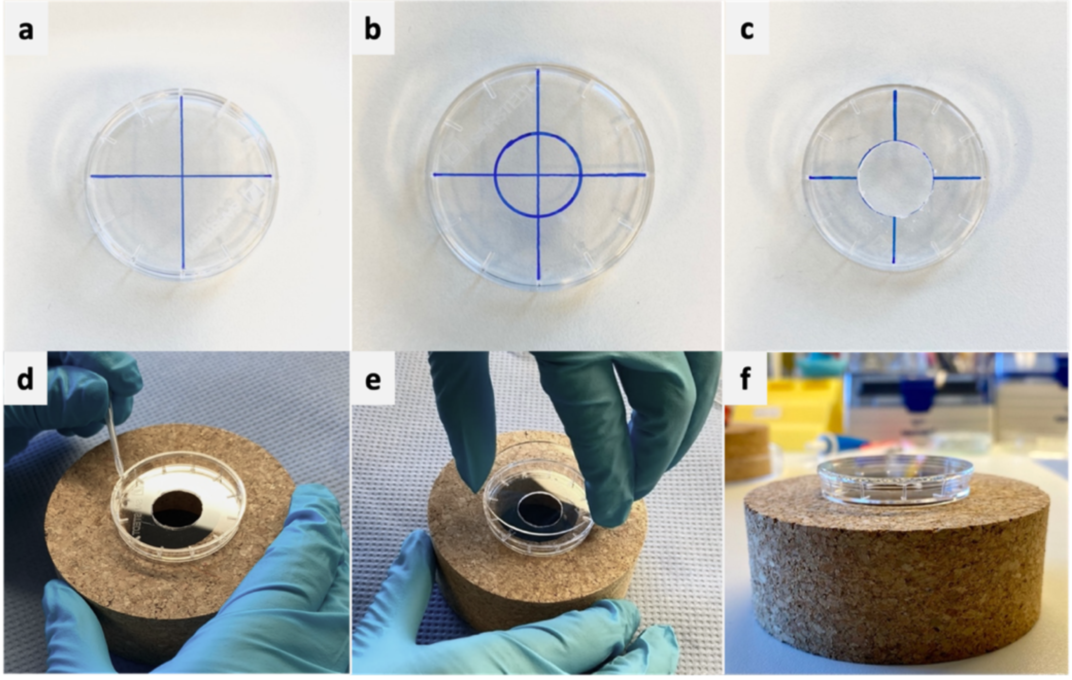

Figure 20: Assembly of cylindrical chambers. (a) The center of the Petri dish lid is marked. (b) A circle with d= 15 mm is drawn at the center of the Petri dish lid. (c) A hole is drilled through the circle in (b). (d) Epoxy glue is applied to the rim of the Petri dish lid. (e) The glass microscope slide is attached to the lid (f) The glue is left to dry overnight.

Various opening hole sizes were tested; 5, 10 and 15 mm, but 15 mm was the optimal size for easy insertion of the injection capillary. After cleaning the lid and glass slide, a two-component epoxy glue was applied to the rim of the lid (**Figure 20d**), which was attached to the glass slide (**Figure 20e**) and left to dry overnight (**Figure 20f**).

2.7 Fabrication of Injection Capillaries

Three different materials were tried for use as injection capillaries: silanized and unsilanized fused silica capillaries, silanized and unsilanized glass micropipettes and PEEK capillaries.

2.7.1 Fused Silica Capillaries

The fused silica capillary tubing, produced by Postnova, was purchased from Norlab, Finland. We tried various inner diameters: 5, 10, 25 and 100 µm. The capillaries were cut 2-3 cm long, using the fused silica tubing cutter by Shortix™, purchased from Sigma-Aldrich (**Figure 21a**).

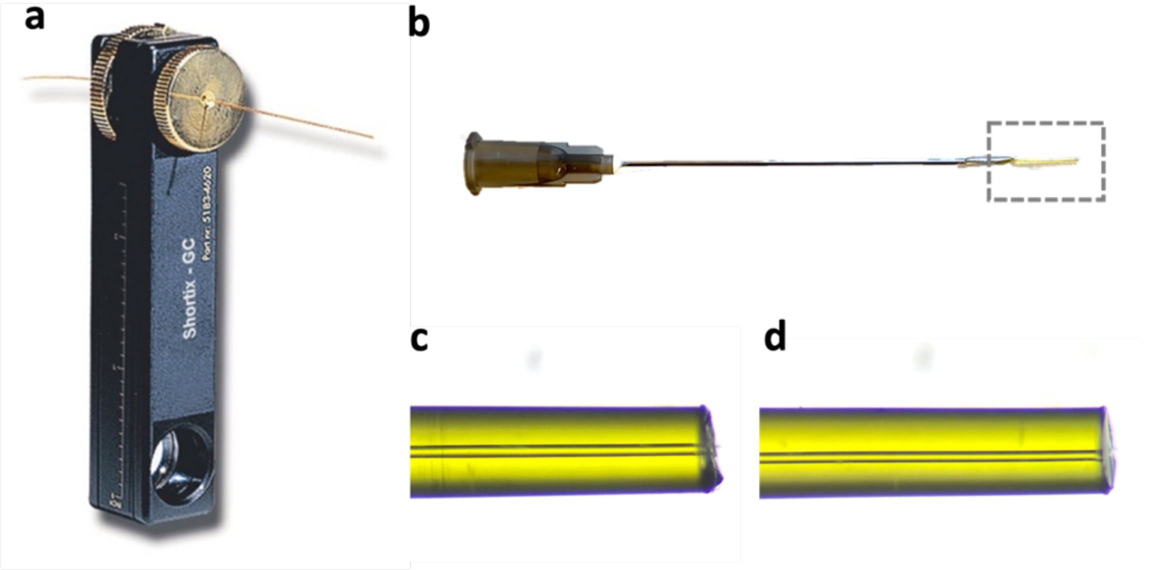

Figure 21: Preparation of fused silica capillaries. (a) Tubing cutter by Shortix™ [80]. (b) Assembled injection capillary consisting of a syringe needle (22G x 2") with a fused silica capillary (ID: 25 µm, OD: 370 µm). (c) Tip of a capillary that is not cut properly. (d) Capillary tip with a clean cut.

The cutter has a diamond blade that enables the clean, straight cut of capillaries with ID over 100 µm and OD up to 800 µm. The device was used for capillaries with inner diameter of 25 µm as well but did not result in a clean cut each time (**Figure 21c**). Approximately 20 cm of the capillary was first gently wiped using acetone on lint-free wipes by Kimtech. Then it was inserted into the cutter while pressing the blade down to allow the passage through the device and out on the other end. After 1.5-2 cm of the capillary was threaded through, the blade was released, and the capillary tightened by turning the wheel on the backside. The front wheel was then turned around until the capillary was cut off.

The cut capillary pieces were observed in a stereo microscope, and the ones with the cleanest cut ends were salinized. In the early stages of this project, unsilanized fused silica capillaries were used as injection capillaries. After a digital microscope was installed, we could observe the droplet formation in real-time. This revealed issues with droplet formation for the unsilanized capillaries. The aqueous solution was wetting the outer wall of the tip and climbing upwards (**Figure 22a**).

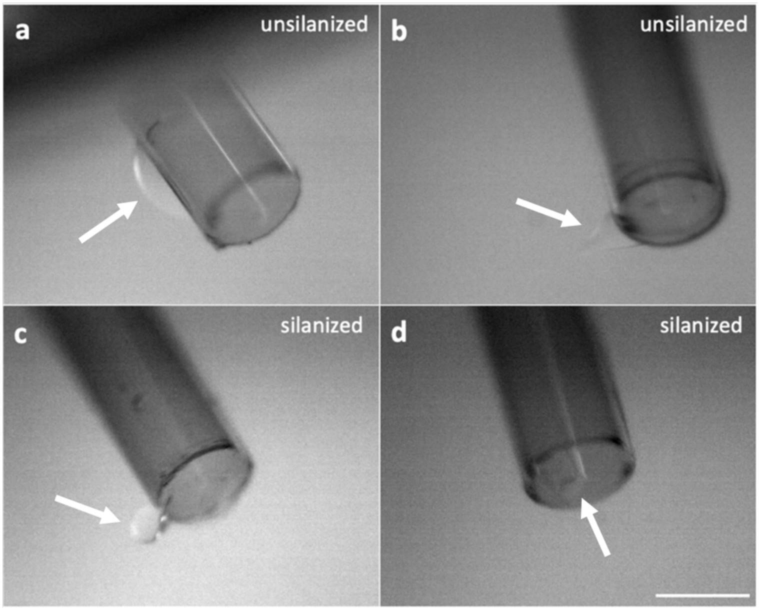

Figure 22: Fused silica capillary tips. (a) The outer wall of the unsilanized capillary is wetted. Droplets not detaching from an (b) unsilanized- and a (c) silanized capillary with uneven tip-surfaces. (d) Proper droplet formation from a silanized capillary with even tip-surface. The aqueous solution is indicated with white arrows.

The capillaries were therefore silanized to increase the hydrophobicity of the glass. This led to enhanced droplet formation: the droplets were easily detaching from the tip. Another important factor is the shape of the capillary tip. When the fused silica capillary tips had an uneven surface, we observed that the aqueous solution would get attached to this part instead of detaching, both for the unsilanized (**Figure 22b**) and silanized capillaries (**Figure 22c**).

A petri dish containing fused silica capillaries was place inside a desiccator in a fume hood, along with 1 mL of dichlorodimethylsilane in a glass vial and maintained under vacuum for 2 hours. The capillary pieces were then inserted into syringe needles (22G x 2") with the end that had been exposed during salinization facing away from the metal part of the needle. The parts were glued together with the same two-component glue used for the rotational chambers. The capillary-needles were left to dry overnight.

2.7.2 Glass Micropipettes

Glass micropipettes were used as injection capillaries, as an alternative due to the issues with droplet formation with unsilanized fused silica capillaries. Micropipettes made of borosilicate glass with filament with O.D 1.0 mm and I.D. 0.78 mm from Sutter Instrument (BF100-78-10) were utilized. The glass micropipettes were pulled using the P-2000 Micropipette Puller from Sutter Instrument. A micropipette puller works by heating the micropipette with a laser at the center point of the pipette, and pulling it apart to make two shorter pipettes, each with one narrow end. The program of the micropipette puller was set as to the parameters written in **Table 6**. The program should loop once, and the heat-on-time should be 4,8 ± 0,15 sec.

Table 6: Program for pulling borosilicate glass micropipettes with P-2000 Micropipette puller from Sutter Instrument

HEAT	FIL	VEL	DEL	PULL
300	5	150	128	50

The maximum tip opening that can be reached with a laser cutter is 20 µm. For cDICE an optimal tip diameter of 25-100 µm was suggested. To create a larger pipette tip with an opening size of 20-200 µm after micropipette pulling, the micropipettes must be scored using a ceramic tile, optic scribe, or the glass-to-glass technique. I used the glass-on-glass approach as depicted in **Figure 23**.

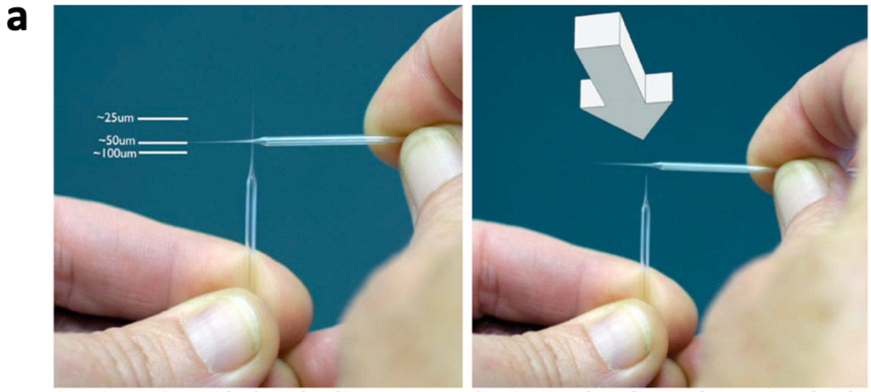

Step .1 *Score only, do not break!*

Step 2. Move above the score location & push with a smooth, continuous motion to break the glass.

b ¼th back from the tip = 25µm ½ back from the tip = 50µm

2/3rd back from the tip = 75µm 3/4th back from the tip = 100-200µm

Figure 23: (a) Glass-on-glass technique for scoring glass micropipettes. (b) Approximate placements of the scoring pipette for obtaining tip-diameters between 25 and 200 µm .Image from Pipette Cookbook 2018, Sutter Instruments [81].

The glass-on-glass technique involves two steps. First, one pipette is held vertically, and the second scoring pipette is held horizontally. The first pipette is scored using the thicker region near the shoulder of the taper of the second pipette, as shown in **Figure 23a**. The placement of the second pipette determines the size of the scored pipette tip, and the general rule of thumb is shown in **Figure 23b**. The glass is scored in one short horizontal movement (1 mm). In the second step, the scoring pipette is placed above the location of the score and is pushed back in a continuous motion to break off the glass[81].

The unbroken capillaries were silanized (same protocol as for fused silica) and then glued to syringe needles (14 G x 3") (**Figure 24**).

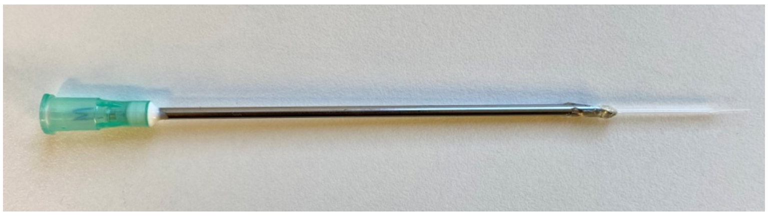

Figure 24: Glass micropipette-based injection capillary

The glass-on-glass method proved to be quite difficult, as many of the pipette tips were broken. Another downside of the technique is that the scoring of glass provides very low control over the opening diameter.

2.7.3 Polymeric (PEEK) Capillaries

Polyether ether ketone (PEEK) was another material that was used for the fabrication of injection capillaries (**Figure 25a**). PEEK is a hydrophobic polymer, so silanization could be bypassed with this material. The PEEK capillaries are also easier to cut than the fused silica capillaries and are manufactured with great control over diameter size. PEEK capillaries of 50 and 100 µm diameter, were purchased from Teknolab. The capillaries were cut using a polymeric tubing cutter by inserting the tubing into a hole with appropriate size (holes in **Figure 25b**) and pushing down the blade.

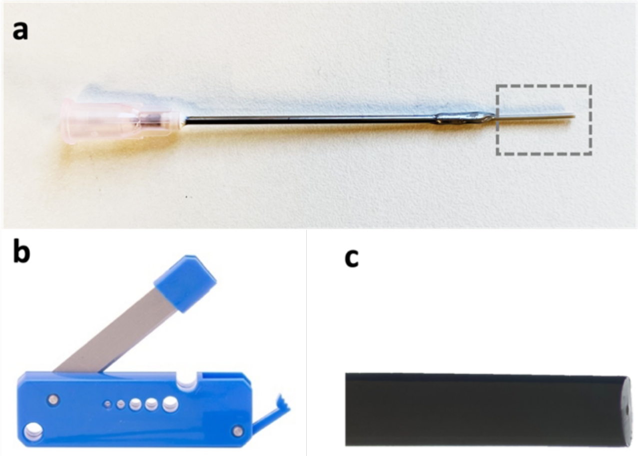

Figure 25: (a) PEEK injection capillary. (b) Polymeric tubing cutter. Copyright 2022, BGB Analytik AG. (c) Tip of a PEEK capillary (ID: 50 µm).

The PEEK capillaries were attached to syringe needles (18G x 2”) the same way as the other materials. Although the easy cutting, control over inner diameter and hydrophobic nature of PEEK makes it advantageous to fused silica and glass capillaries, it was difficult to observe droplet formation. It might be due to the opacity of the material or its highly hydrophobic nature. The droplet formation through PEEK capillaries should be further studied but due to the time limits, the experiments were continued with fused silica capillaries.

2.8 Design of Holder for Injection Capillaries

A holder for the positioning of the injection capillary with high control was necessary for the experimental set-up. To make this, a stand for Dino-Lite digital microscopes with a positioning arm, was purchased from VWR (parts: RK-06A, RK-06-PL, RK-10-PX). The holder part meant for the USB microscope was replaced with a custom-made holder for the capillary designed by I-lab, UiO (**Figure 26a**).

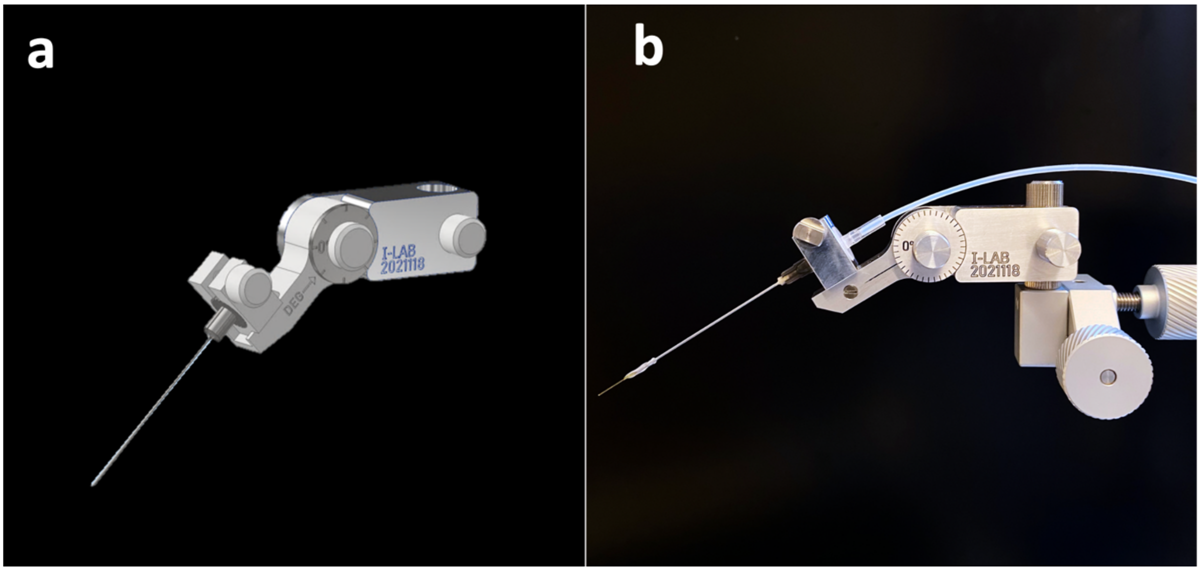

Figure 26: (a) Illustration of capillary holder. (b) Photograph of the capillary holder attached to the stand with a fused silica injection capillary.

The holder is mounted to the stand and can be set to various angles by increments of ten degrees. 30 degrees was the position that permitted the optimal insertion of the capillary into the cylindrical chamber. The foot of the stand was replaced with a heavier custom-made aluminum board that can be screwed onto a breadboard.

2.9 Workflow of the Pressure Pump

The microfluidic set-up for the cDICE system consists of a pneumatic pump (built in-house), a microfluidic reservoir for the IAS and an injection capillary (**Figure 27**). It has four outlet channels: two for positive pressure (0-450 mBar) and two for negative pressure (-300-0 mBar). The pressure is controlled manually using the knob in the pump or digitally by wireless connection to a smartphone or computer. The actual pressure could be monitored through the associated software.

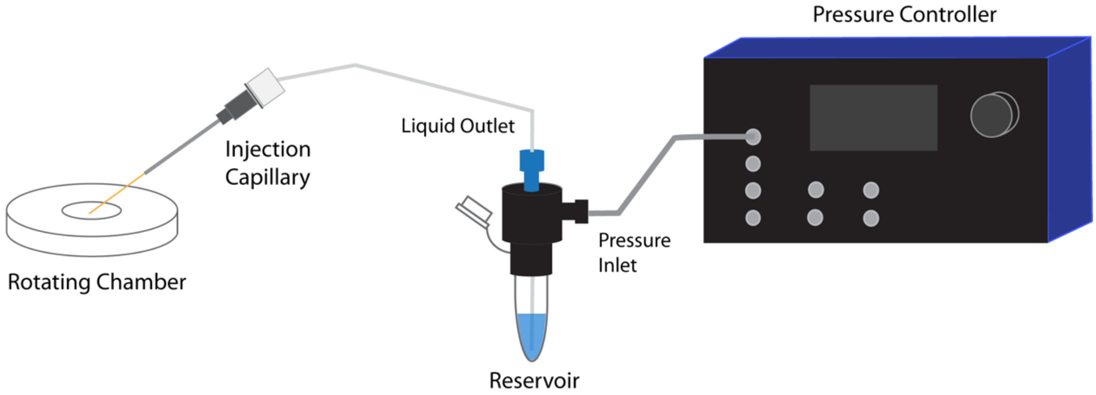

Figure 27: Illustration of the main components of the microfluidic set-up for cDICE.

The pressure inlet tubing for the microfluidic adapter is PTFE tubing with 3.2 mm OD and 2.4 mm ID. 30 cm of the tubing was connected to the pump via a plug-in reducer from SMC Automation. The other end of the tubing was connected to the microfluidic reservoir via the barbed end of a ¼-28 fitting which is connected to the microfluidic adapter from Elveflow® purchased from Darwin Microfluidics (**Figure 28**). On top of the adapter there is an opening for the liquid outlet PTFE tubing of 1.6 mm OD. The tubing is inserted, and the opening was made airtight by using a ¼-28 flangeless fitting with a ferrule. The liquid outlet tubing goes into a 1,5 mL Eppendorf® tube. When positive pressure is applied through the pressure inlet tubing, the reservoir (Eppendorf® tube) becomes pressurized, and the liquid (IAS) is forced into the liquid outlet tubing (**Figure 28**). All of the tubing was purchased from Darwin Microfluidics.

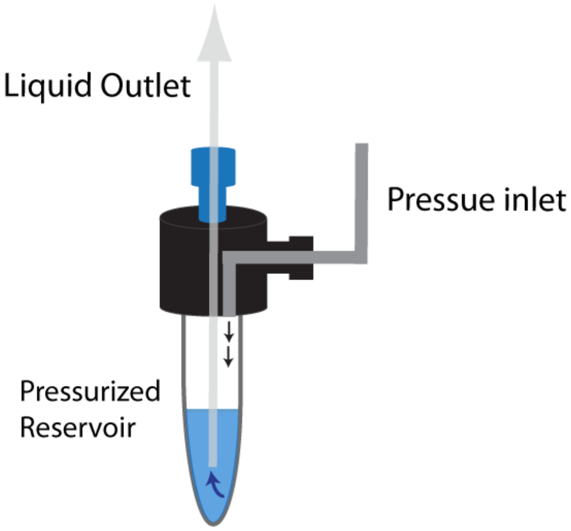

Figure 28: Pressurization of the microfluidic reservoir. When air is pushed into the reservoir, it gets pressurized, and the liquid is forced into the liquid outlet tubing. Image adapted from[82]. Copyright 2022, Elveflow.

2.10 Experimental Procedure for cDICE

The rotating chamber, liquid outlet tubing with luer lock adapter, microfluidic reservoir adapter and Eppendorf tube are cleaned with isopropanol and water and dried with nitrogen gas. The Eppendorf tube is filled with 200 µL of IAS and connected to the microfluidic reservoir adapter. The liquid outlet tubing is fitted to the adapter and the luer lock adapter is placed inside its holder. A capillary-needle is wiped with acetone and dried with N2 gas. The cleanness of the tip of the capillary is checked in a stereomicroscope, before connecting to the luer lock adaptor. The pressure is set to 100 mBar and the IAS in the reservoir, is led from the liquid outlet tubing and into the capillary. Next, the clean cylindrical chamber is secured inside the holder of the spinning device. The motor is then turned on and the speed of rotation is increased to a value between 1500 and 1900 rpm. Afterwards, the OAS followed by the LOS, are injected into the rotating chamber using automatic pipettes, in the quantities in **Table 7**.

Table 7 The solutions injected into the rotating chamber

Component	**Volume (μL)**
Outer aqueous solution (OAS)	700
Lipid-in-oil solution (LOS)	3500
Total	**4200**

Subsequently, the digital camera is turned on, and the capillary is inserted into the LOS (**Figure 29a**).

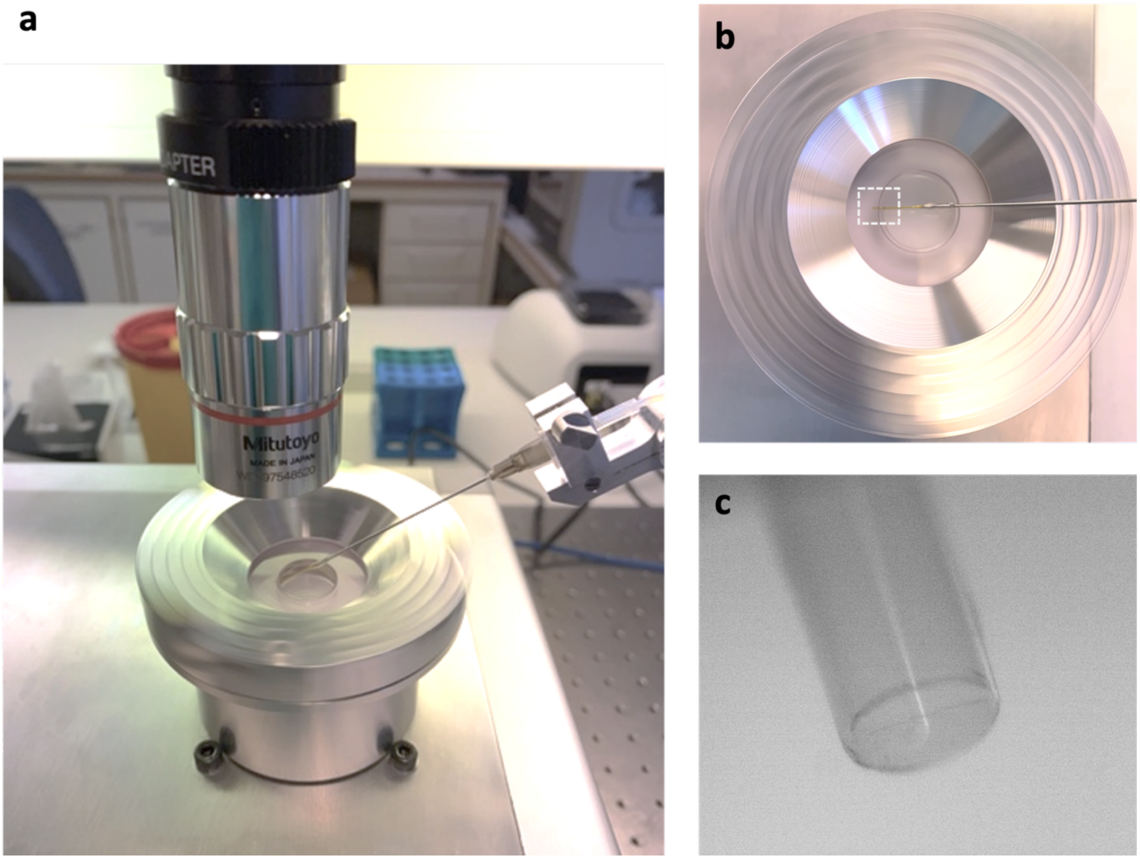

Figure 29: Injection capillary placed inside the rotating cylindrical chamber a) Side view. b) Top view. c) Image of a fused silica capillary tip captured by the digital microscope during injection.

The position of the capillary tip is adjusted with the knobs on the stand and moved into the camera frame. The recording is started, and the IAS is injected for 5 minutes. Irregularities of the surface of the capillary tip would often interfere with continuous droplet formation. In this case, the pressure was adjusted to promote the formation of evenly sized droplets.

After 5 minutes, the recording is stopped, and the capillary is ejected. The chamber is spun for another 5-10 minutes before slowly decreasing the speed of rotation and turning off the spinning. Four 1,5 mL Eppendorf tubes are prepared, and most of the oil is transferred into 3 of the tubes. The chamber is positioned vertically for 15-20 minutes to collect the bulk liquid on one side of the chamber as in lateral alignment the liquid spreads out to the bottom surface of the dish and the different phases becomes harder to observe and collect (**Figure 30a**).

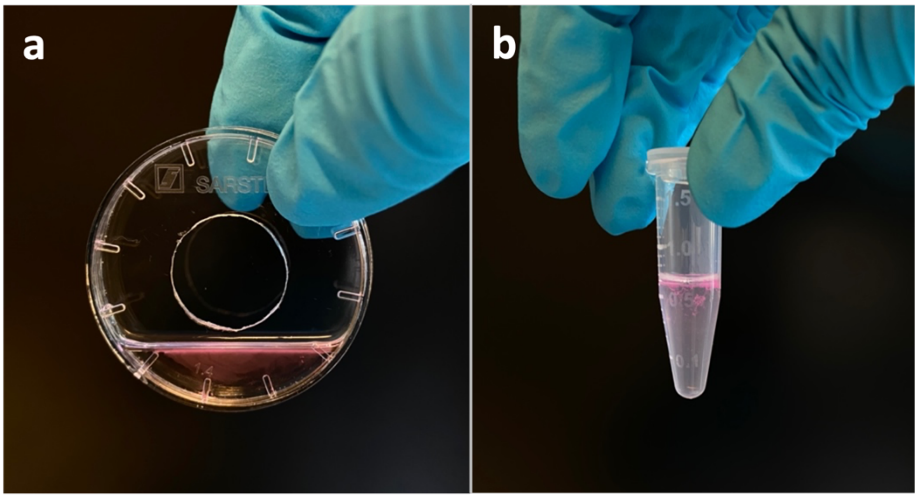

Figure 30: a) Vesicle dispersion after removing most of the oil. b) Vesicle dispersion transferred to a 1.5 mL tube. Some lipid debris (pink) is in the interface between the oil and aqueous solution.

This is a critical step that is necessary in order to collect most of the vesicles in the sample. Then the rest of the oil is removed, and the vesicle solution is transferred to the last tube (**Figure 30b**). The vesicles are either transferred to the microscope the same day or stored in the fridge (4℃) for observation the next day.

cDICE in principle is an easy method that is less demanding than other microfluidics-based set-ups. In practice however, as stated by Van de Cauter et al.[51], "the lack of understanding of the physical process of vesicle formation and of which parameters are essential to control tightly for the method to work robustly", makes the method less straight forward. One critical aspect of the cDICE method is the shape and hydrophobicity of the capillary tip. Using a hydrophobic capillary with a flat tip is necessary to make the droplets detach properly. Another important factor is the dispersion state of the LOS. The lipid film formation and rehydration with solvents that promote the formation of lipid aggregates, improves the formation of droplet coating and formation of vesicles. Lastly, a density gradient between the IAS and OAS and tilting the chamber after removing the excess oil, makes it easier to collect a high number of the produced vesicles.

2.11 Assembly and Fabrication of Imaging Chambers

The vesicles were deposited on rectangular glass cover slips (24 x 60 mm) (**Figure 31a**), or SU-8 coated circular glass cover slips (Ø: 47 mm) (**Figure 31b**) attached to a PDMS frame or circular hard plastic frames from WillCo Wells, respectively.

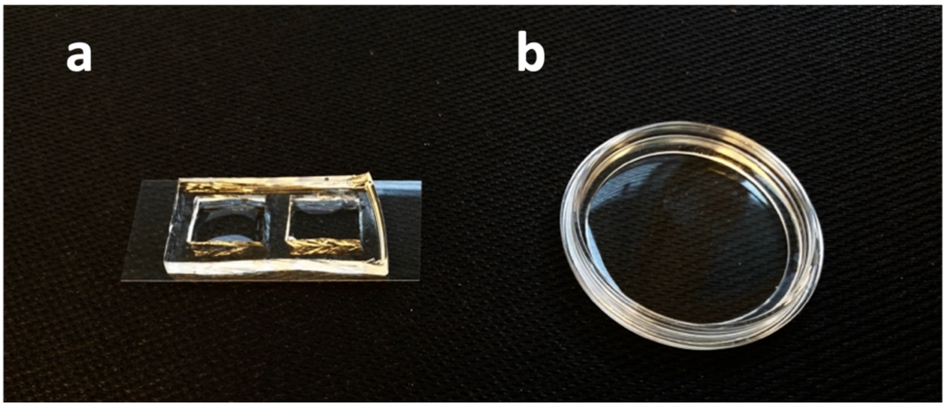

Figure 31: Imaging chambers. a) Rectangular glass slide attached to a PDMS frame with two compartments. b) Circular glass slide attached to a plastic frame by WillCo Wells.

2.11.1 SU-8 Deposition by Spin Coating

The 650M spin coater from Laurell Technologies was used to make the SU-8 coated surfaces. SU-8 is an epoxy-based photoresist that is hydrophobic and can be used to passivate glass surfaces to prevent the strong adhesion and rupture of the vesicles and allow prolonged observation. A round glass cover slip was cleaned and placed on top of the chuck of the spin coater. The surface was attached to the chuck by vacuum. 1 mL of SU-8 developer was pipetted on top of the surface and spin-coated at 2000 rpm for 1 minute. After the spin coating, the SU-8 coated surface was placed on top of a cork ring and soft baked in the oven at 95°C for 5 min. The surface was then taken out and exposed to UV-light for 5 min before post exposure baking for another 5 min at 95°C.

2.11.2 Preparation of PDMS Frames

To prepare a frame from PDMS in a large silanized glass Petri dish (Ø: 12 cm), 56 g elastomer was mixed with 5,6 mL of the curing agent. The components were mixed in a disposable plastic cup. The plastic cup was placed in a desiccator for 1 hour to eliminate air bubbles. The viscous solution is poured slowly over to a silanized glass Petri dish. Air bubbles should be avoided and if they appear, the Petri dish can be placed in the desiccator for 20 min or more until the bubbles are gone. The Petri dish is put into a preheated oven at 100 °C. After 45 minutes, the Petri dish is taken out and allowed to cool down at room temperature. The PDMS is removed from the silanized Petri dish by cutting it out with a scalpel. The PDMS is then cut into rectangles, with squares inside that are able to fit onto rectangular cover slips. The PDMS adheres to the glass and forms an air-tight seal.

2.12 Optical Fiber-Based IR-laser Set-Up

An optical fiber-based IR-laser set-up was employed to achieve localized heating of the GUVs. Infrared (IR) radiation is part of the electromagnetic spectrum with wavelengths longer than visible light and ranges from 780 nm to 1 mm. It is divided into three types: IR-A (780 nm-1400 nm), IR-B (1400 nm-3000 nm) and IR-C (3000 nm-1 mm)[83]. The energy of IR radiation is given off in the form of heat, i.e. thermal radiation[84]. We use a semiconductor diode IR-B laser that produces radiation with a wavelength of 1470 nm, by Seminex (HHF-1470-6-95) driven by an in-house built laser diode power supply (DC 12 V, 4.5 A). The semiconductor laser is connected to a multimode optical fiber cable (0.22 NA, core diameter: 50 µm). The tip of the cable has been stripped of the outer sheath cladding to expose the fiber core. The temperature and thermal range of the temperature gradient can be controlled by regulating the current and the distance between the fiber tip and the sample surface in the z direction. The relation between these parameters is shown in the plot in **Figure 32a**.

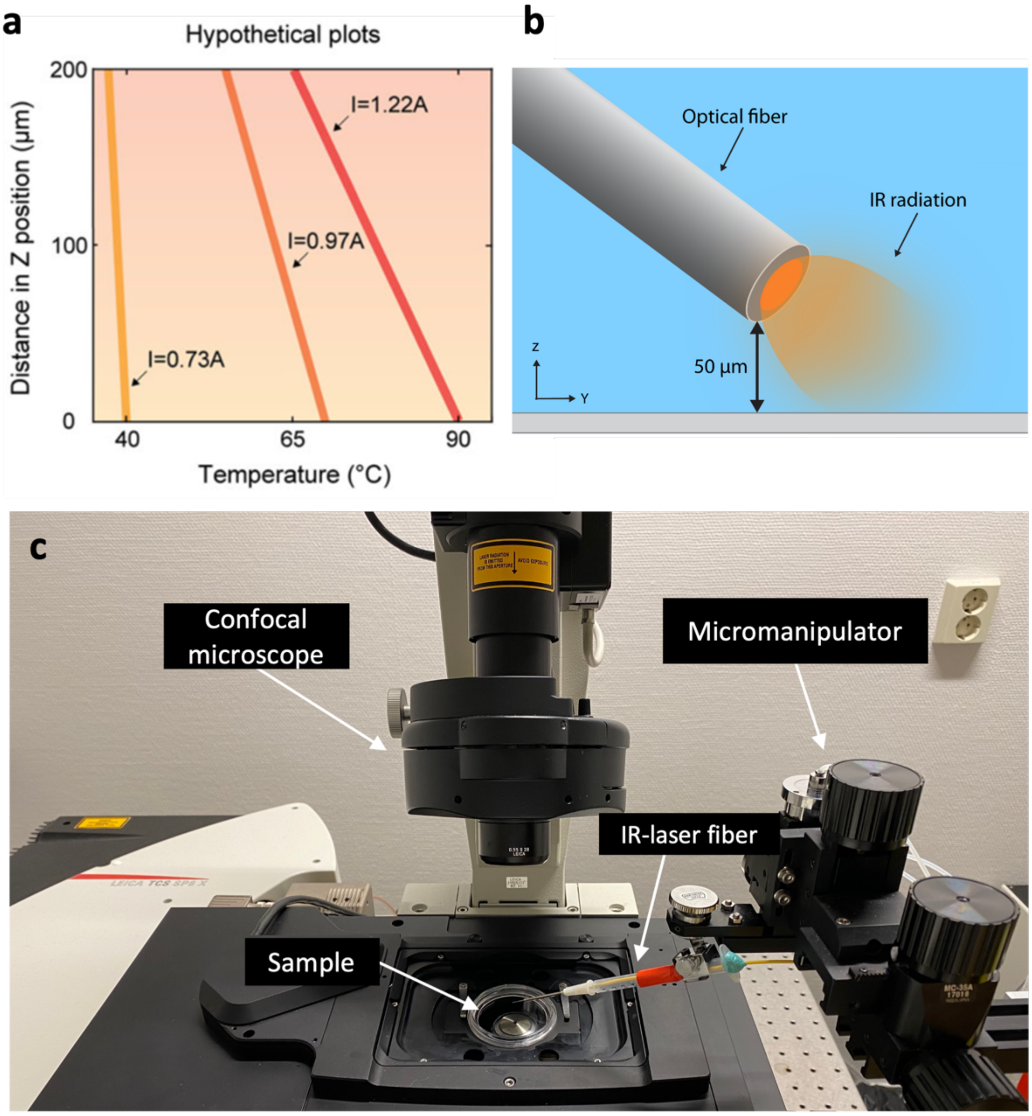

Figure 32: (a) Plot over the relation between the temperature and distance in z-position for the different currents. (b) Illustration of the IR-laser optical fiber submerged in aqueous solution positioned 50 µm above the surface. (c) Confocal microscope set-up with an IR-laser mounted to a micromanipulator. Adapted with permission[85]. Copyright 2022, Springer Science+Business Media, LLC, Springer Nature.

The current can be set at 0.48, 0.73, 0.97 or 1.22 A. The IR-laser fiber is mounted onto a 3-axis water hydraulic micromanipulator by Narishige. The tip is positioned in a 30–45-degree angle approximately 50 µm above the sample surface (**Figure 32b**). The laser beam projection is conically shaped, i.e. the cone of acceptance.

2.13 Imaging

2.13.1 Digital Light Microscopy

The droplet formation during cDICE was monitored by a digital light microscope. Digital light microscopes work by the same principles as traditional light microscopes but use a sensor in a digital camera in place of an eyepiece to capture still images or record videos. Digital microscopes can achieve higher resolution images than what is generally seen with the human eye[86]. We employ an infinity-corrected optical system that consists of four components: a C-mount camera, an extension tube, tube lens and objective lens. In contrast to finite correction optical systems, where the light is focused directly onto the sensor and the objective forms an intermediate image by itself, infinity-corrected systems require a tube lens between the objective lens and the sensor to create an intermediate image and focus the light into the sensor. The light beam transmitted from the specimen passes through the infinity corrected objective lens, exits as an infinity parallel beam and forms an intermediate image after passing through the tube lens (**Figure 33a**)[87].

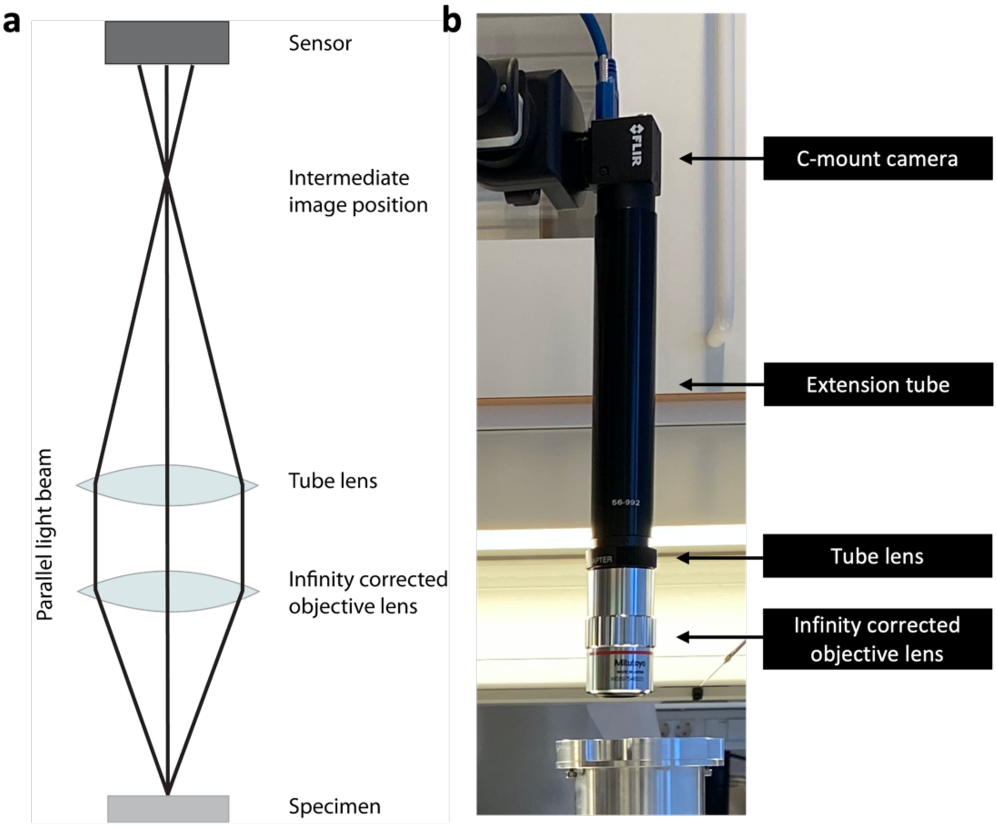

Figure 33: (a) Scheme of the pathway of light in an infinity corrected system. (b) Photograph of the digital light microscope set-up.

The components for the digital camera were purchased from Edmund Optics. The microscope is composed of the FLIR Flea®3 FL3-U3-13E4M-C 1/1.8" Monochrome USB 3.0 CMOS Camera, Mitutoyo to C-mount Camera 152.5 mm Extension Tube, the MT-4 Accessory Tube Lens and 5x Mitutoyo Plan Apo Infinity Corrected Long WD Objective lens (**Figure 33b**). The four-component system is optimized for 5x magnification and where the highest resolution is 1280 x 1024 (1.3 MP) pixels at a frame rate of 60 frames per second (fps). The camera is connected to a computer via a USB 3.0 cable and is controlled using the Spinnaker software from FLIR.

2.13.2 Laser Scanning Confocal Microscopy

The GUVs were visualized by laser scanning confocal microscopy (LSCM). The lipid membranes were fluorescently labeled by fluorophore-conjugated lipid molecules. The electrons of fluorophores are capable of absorbing the energy of photons of specific wavelengths and become excited into a higher energy state (S1), as illustrated in the Jablonski diagram in **Figure 34a**.

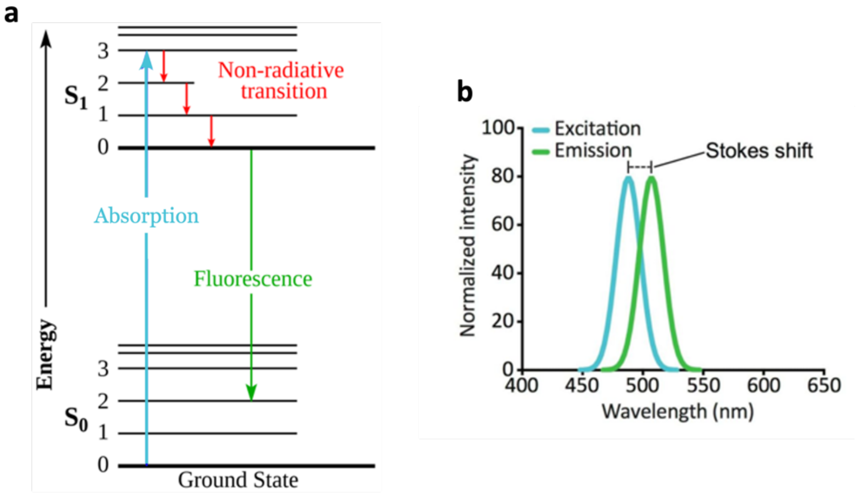

Figure 34: (a) Jablonski diagram. (b) Excitation and emission spectra. Image reused from [88].Copyright 2022, Science Squared.

This process is known as excitation. The electrons are unstable in the excited state and will return back to their ground state (S0). During this process, they emit photons of lower energy (longer wavelength) as fluorescence. This process is called emission[88]. The difference between the peaks of the excitation and emission spectra is known as the Stokes shift (**Figure 34b**) and varies from one fluorophore to another. Commonly, large Stokes shifts are advantageous as the excited and emitted light are more easily separated[89].

We used an inverted LCSM microscope (Lecia DMi8) with illumination provided by an argon- or white light laser. The images were acquired by using a 40X oil immersion objective (1.3 NA). The light from the light source is filtered out by the excitation filter which only transmits wavelengths that are able to excite the sample (**Figure 35**)[88]. The emitted fluorescence passes through the emission filter and is then collected by the eyepiece or camera. In contrast to widefield microscopes, confocal microscopes employ a spatial pinhole to block the out-of-focus- and background fluorescence[90].

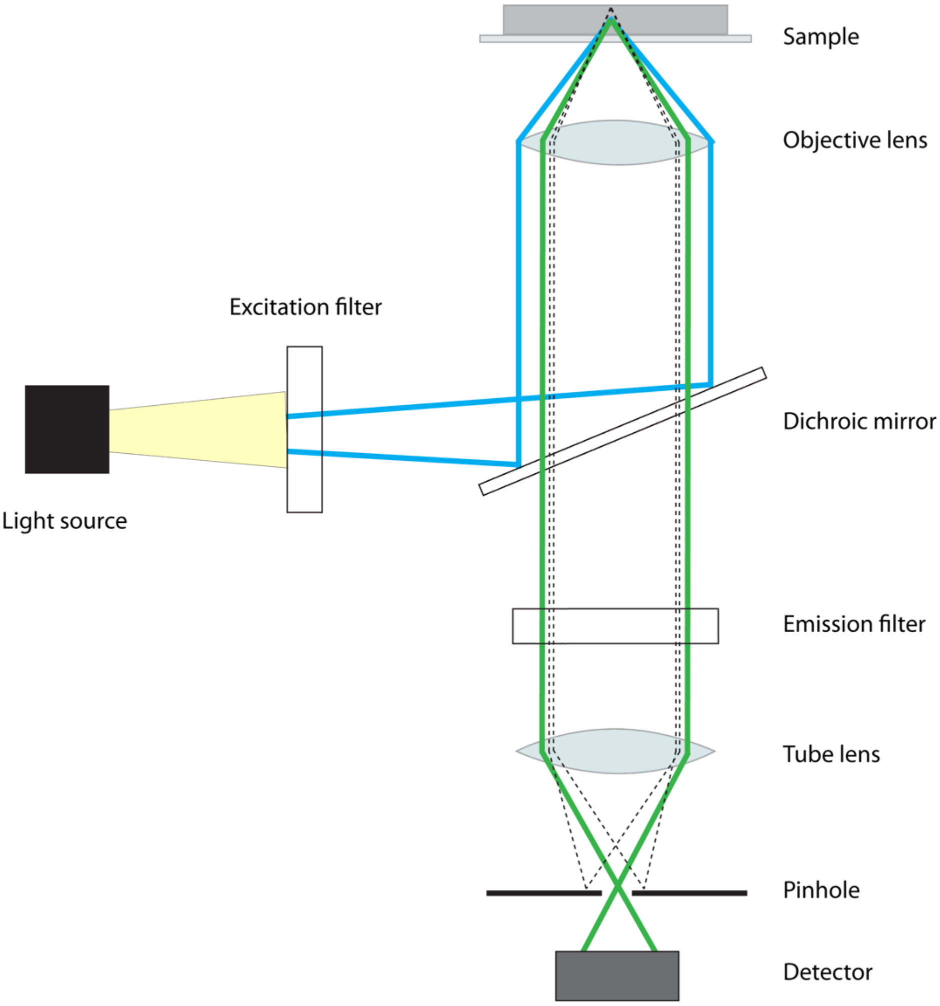

Figure 35: Pathway of light in an inverted confocal microscope.

This way, images of high optical resolution and contrast are created. Only a cross-section of the specimen in the xy-plane is illuminated and a translated image is generated. These cross-sections can be used to reconstruct a three-dimensional image of the sample, in a process known as optical sectioning[90].

2.14 Image Analysis

The images and videos were analyzed using Fiji (ImageJ). The diameter of the GUVs were measured by manually drawing the ROI by hand and measuring the area of the ROIs. The values for the areas were then used to calculate the diameter of the spherical vesicles. The contours of the clusters in **Figure 55-65** were drawn manually while the contours of clusters during formation and during the heat pulses, were detected completely by using the software. The digital measurement was done by converting the images to grayscale (8-bit), adjusting the "threshold", and selecting the edge of the cluster by using the "wand" tool. The areas of the clusters were then measured by using the "measure" tool.

3 Results and Discussion

3.1 Generation of GUVs

GUVs Formed Without a Density Gradient

The first successful cDICE experiment was performed following the protocol for LOS modified from Abkarian et al.[50]. The GUV membranes were composed of POPC and the fluorescence label Liss Rhod PE. 100 mM glucose solution was used as both IAS and OAS, and decane as the medium in which the initial droplets were injected from the capillary. The sample was observed the following day in a confocal microscope. As seen in the images in **Figure 36**, several tens of GUVs, with an average diameter of 6 µm, were formed. Most of the GUVs contained artifacts, such as internal compartments or were at a hemifused state with one or more GUVs (white arrows **Figure 36a**). GUVs were generated even though a density contrast between the IAS and OAS was not used.

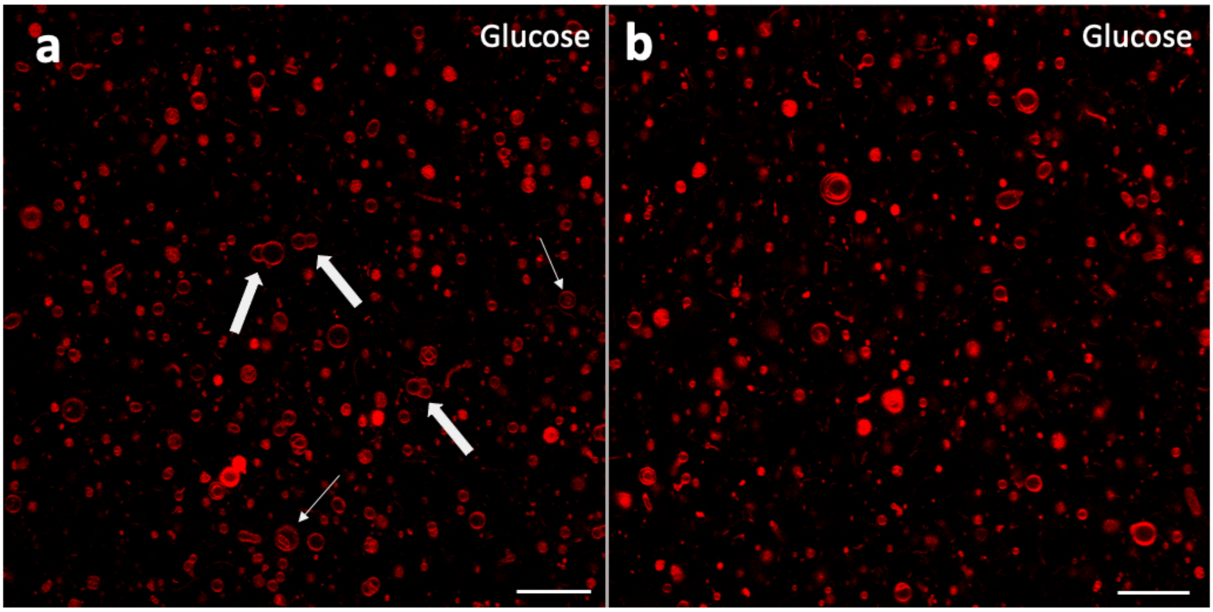

Figure 36: GUVs encapsulating 100 mM glucose solution (same as ambient solution). Many of the GUVs in both (a) and (b) contain artifacts. (a) The thick arrows point to hemifused GUVs and the thin arrows point to GUVs with internal compartments. Scale bars are 25 µm.

GUVs Formed in a Sucrose-Glucose Density Gradient

Next, the protocol by Van de Cauter et al.[51] was followed. The GUVs were also made of POPC and the fluorescence label Liss Rhod PE, with 100 mM sucrose solution as IAS versus 100 mM glucose solution as the OAS. Sucrose has a molar mass of 342.30 g/mol and is heavier than glucose, which has a molar mass of 180.156 g/mol. This makes the IAS denser and heavier compared to the OAS. The results indicate that GUVs encapsulating sucrose solution (**Figure 37**) appear to have a larger average diameter compared to the ones encapsulating glucose solution (d=13 µm vs. d=6 µm). In cDICE, the vesicle generation is directly dependent on droplet formation from the capillary. In principle, cDICE should provide a monodisperse GUV suspension, if all parameters such as flow rate, injection time and sample volume, are the same. However even though the above-mentioned parameters are optimal, the structure of the tip of the capillaries, which are manually cut, may influence the droplet formation. This occasionally prevents the formation of uniform droplets. This could be the reason leading to the polydisperse vesicles in **Figure 37**. Images from the vesicle samples shown in **Figure 37** are diluted in the glucose buffer in order to prepare the imaging chamber.

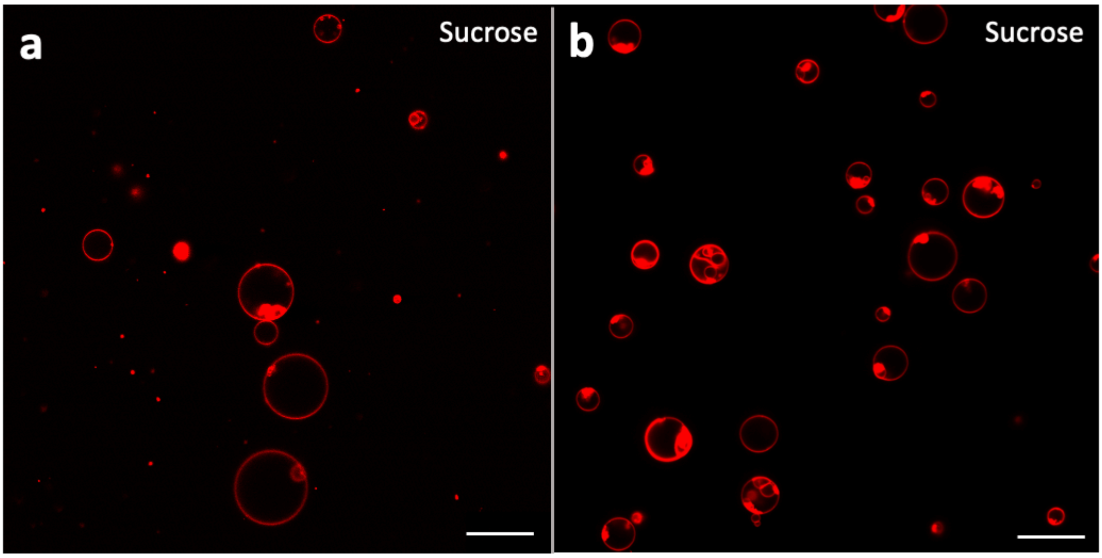

Figure 37: Two different samples of GUVs encapsulating 100 mM sucrose solution. Scale bars are 25 µm.

GUVs Formed in an Iodixanol-Glucose Density Gradient

Iodixanol is a large and heavy molecule with a molar mass of 1550.191 g/mol. It has been used as a density gradient medium in other studies employing the cDICE technique[51, 78]. This method was the most efficient for forming vesicles without any internal components, i.e. highest conversion of droplets to vesicles. The GUVs generated with this method were used as control experiments and the results are shown in the following section in **Figure 48-51**.

3.2 Encapsulation of PNIPAAm and Thermal Manipulation of the GUVs

Aqueous solution of linear PNIPAAm homopolymer was encapsulated in GUVs made by following the protocol for cDICE adapted from Van de Cauter et al.[51]. There were some areas on the surface with a lower number of vesicles (**Figure 38a**) while other areas were more densely packed (**Figure 38b** and **c**). The corresponding bright field images of GUVs encapsulating PNIPAAm sol in an environment below the LCST of PNIPAAm (~20°C), are depicted in **Figure 38a'-c'**.

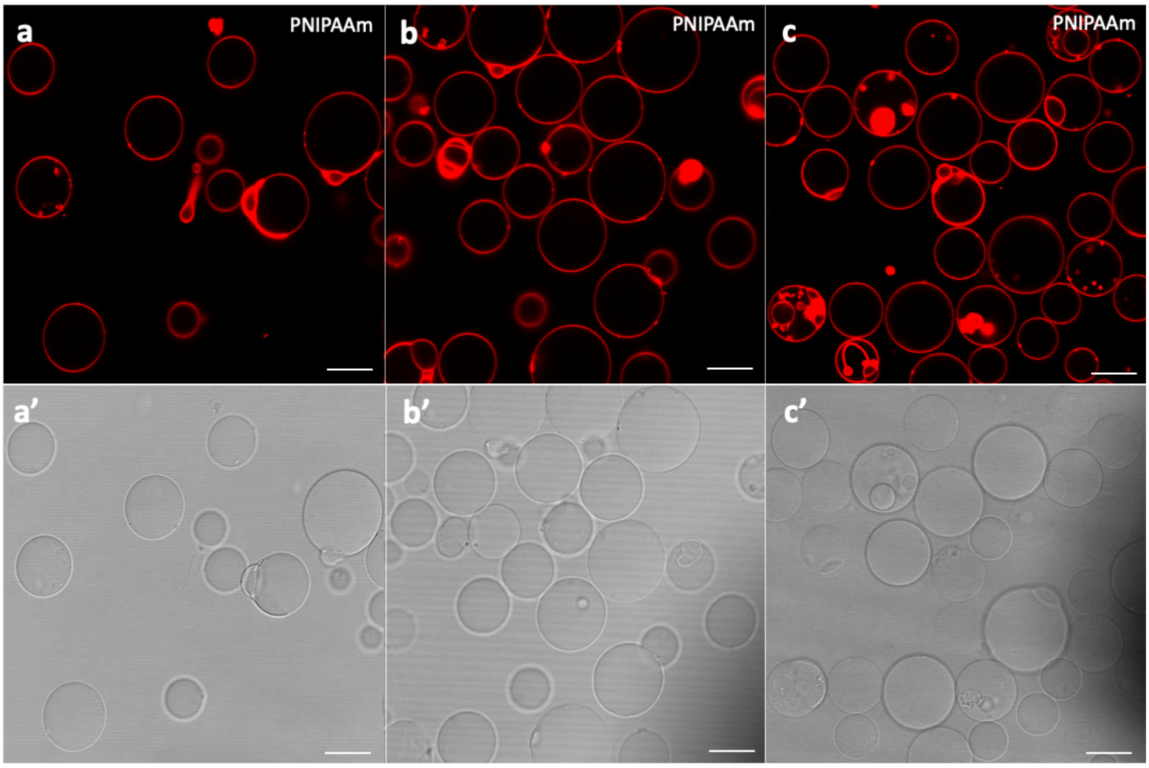

Figure 38: GUVs filled with 1 mM PNIPAAm sol. Large GUVs with few artifacts in the membrane was produced when encapsulating PNIPAAm. (a-c) Fluorescence-, (a'-c') bright field microscopy images. Scale bars are 25 μm.

3.2.1 Cluster Formation with Thermal Stimuli

The thermal manipulation of the PNIPAAm-encapsulating vesicle clusters was conducted by positioning the IR-laser 50 µm above a GUV in the sample and locally heating the volume beneath the laser to 40 °C, a temperature higher than the LCST. The optical fiber-tip is visualized in the bright-field channel and is seen as a dark shadow in the bright-field micrographs. A clustering phenomenon was observed when the heat was turned on. We observed that the vesicles started to move rapidly towards the heated spot, got trapped in this area, and eventually formed a cluster (**Figure 39**). Seven different clusters from two samples have been characterized (P1-P7) in the scope of this thesis. The formation of these clusters has been depicted in **Figure 39-45** (corresponding to P1-P7). Since the time it took from the activation of the laser to formation of a cluster varied a lot between the experiments, time zero has been set to the timepoint when the first two GUVs gather and get trapped.

When the vesicles entered the area of higher temperature, the appearance of their internal volume changed from clear (**Figure 38a'-c')** to a darker, grainy phase (bright field images **Figure 39-45)**. This change can be attributed to the phase transitioning of PNIPAAm[39] and confirms that PNIPAAm was successfully encapsulated inside these vesicles.

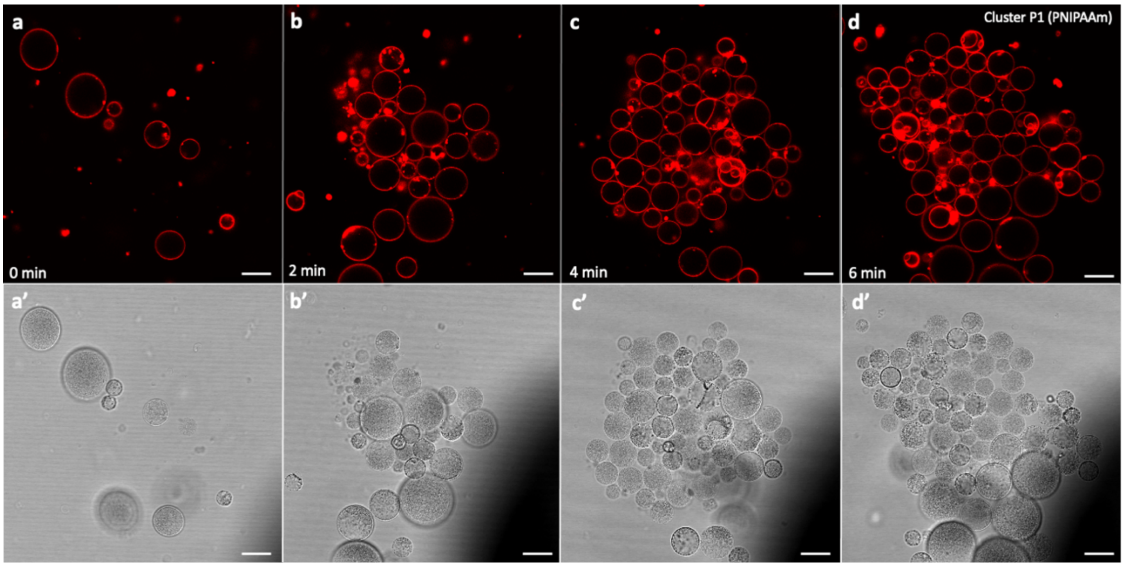

Figure 39: Cluster P1 formed by GUVs encapsulating 1 mM PNIPAAm. (a-d) Fluorescence-, (a'-d') bright field microscopy images. Scale bars are 25 µm.

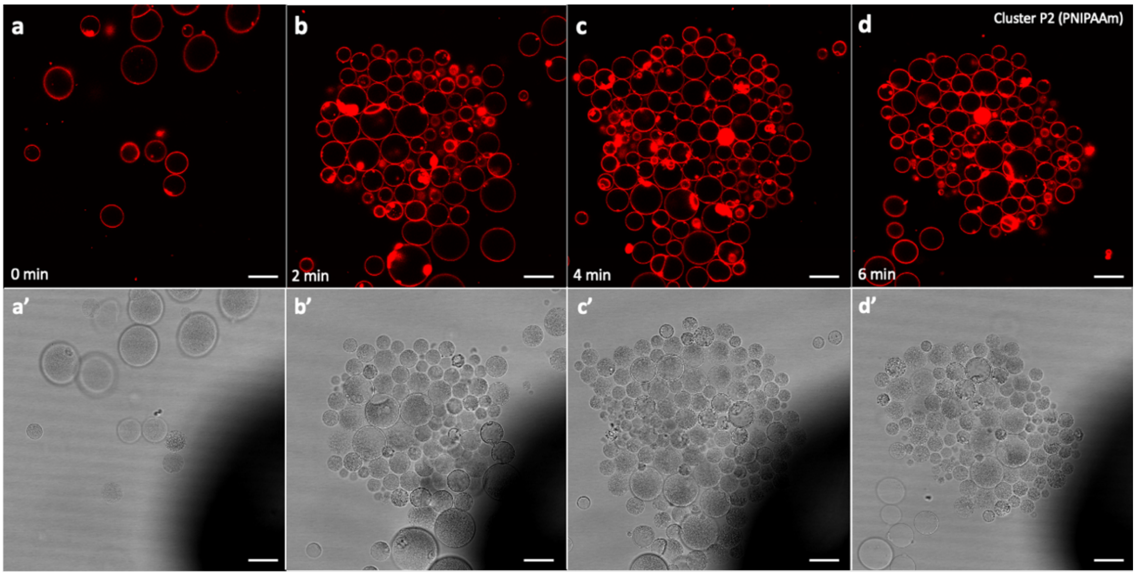

Figure 40: Cluster P2 formed by GUVs encapsulating 1 mM PNIPAAm. (a-d) Fluorescence-, (a'-d') bright field microscopy images. Scale bars are 25 μm.

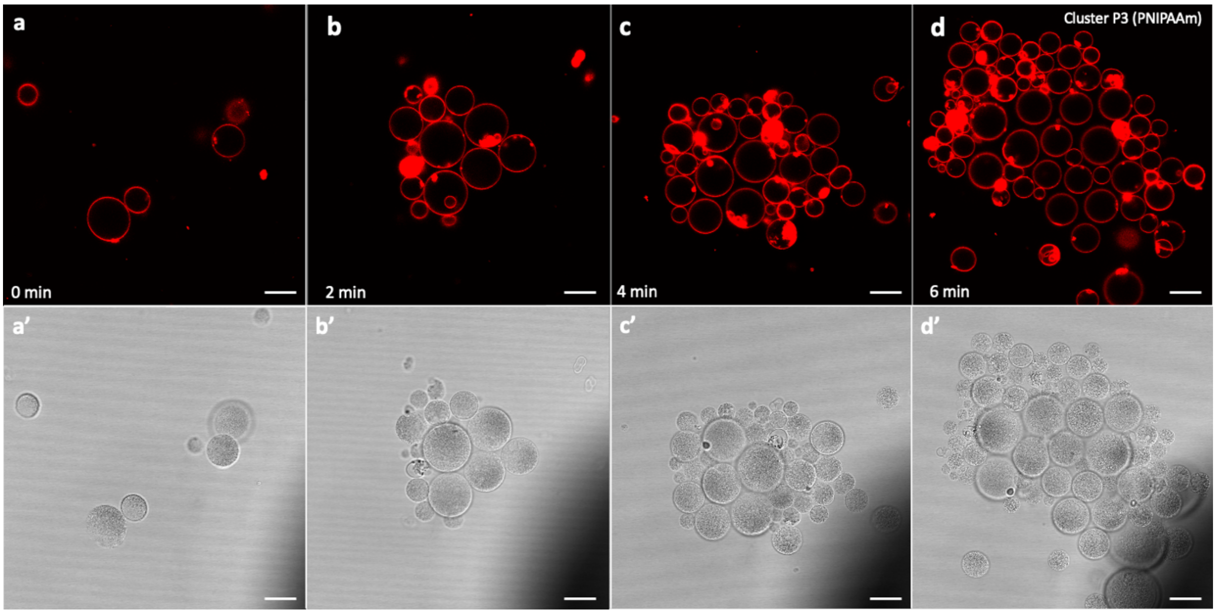

Figure 41: Cluster P3 formed by GUVs encapsulating 1 mM PNIPAAm. (a-d) Fluorescence-, (a'-d') bright field microscopy images. Scale bars are 25 *µ*m.

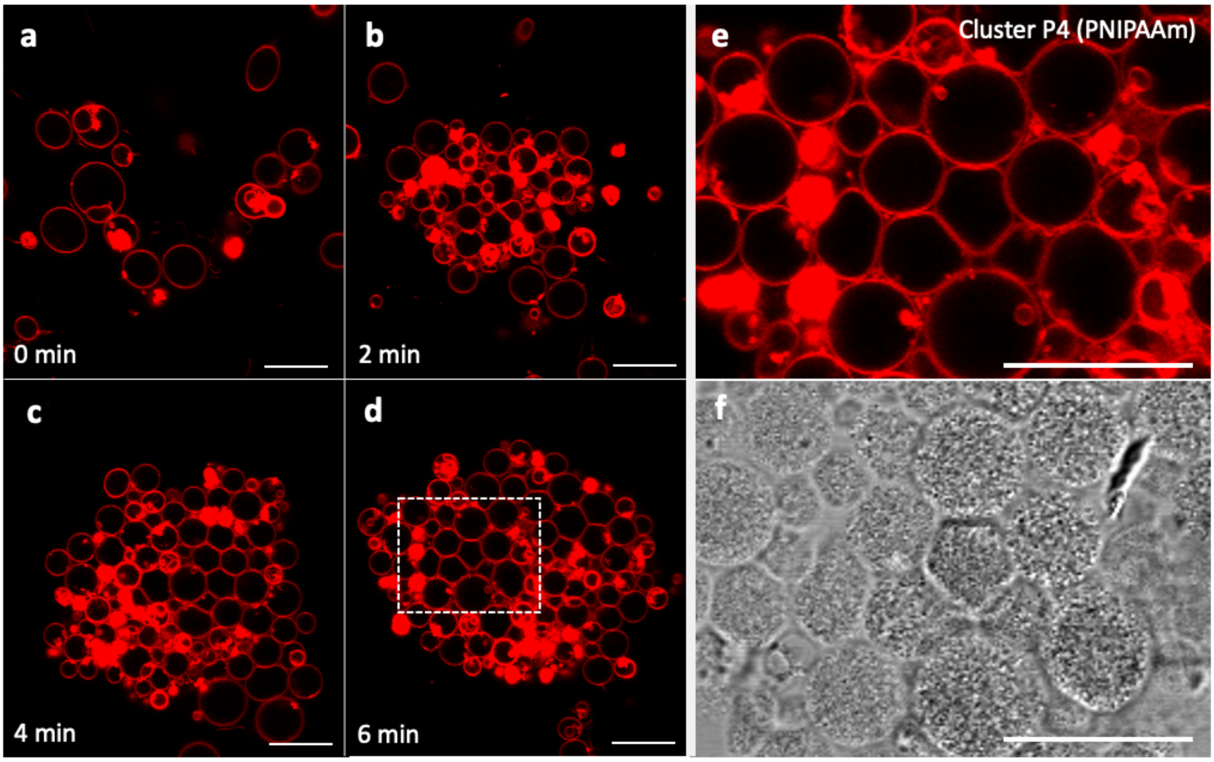

Figure 42: Cluster P4 formed by GUVs encapsulating 1 mM PNIPAAm. (a, b, d, e) The formation of cluster C4 over time. The area inside the dashed square in e) is enlarged in c) and f), where membrane deformation is visible. Scale bars are 25 µm.

The size of the clusters, the number of vesicles composing the cluster and the size of these vesicles varies from cluster to cluster. The detailed analysis will be shown in the following sections. The GUVs in cluster P4 and P5 appear to be mechanically pushed together to the extent that the vesicles are deformed (**Figure 42e, f**). Moreover, the clusters seem to adopt and maintain a circular shape during growth following the cone of acceptance of the optical fiber projecting the IR-laser beam.

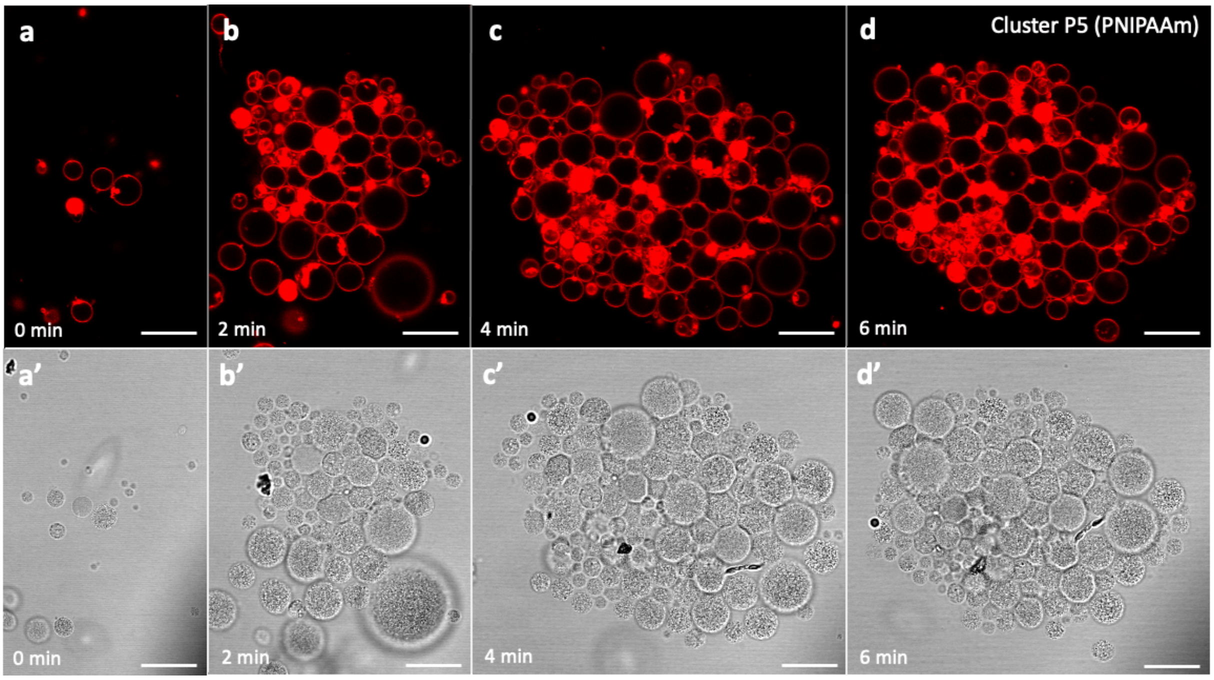

Figure 43: Cluster P5 formed by GUVs encapsulating 1 mM PNIPAAm. (a-d) Fluorescence-, (a'-d') bright field microscopy images. Scale bars are 25 µm.

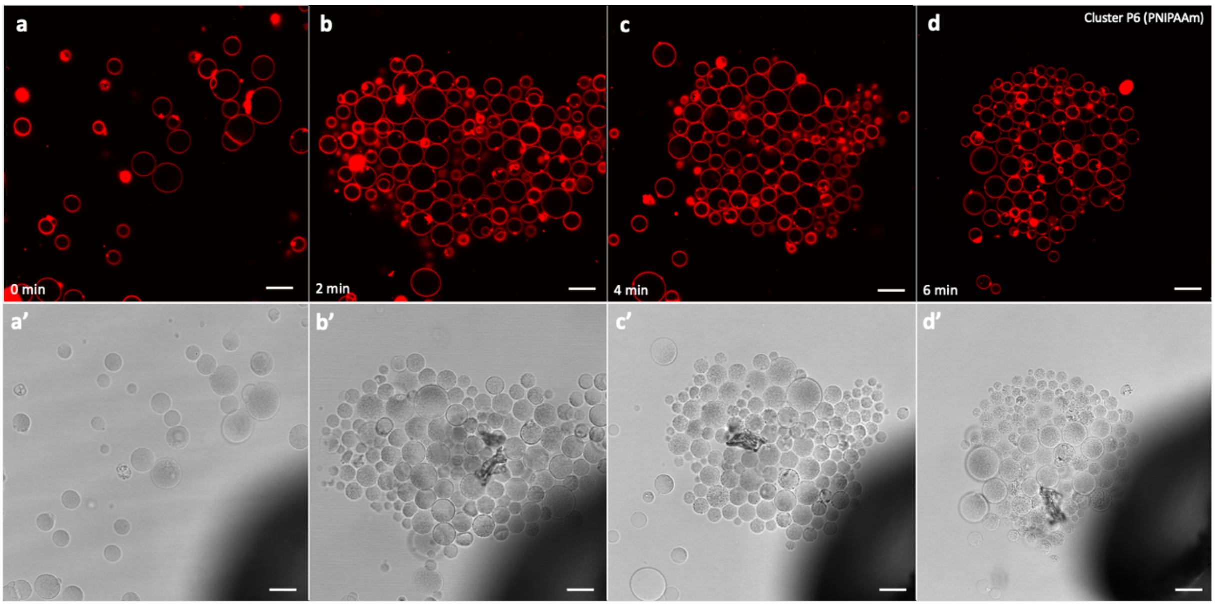

Figure 44: Cluster P6 formed by GUVs encapsulating 1 mM PNIPAAm. (a-d) Fluorescence-, (a'-d') bright field microscopy images. Scale bars are 25 µm.

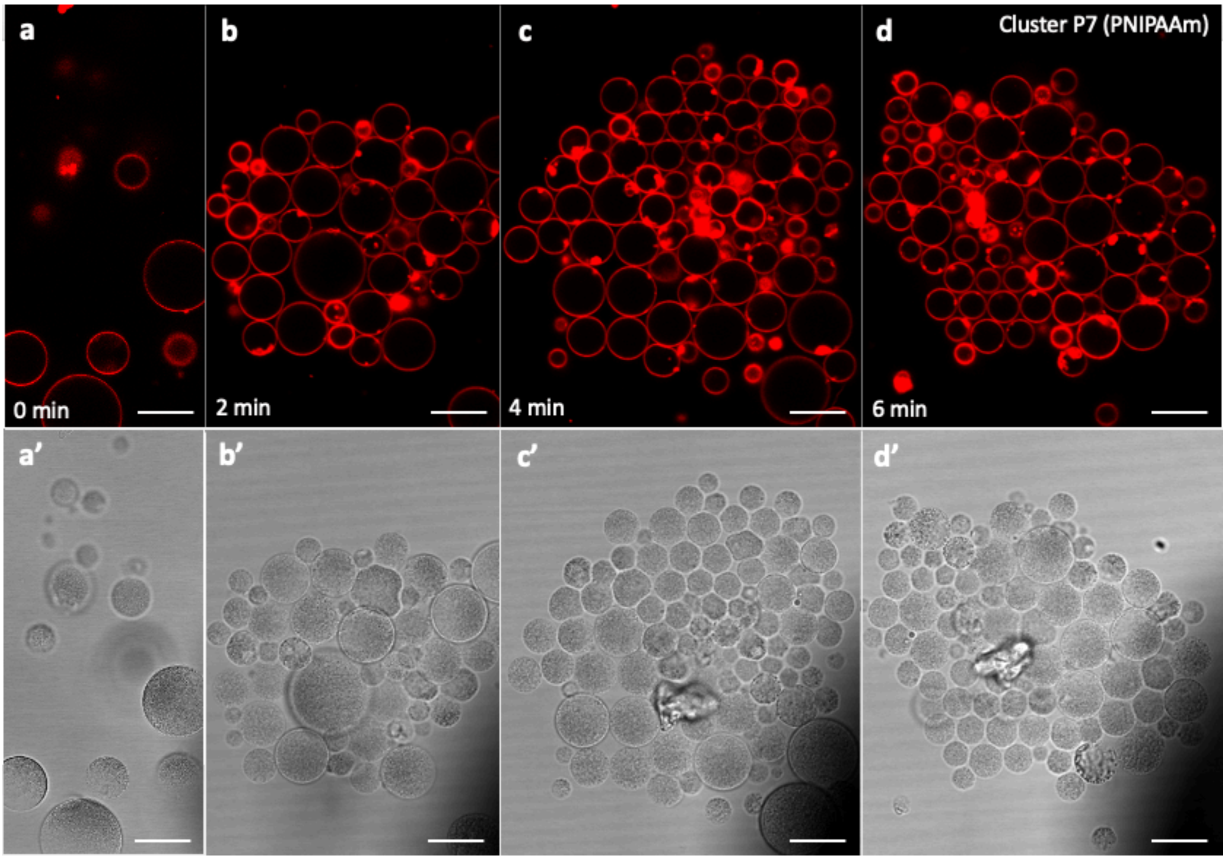

Figure 45: Cluster P7 formed by GUVs encapsulating 1 mM PNIPAAm. (a-d) Fluorescence-, (a'-d') bright field microscopy images. Scale bars are 25 µm.

All the clusters display counterclockwise axial rotation in the xy-plane. The rotation of cluster P1 is shown in **Figure 46**.

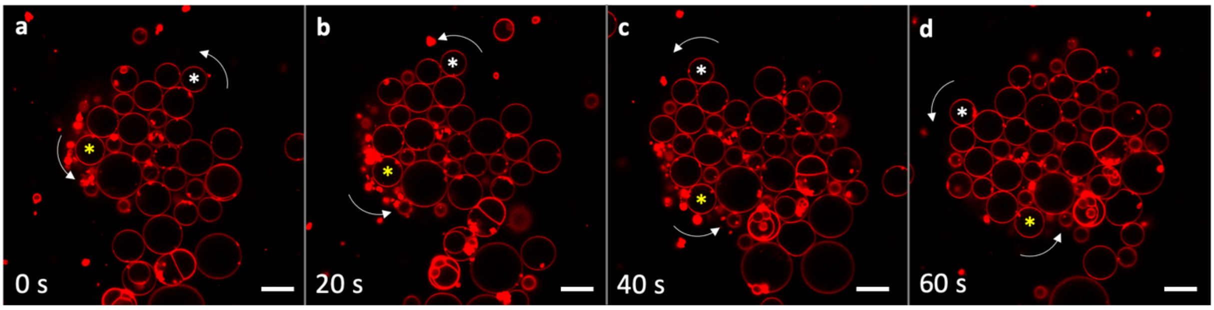

Figure 46: Rotation of cluster P1 over a 1-minute timeframe. The position of two specific vesicles in the cluster is marked with asterisks (white and yellow). The direction of rotation is indicated with curved arrows. Scale bars are 25 µm.

* * *

The growth of the clusters was quantified by measuring the increase in the total area of the clusters in 2D (xy-plane) over time. The growth of each cluster versus time is plotted and shown in **Figure 47**.

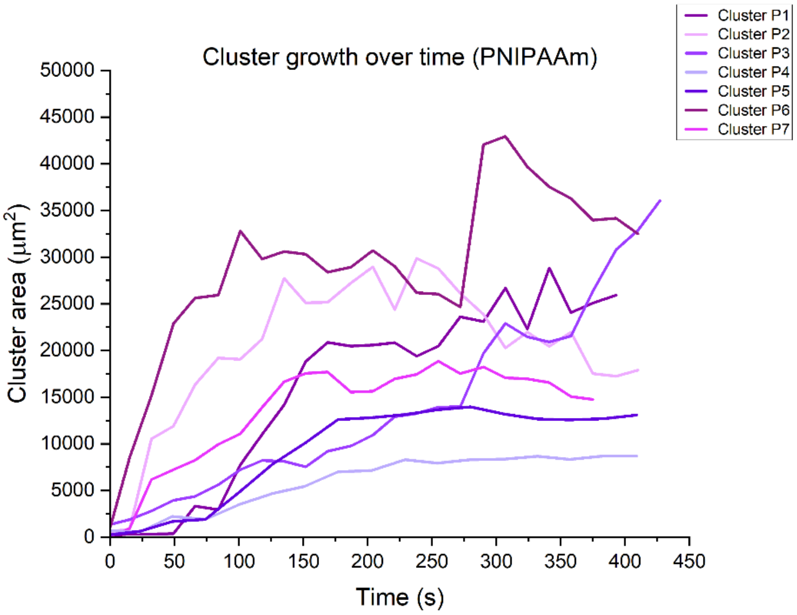

Figure 47: Graphs of cluster area over time for PNIPAAm-encapsulating vesicle clusters.

Clusters P4 and P5 appear to have the slowest growth leading to clusters with small diameters. The vesicles in these clusters are mostly deformed i.e. honeycomb-like manner, indicating that relatively high number of vesicles have been concentrated in a locally heated area. The more the vesicles are squeezed into the heated volume, the less the expansion of the cluster. More concentrated clusters (honeycomb-like structure) can be formed due to a stronger heat gradient. The strength of the heating is highly dependent on the exact position of the IR-B laser fiber with respect to the surface. Slight differences in the height of the laser fiber tip from the surface may affect the temperature gradient it creates[91]. If the tip is further above the surface, the temperature profile might expand over a larger area. This can cause the size of the clusters and the density of the vesicles in each cluster to vary.

Control Experiments

Control experiments were performed to assess whether cluster formation was exclusive to PNIPAAm-encapsulating vesicle clusters and was happening due to the thermoresponsive properties of the encapsulated polymer, or if it would occur in GUVs without PNIPAAm as well. GUVs encapsulating 100 mM iodixanol were locally heated by the same parameters as the PNIPAAm-encapsulating GUVs (T= 40 °C). The formation of clusters was observed also in the control experiments. Four different clusters from one sample were characterized (C1-C4). Their formation is shown in **Figure 48-51**.

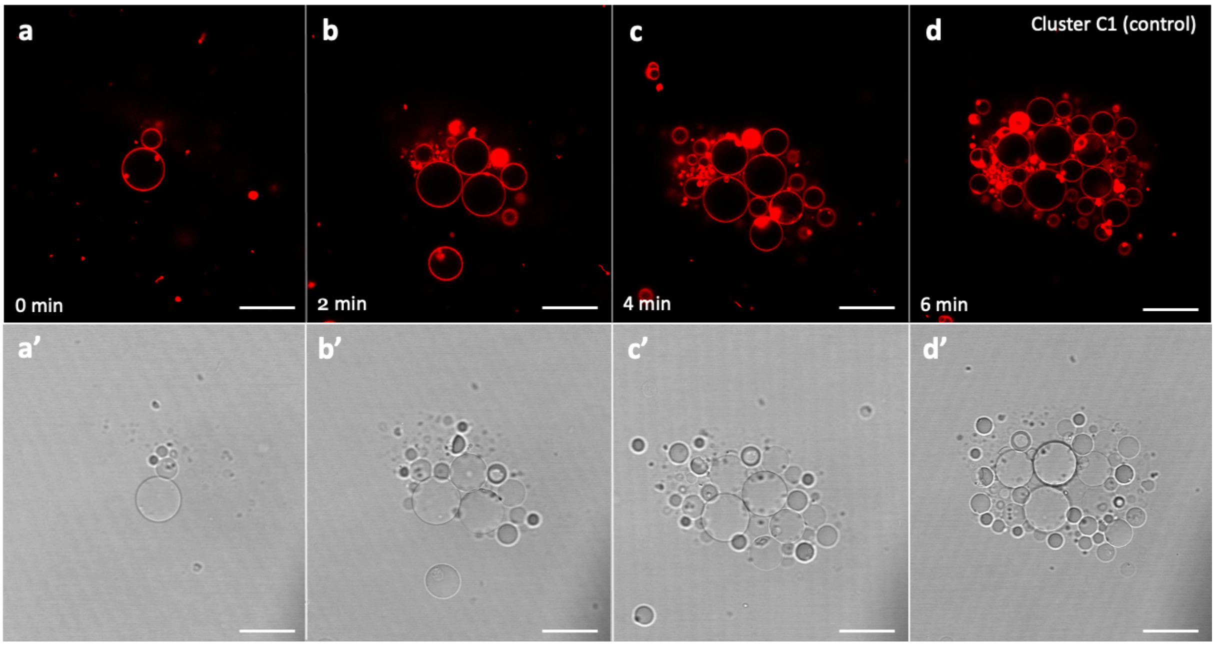

Figure 48: Formation of cluster C1 during local heating. Scale bars are 25 µm.

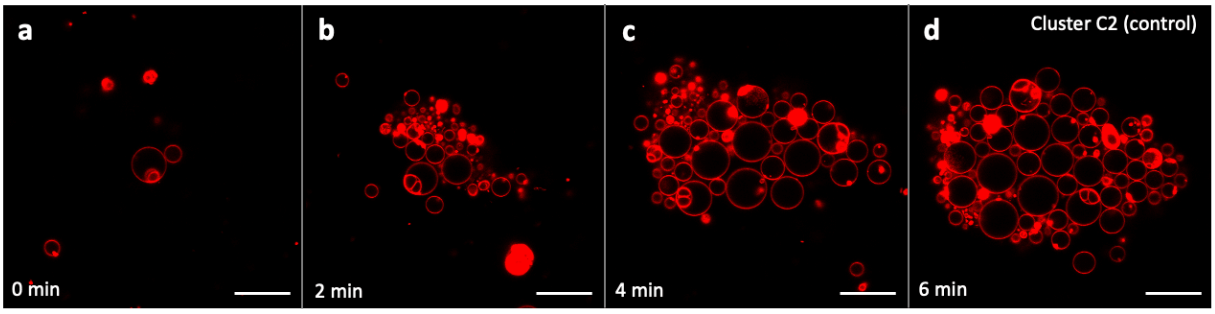

Figure 49: Formation of cluster C2 during local heating. Scale bars are 25 µm.

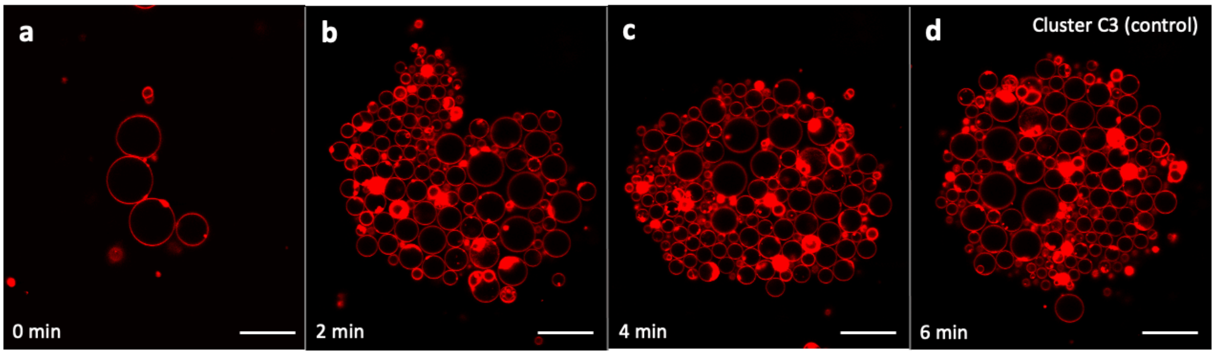

Figure 50: Formation of cluster C3 during local heating. Scale bars are 25 µm.

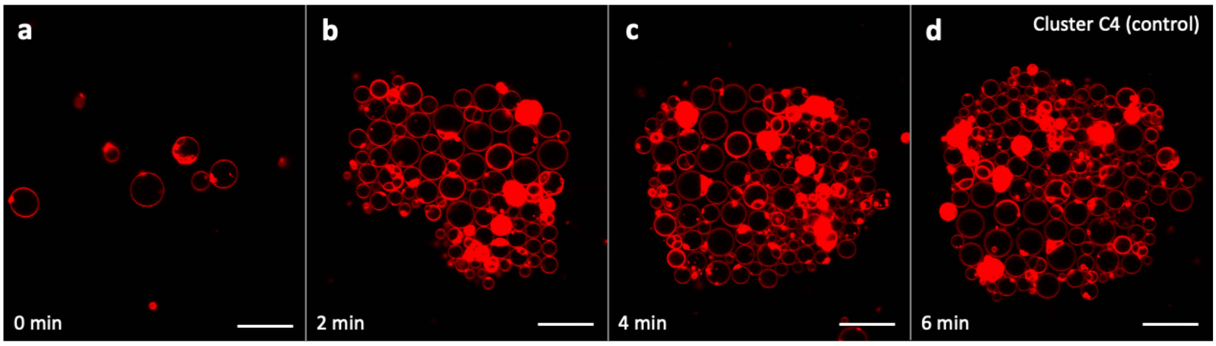

Figure 51: Formation of cluster C4 during local heating. Scale bars are 25 µm.

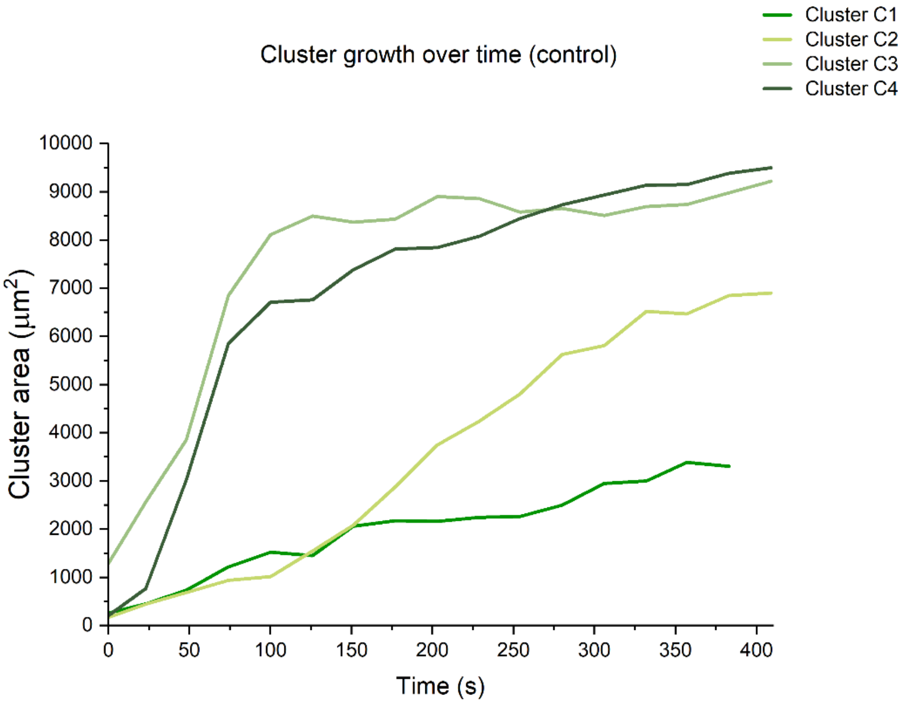

Figure 52: Plot of cluster growth over time for the control experiments.

The formation for the control-clusters is similar to the PNIPAAm-encapsulating clusters but appears to occur in two different modes. In the plot in **Figure 52**, we see that cluster C1 and C2 have a slower, linear growth, while C3 and C4 have a rapid growth from 0 to 2 min, as seen in **Figure 50** and **51.** Clusters C3 and C4 have adopted a highly circular shape. This can be due to the position of the laser fiber tip (cf. discussion above) and also due to the density of the vesicles around the fiber tip at t=0. Some areas in the imaging chamber are more densely packed with vesicles compared to other, relatively dilute areas. Therefore, a randomly selected position in the sample to initiate heating, may lead to differences in the assembly time of the clusters.

3.2.2 Size Distribution of GUVs in the Clusters

The cluster area was defined as the area of the cluster right before turning off the heating. All of the clusters were grown over a 7-minute timeframe. The assembly of the vesicles to the clusters was continuous as long as the heating was maintained, i.e. new vesicles were joining the clusters over time during heating. In order to precisely calculate the cluster size, we distinguished the vesicles in the cluster from those outside it, based on the phase separation. If the internal volume of a vesicle at the edge of the cluster is not exhibiting phase separation at the end of the 7 minutes, it meant that the vesicle was not yet inside the effective heating zone therefore we did not count this vesicle as part of the cluster. The area calculation only took into account the vesicles which were physically in contact and exhibited phase separation.

The vesicle size distribution analysis for each cluster is shown in the histograms in **Figure 53**.

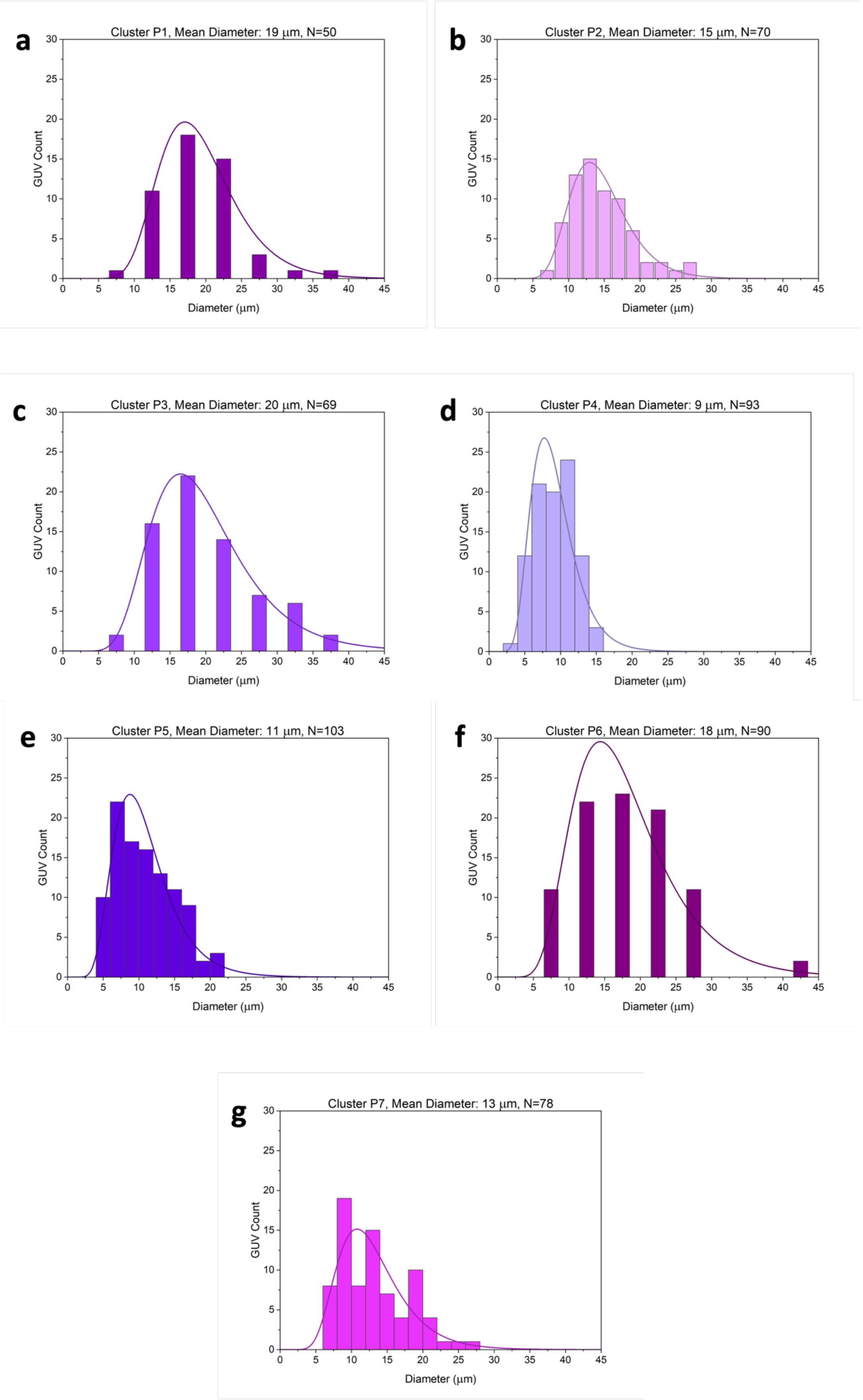

Figure 53: Size distribution of PNIPAAm-encapsulating GUVs within each of the clusters. (a-g) corresponds to P1-P7.

The size of the GUVs in the clusters ranged from 5 to 40 µm and follows a log-normal distribution. Their average diameter is 15 µm. The clusters are densely packed with small vesicles occupying the space in between larger vesicles.

Control Experiments

The histograms for the GUV size distribution of the control-clusters are shown in **Figure 54**.

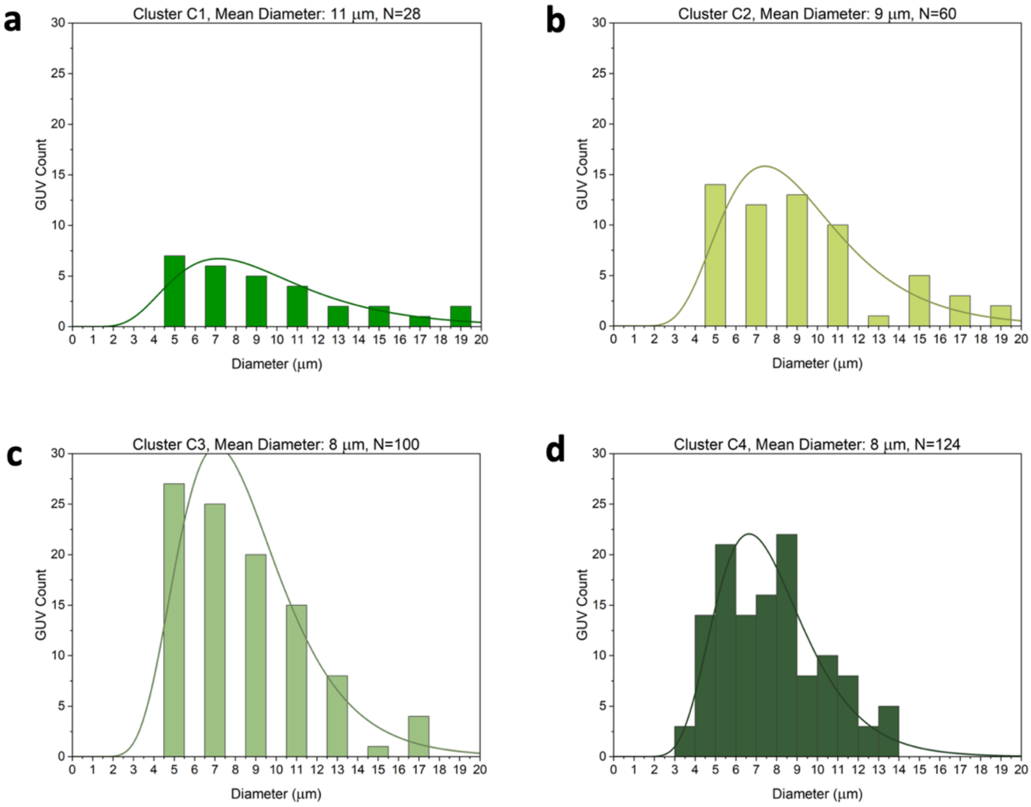

Figure 54: Size distribution analysis of GUVs in the control-clusters. (a-d) corresponds to C1-C4.

The average diameter of the GUVs in the clusters from the control experiments are comparable to the diameter of the PNIPAAm encapsulating GUVs. However, they are relatively smaller in size: the whole size range of aqueous solution-containing vesicles in clusters, ranged from 5-20 µm, versus 5-40 µm in PNIPAAm-encapsulating vesicles in clusters. The average diameter of the vesicles composing the clusters in the control experiments is 9 µm (N=312) vs. 15 µm (N=328) for the PNIPAAm-encapsulating vesicle clusters.

3.2.3 Disintegration of Clusters and the Impact of PNIPAAm on Cluster Integrity

The clusters were grown over a 7-minute timeframe following the termination of heating. This resulted in the expansion of the clusters and in the case of PNIPAAm, the rapid reverse transition of the PNIPAAm back to the sol phase. The following figures show the images of the clusters the second before the termination of the laser and 14 seconds after the laser had been turned off (**Figure 55-61**).

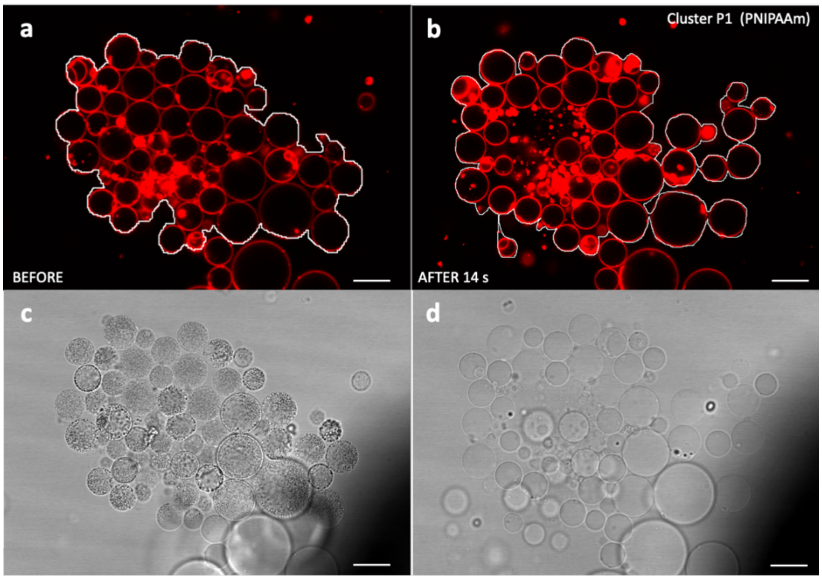

Figure 55: Disintegration of cluster P1. Scale bars are 25 µm.

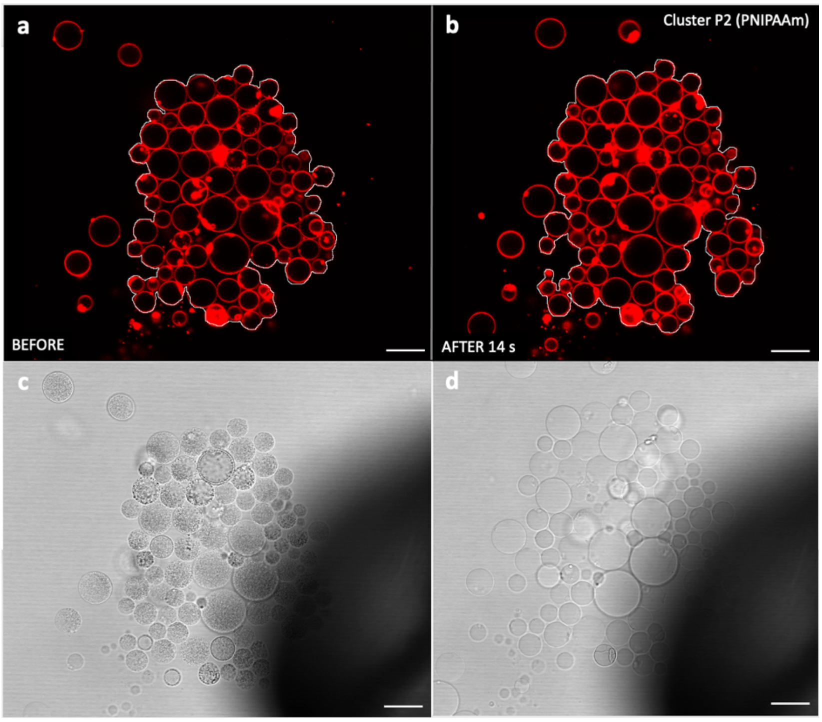

Figure 56: Disintegration of cluster P2. Scale bars are 25 µm.

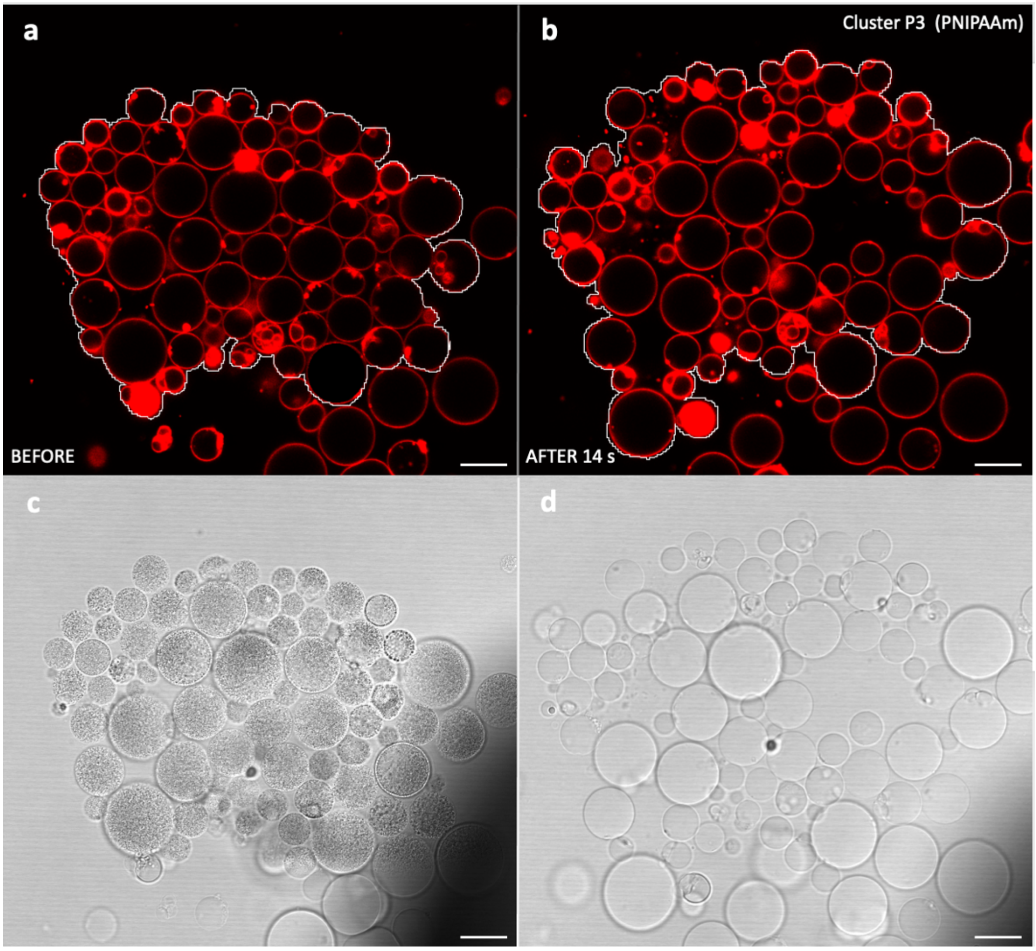

Figure 57: Disintegration of cluster P3. Scale bars are 25 µm.

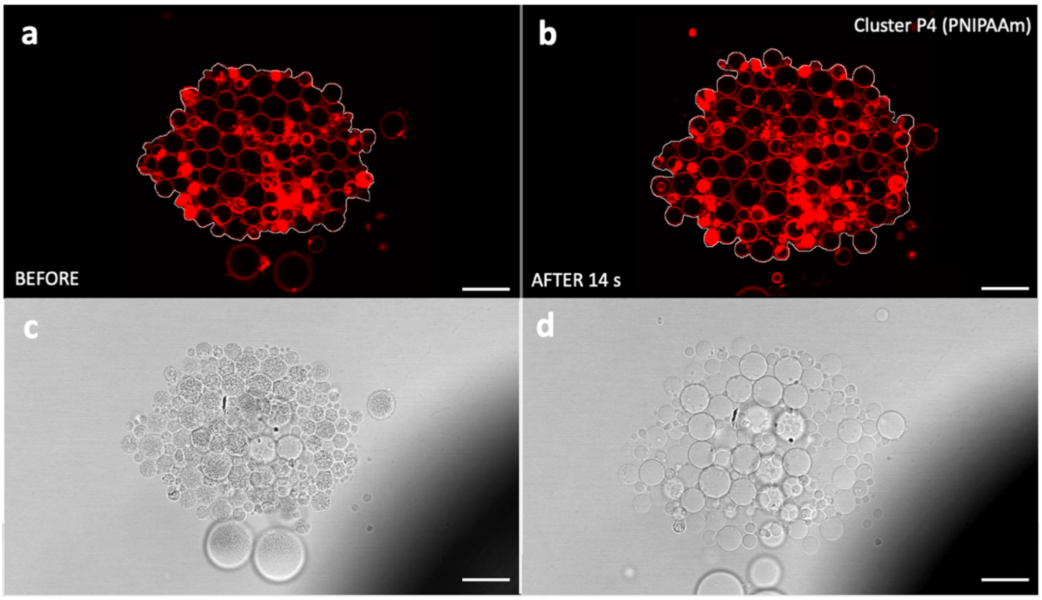

Figure 58: Disintegration of cluster P4. Scale bars are 25 µm.

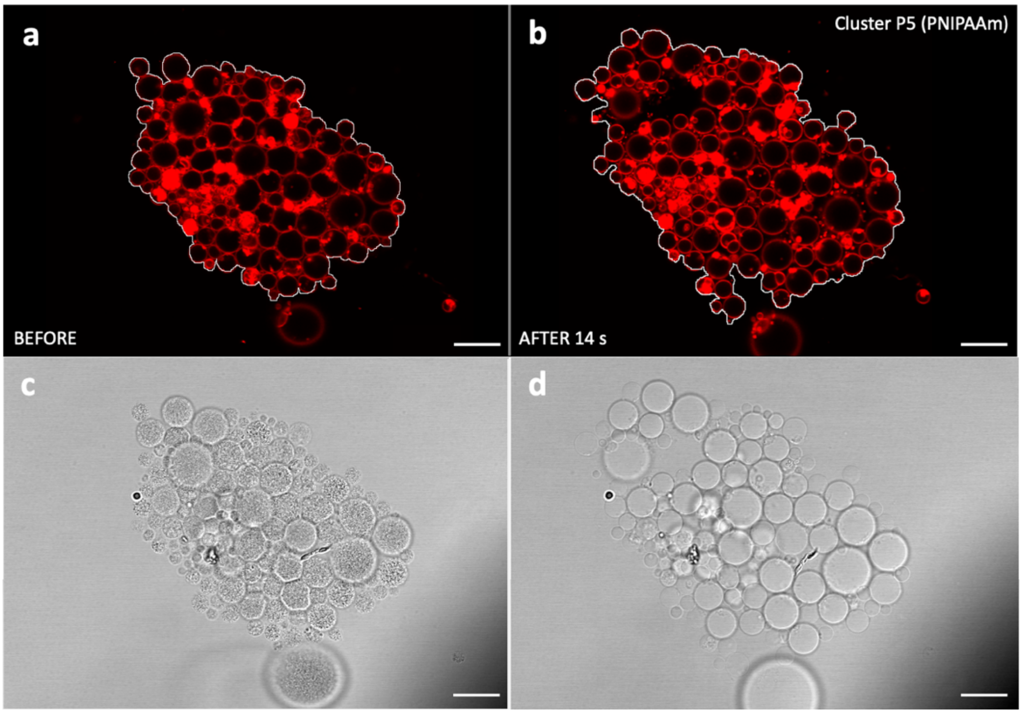

Figure 59: Disintegration of cluster P5. Scale bars are 25 µm.

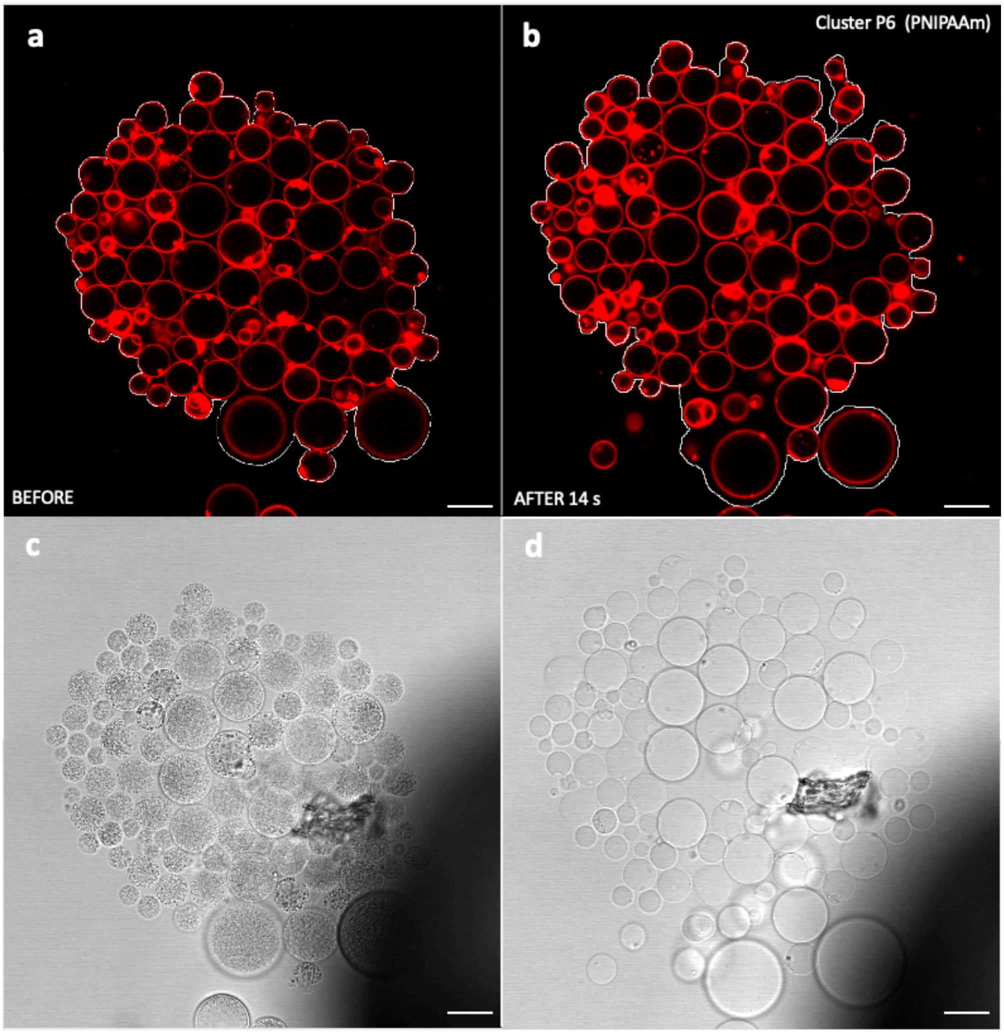

Figure 60: Disintegration of cluster P6. Scale bars are 25 µm.

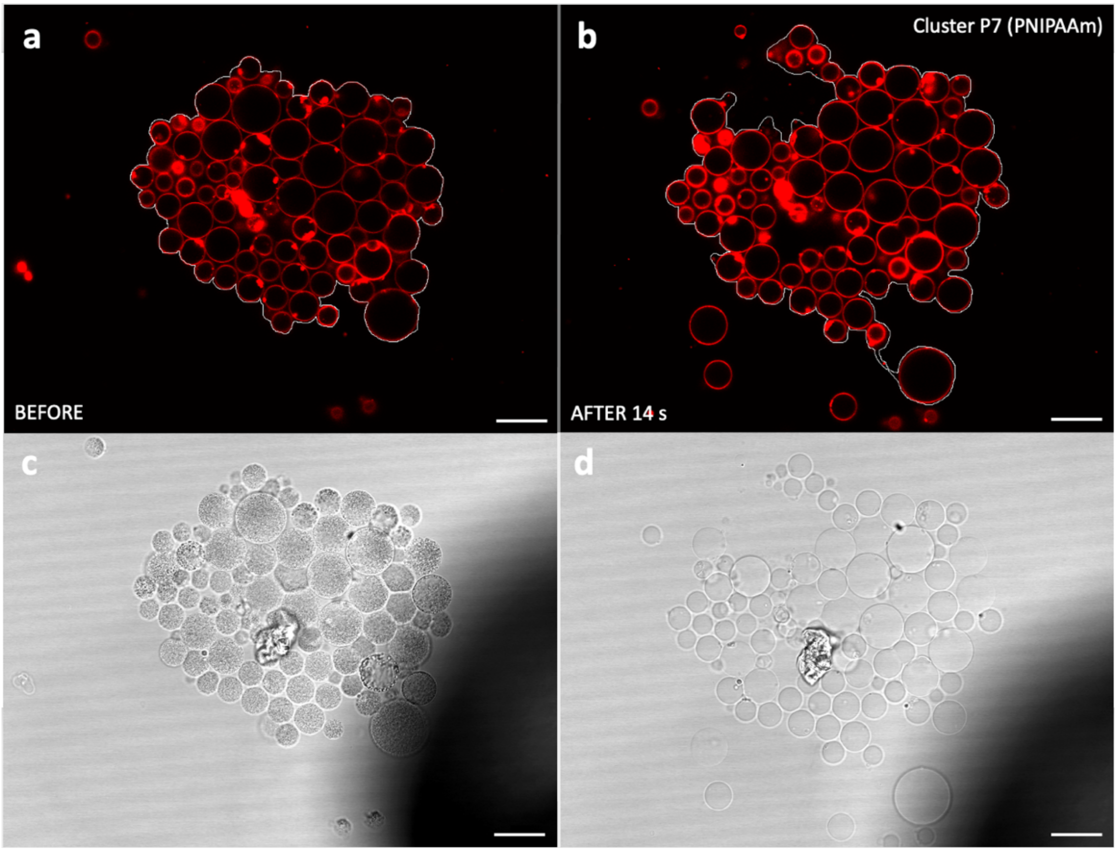

Figure 61: Disintegration of cluster P7. Scale bars are 25 µm.

The amount of expansion was quantified by measuring the area of the cluster right before and 14 s after the laser was turned off and calculating the increase in area as percentage of the initial cluster area. The results above regarding expansion of PNIPAAm containing vesicles, were compared to the control experiments which are presented and discussed in the following sections.

Control Experiments

The disintegration of the control-clusters which was measured the same way as for the PNIPAAm experiments, are shown in **Figure 62–65**.

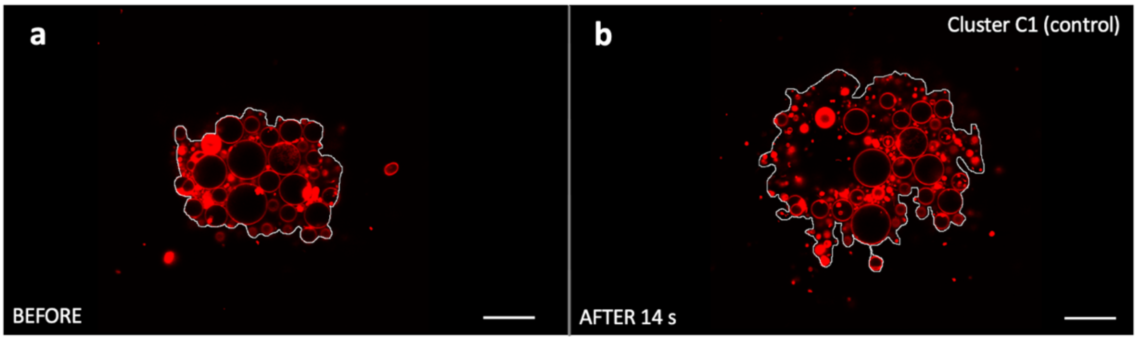

Figure 62: Disintegration of cluster C1. Scale bars are 25 µm.

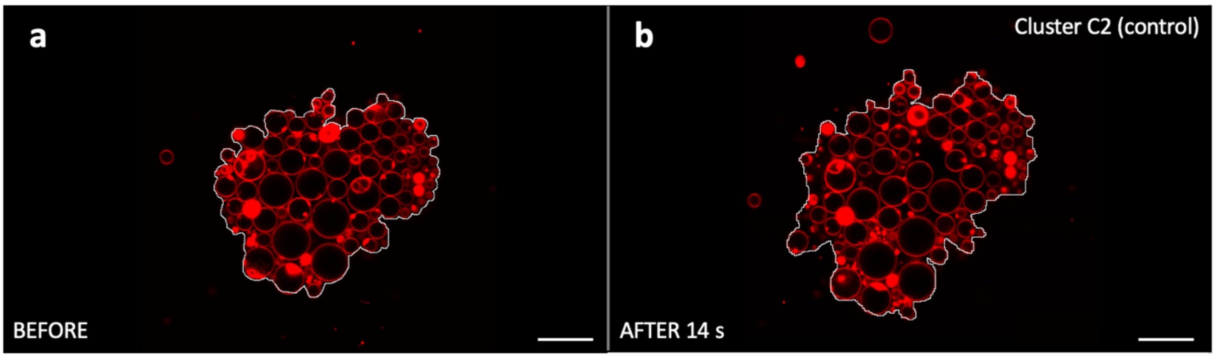

Figure 63: Disintegration of cluster C2. Scale bars are 25 μm.

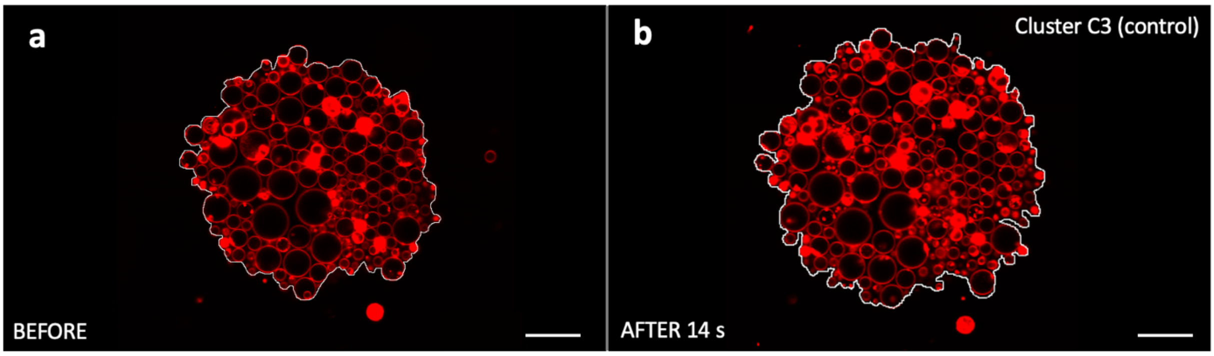

Figure 64: Disintegration of cluster C3. Scale bars are 25 μm.

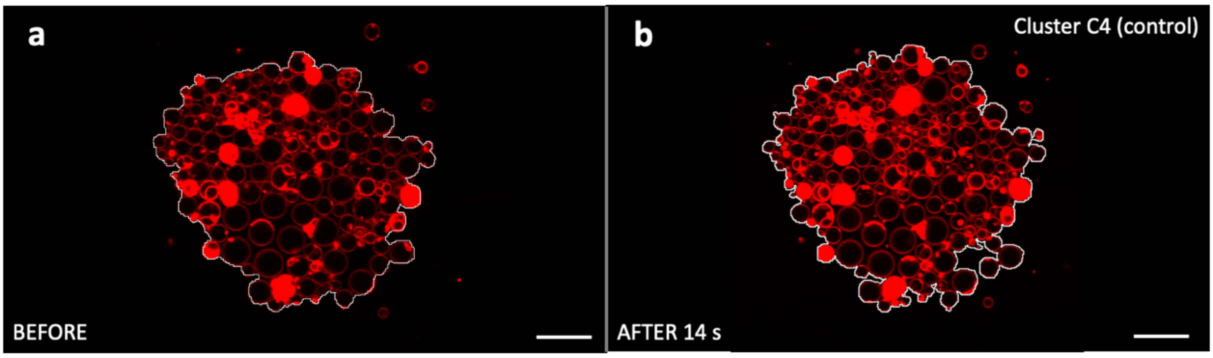

Figure 65: Disintegration of cluster C4. Scale bars are 25 μm.

* * *

The increase in area of each cluster, of both control and PNIPAAm-encapsulating vesicle clusters was plotted against the initial cluster area and is shown in the plot in **Figure 66**.

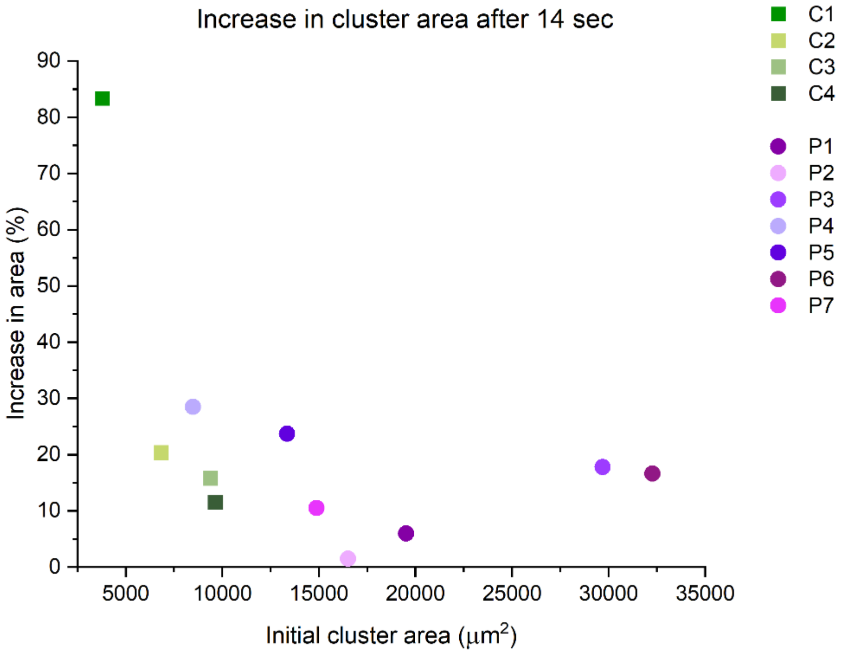

Figure 66: The expansion of the clusters 14 seconds after deactivation of the laser.

Based on the graph in **Figure 66**, within the set of control experiments, the smallest control cluster (C1) has the highest area increase (83,4 %) and the largest control cluster (C4) has the least area expansion (11,5 %). A possible explanation for this observation could be that when the clusters are large, they are composed a of high number of vesicles. This means more membrane surface area; hence more membrane material is in physical contact. It is established that heating causes an increase in membrane fluidity[17] and pore/defect formation[92]. In this case, membranes which are in physical contact would form intermembrane defects, for example hemifusion-like connections between the vesicles (**Figure 67a**).

The PNIPAAm-encapsulating vesicle clusters P1, P2 and P7, which all have a moderate cluster size, display very low expansion, with cluster P2 having the lowest increase in area of only 1,5 %. The increased integrity of these PNIPAAm-encapsulating vesicle clusters might be due to physical linkages between adjacent GUVs via PNIPAAm (**Figure 67b**). PNIPAAm has been reported to interact with lipid bilayer model membranes, in both physical-, e.g. through hydrophobic interactions and hydrogen bonds; and chemical gel form, e.g. as crosslinked polymer[93-95]. When PNIPAAm undergoes phase transition from expanded to collapsed state, it becomes more hydrophobic. The physical PNIPAAm gel (collapsed, T > LCST) encapsulated inside GUVs, can partially penetrate the membrane and become anchored to it[93]. Likewise, chemical PNIPAAm microgels in the ambient solution of GUVs, has been shown to assemble in the bilayer-bilayer contact area between adjacent GUVs, and partially penetrate into the hydrophobic core of the bilayer when heated above the LCST[95]. Hydrophobically modified PNIPAAm chains have displayed even greater interactions with lipid membranes. Copolymers of PNIPAAm and vinyl ferrocene internalized in GUVs, interact with the membrane, and exerts a pulling force that is strong enough to create deformations and pull nanotubes when transitioning to a physical gel[39]. In another study, PNIPAAm copolymerized with N-[2-(1-naphthyl)ethyl]-N-n-octadecylacrylamide or N-[4-(1-pyrenyl)butyl]-N-n- octadecylacrylamide was mixed with liposome suspensions, and was found to promote both membrane fission and fusion[96]. Although the exact nature of the PNIPAAm-membrane interactions is not completely understood, the findings from these studies imply that there could be a PNIPAAm-facilitated linkage between the GUVs in our clusters.

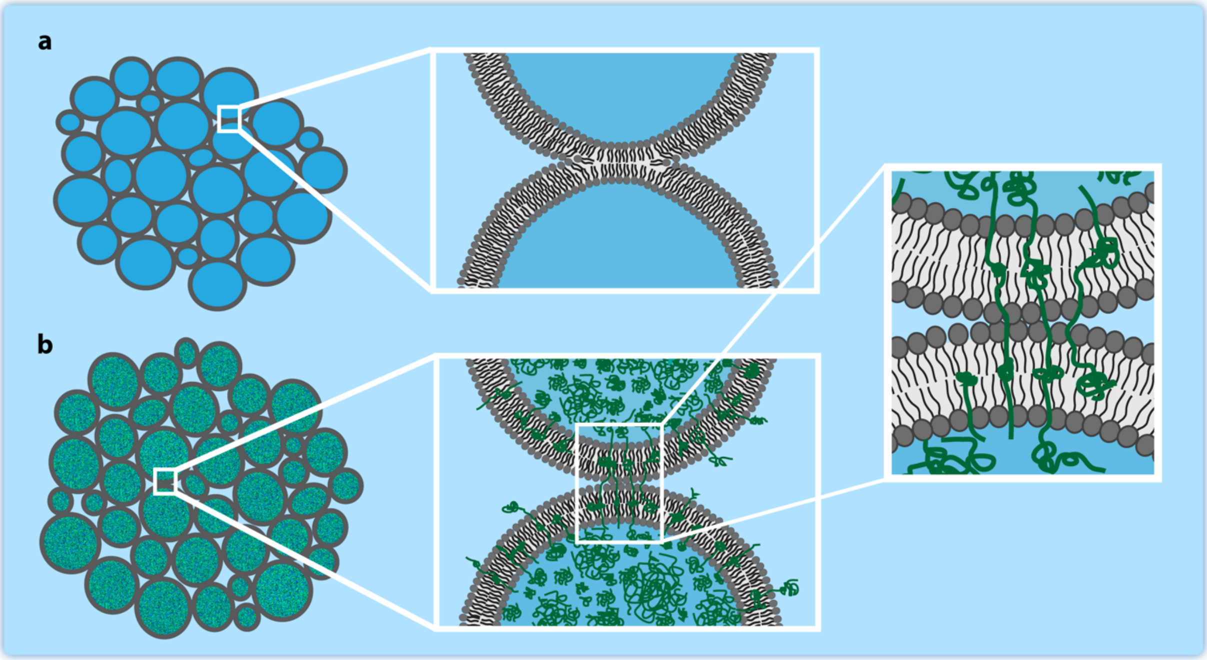

Figure 67: Possible mechanisms of clustering among lipid compartments. (a) Hemifusions between the vesicles may prolong cluster integrity. (b) PNIPAAm (represented in green) can penetrate the lipid bilayer upon gelation and might anchor adjacent vesicles.

We observe that the appearance, e.g. opacity, graininess of PNIPAAm inside the vesicles in the clusters during heating, vary. The majority of the vesicles have a homogenous graininess in their internal volume, e.g. those indicated with blue arrows in **Figure 68b**. In other vesicles (magenta arrows), the opacity is higher and there are grains with relatively larger size. In those vesicles, a ring-shaped aggregation along the vesicle membrane is observed, i.e. there appears to be a preferred interaction of the gel with the lipid membrane. Previous work indicates that the opacity of the internal volume of the GUVs is related to the concentration of polymer and the size of the microaggregates[39, 40, 97]. The concentration of PNIPAAm inside all the vesicles is the same and all clusters have been heated for the same amount of time. The different levels of phase separation of the polymer inside the vesicles are highly likely due the exact temperature a particular vesicle experiences at a specific position within the cone of acceptance of the locally heated region. The vesicles are dynamically moving inside the clusters which are themselves rotating. Since the amount of phase separation is different from GUV to GUV, the PNIPAAm-membrane interaction likely also differs among the GUVs composing a cluster.

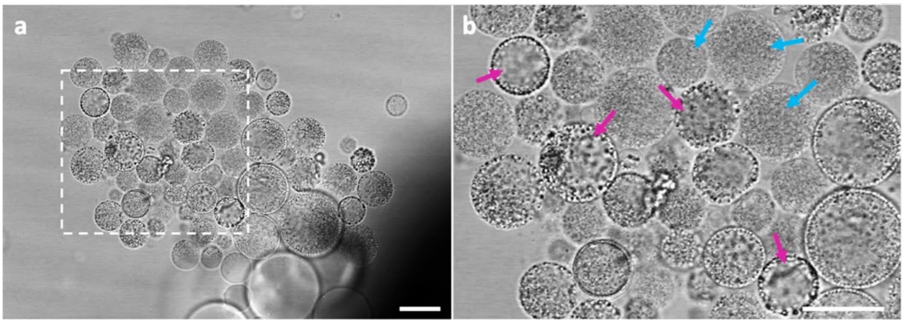

Figure 68: Phase separation of PNIPAAm inside the vesicles composing cluster P1. b) Blue arrows point to lower degree of phase separation, while magenta arrows point to vesicles with larger PNIPAAm microaggregates. Scale bars are 25 µm.

When comparing the micrographs of the cluster with the lowest expansion (P2) and the cluster with the highest expansion(P4) (**Figure 69a'**), we see that there is a difference in the size of the PNIPAAm-microaggregates. P2 appears to have larger aggregates, some along the vesicle membranes, whereas the vesicles in P4 have a more homogeneous distribution of the polymer in their internal volume (**Figure 69b'**).

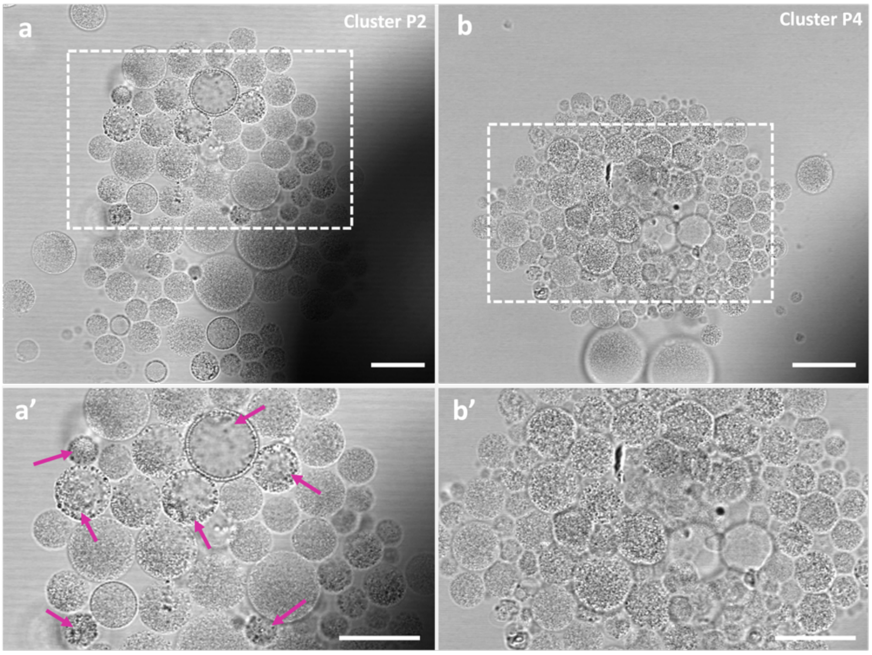

Figure 69: Microphase separation of PNIPAAm in cluster P2 (a) versus P4 (b). The areas within the dashed rectangles are enlarged and shown in (a') and (b'). Scale bars are 25 µm.

P3 and P6 are the largest clusters and are approximately twice the size of clusters P1 and P2. According to our hypothesis, if the PNIPAAm interconnect the vesicles in P3 and P6, these clusters are expected to stick together and expand minimally. One explanation for the deviant behavior can be that the large clusters are exposed to a broader temperature gradient, i.e. a more spread temperature range along the plane of the locally heated surface region. In this case, the vesicles at the edge of a large cluster would experience a lower temperature than the vesicles at the center of the heated circular region. Although PNIPAAm is in the collapsed state inside the vesicles, i.e. their temperature is above the LCST (**Figure 57c** and **Figure 60c**), slight temperature differences in the order of a few °C might result in different levels of interaction between the polymer and the membrane. We observe that P3 and P6 do not exhibit the very distinct polymer aggregation along the vesicle membrane, as for the vesicles in P1 and P2 (**Figure 68b** and **Figure 69a'**). Another aspect is the temperature the vesicular lipid membranes experience. Changes in temperature can increase fluidity and induce defect formation[92], as well as phase separations in phospholipid bilayer membranes[98]. This means that not only does the polymer phase transition during temperature changes, but also the lipid membranes change their behavior. Since the physical interaction between the polymer and the membrane would be influenced by properties of both components, it should be taken into account that the temperature gradient affects both.

3.2.4 Pulsed Heating

In order to confirm that the cluster formation was due to local heating we performed an experiment where we applied the heat to vesicles containing no PNIPAAm in consecutive pulses and observed the response of the vesicle agglomerates. After the clusters had formed, the heating was turned off and on by 20 second intervals. The change in cluster size during the heat pulses over time is shown in the plot in **Figure 70**.

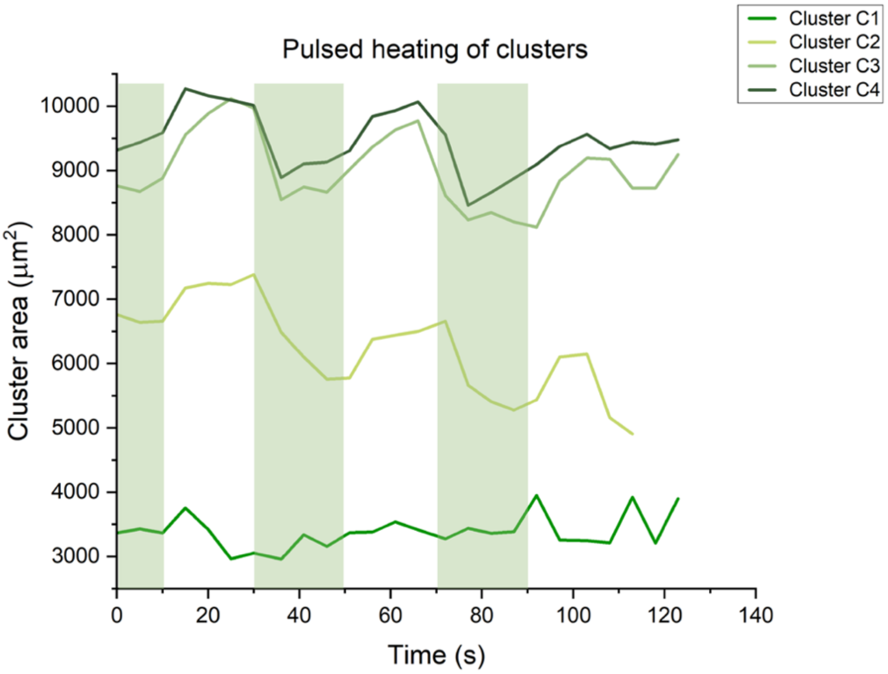

Figure 70: Pulsed heating of control clusters C1-C4. The green areas indicate the activated state of the laser (40 °C).

Cluster C2, C3 and C4 form during heating and expand when the heat is off. It is difficult to attribute the behavior of C1 to heating; this particular cluster appear to follow no special trend in terms of growth during heat-cool cycles. C1 is a relatively small cluster **Figure 62a**. During the heating cycles, the number of vesicles which adhere and detach from the cluster are too few to significantly contribute to the wave-like pattern observed in C2-4.

3.2.5 Cluster Migration

We explored the possibility to direct the migration of vesicle clusters by using the thermal trap. Cell migration plays an essential role in many physiological and pathological processes, such as embryonic growth, tissue development, wound healing and metastasis of cancer[99]. The physics and mechanics of cellular migration is poorly understood in cell biology[100] and employing artificial cells as models to investigate migration is of interest. Cells have the ability to detect and respond to various types of environmental cues, such as chemical gradients, electrical fields and temperature gradients[100, 101].

A cluster from PNIPAAm-encapsulating vesicles was formed, and the optical fiber-tip was moved along the xy-plane to check if the clusters can migrate following the temperature gradient. The results are presented in **Figure 71**.

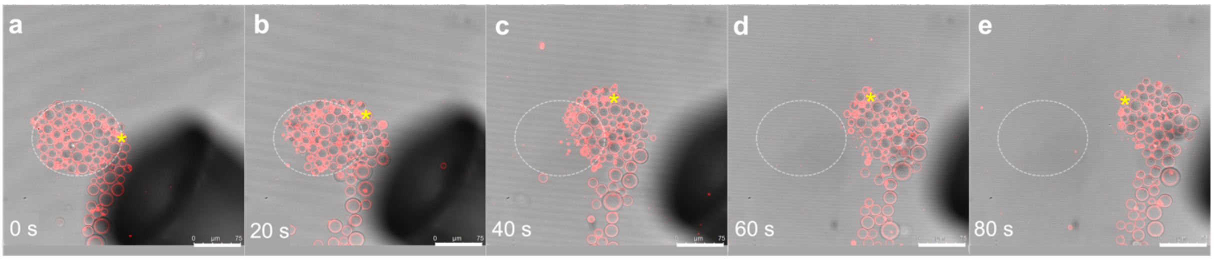

Figure 71: (a-e) Confocal micrographs showing migration of a cluster. A cluster containing PNIPAAm-encapsulating vesicles is migrating on the surface following the locally heated region. Fluorescence and bright field channels are overlaid. The tip of the laser optical fiber is visible in the bright field channel. The contour of the original cluster at its initial position is encircled within the white dashed line. The position of a specific vesicle in the cluster is marked with a yellow asterisk. Scale bar is 75 µm.

It was observed that the cluster migrated following the movement of the optical fiber tip. The cluster is clearly trapped in the heated spot following the heat gradient. While the cluster migrates, a stream of vesicles continues to approach and adhere to the dynamic cluster. It appears that the cluster is stable while moving and continues to rotate in a counterclockwise manner. In summary, the clusters are motile in response to the local heating; they move towards the region with higher temperature. The clusters can be used as a platform to study collective cell migration along a temperature gradient. Thermal migration, or thermotaxis, is observed in single human cells such as trophoblasts[102], sperm cells[101] and leukocytes[103], and also collectively in motile organisms such as bacteria (*E. coli*), amoeba (*D. discoideum*) and nematodes (*C. elegans*)[104].

3.3 Mechanism Behind Self-Organization of GUVs

A possible physical explanation for the clustering phenomenon is that the process is driven by thermal convection. Thermal convection is the transfer of heat by the movement of a fluid mass such as air or water[105]. A temperature gradient across the fluid induces a gradient in density and/or surface tension and moves it from high to low temperature. This leads to circulation of the fluid and the generation of convection[106]. Convection is as a form of self-organization of non-living matter, where the random motion of the molecules spontaneously becomes ordered, and results in non-equilibrium patterns[107].

This principle can be applied to our system of cylindrical imaging chambers filled with a thin layer of liquid, in which the GUVs are suspended. A schematic of the proposed mechanism behind the clustering phenomenon is illustrated in **Figure 72**.

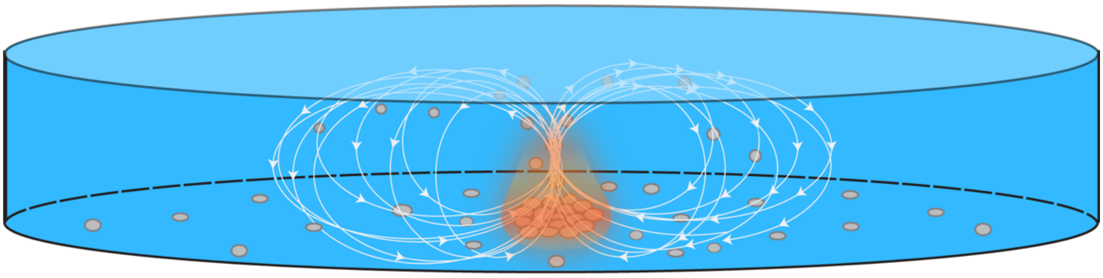

Figure 72: Laser-induced thermal convection currents might be driving the cluster formation.

The activation of the IR-laser induces a localized temperature gradient and convection flow similar to the schematic arrangement depicted in **Figure 72**. It is likely that a single convection cell is created around the vertical axis of the cone of acceptance of the laser beam. The GUVs follow the convection currents and are drawn towards the laser focus point. They get arrested in the "thermal trap" where they aggregate and form a cluster. We observed that occasionally some vesicles arrived at the focus point but moved upwards (in the z plane) and disappeared instead of joining the cluster. This supports the idea that the GUVs are following convection currents.

There are several types of convection: Rayleigh-Bénard (RB) convection, Bénard-Marangoni (BM) convection, and Rayleigh-Bénard-Marangoni (RBM) convection[108]. RB convection, also known as free convection, is driven by the imbalance between the buoyancy and viscous forces and can occur in a thin layer of fluid that is confined between two horizontal plates[105]. The fluid is heated from below and cooled from above. When the fluid is heated, it becomes less dense than the surrounding fluid, making it subject to an upward buoyant force that causes it to rise upwards. When this mass of liquid reaches the colder region, the density will increase, it becomes less buoyant and sinks. This leads to circulation of the fluid and the formation of convection currents[106]. RB convection is described by the dimensionless Rayleigh number (Ra), which is the ratio between the buoyancy forces and the viscous forces, and is given by

$$Ra = \frac{g\beta\Delta T d^3}{\nu\alpha} \tag{6}$$

where g is the gravitational acceleration, β the thermal expansion coefficient, ΔT the vertical temperature gradient, d the thickness of the fluid film, ν the kinematic viscosity and α the thermal diffusivity[107].

BM convection, also called thermocapillary convection, occurs in a thin layer of fluid where the upper surface is exposed to air. The temperature gradient induces a surface tension gradient that drives the convection: surface tension decreases with increasing temperature. When the surface tension forces are higher than the viscous forces, BM convection occurs. It is described by the dimensionless Marangoni number, which is the ratio between surface tension forces and viscous forces:

$$Ma = -\frac{\delta\sigma}{\delta T}\frac{\Delta T d}{\mu\alpha} \tag{7}$$

where σ is the surface tension which changes with the temperature T and μ the dynamic viscosity. RBM is a combination of both of these convection types and is driven by both density and surface tension gradients.

The exact mechanism behind why some of the GUVs get trapped at the focus point instead of just following the current upwards, is currently unknown. To determine which type of convection dominates in our system, and how much each type of flow contributes to the overall convection, the Rayleigh- and Marangoni numbers, and their ratio (Bond number) can be calculated as follow-up work. Studies on microparticles however, suggest that BM convection is the dominating mechanism at this scale. In a study by Vela et al.[109], convection-driven motion of micro-beads in liquid medium was induced by a focused IR-laser beam. Their experimental set-up involved spherical glass beads in the size range of 30 to 300 µm. The glass beads were suspended in water inside a Petri dish, placed on top of a microscope that directs an IR-laser beam (1480 nm) through the objective lens. The heat from the laser was absorbed through the Petri dish, generating thermocapillary convection flow that dragged the beads towards the laser focus. Although our experimental set-up and materials are slightly different, the dimensions of the fluid and the dispersed particles, i.e. vesicles, are comparable. This suggests that the thermally induced self-organization of GUVs is driven by BM convection.

4 Conclusion and Future Work

In this thesis, cDICE is used to efficiently encapsulate an aqueous solution of poly (N-isopropylacrylamide) (PNIPAAm) in artificial cell populations. In earlier work, microneedle-injection and electroformation was utilized to encapsulate PNIPAAm sol phase in single vesicles; this is the first time PNIPAAm is internalized in a large number of giant lipid vesicles (hundreds).

An IR-B laser-induced temperature gradient was locally applied to study the intra- and intercellular response of populations of artificial cells encapsulating PNIPAAm, a synthetic thermoresponsive polymer that undergoes reversible phase transition from sol to gel phase when heated above its lower critical solution temperature (LCST) at 32 ℃. The highly localized temperature gradient applied by means of the optical fiber-based IR-laser, induces convection flow in the aqueous media and the self-organization of GUVs both with and without PNIPAAm, into dynamic multicellular tissue-like structures. Upon termination of heating, PNIPAAm-encapsulating vesicle clusters exhibited a prolonged adhesion compared to the lipid compartments free of PNIPAAm. This observation can be explained by the specific interaction of PNIPAAm hydrogel with the lipid bilayer. PNIPAAm can partially penetrate into the hydrophobic core of the bilayer when heated above the LCST and might anchor adjacent GUVs together.

To the best of our knowledge, the generation of a bottom-up artificial multicellular structure, induced by thermal stimuli, has for the first time been described through this thesis work. The method has many potential applications and is a step towards engineering artificial tissue-like structures or proto-tissue. It can be used to study the emergence of multicellularity, and dynamic processes such as migration and intercellular communication. One potential area to explore is tissue engineering. The state-of-the-art applications of tissue formation out of soft matter compartments involve 3D droplet printing, where an aqueous solution is ejected into a lipid-in-oil solution, forming stable lipid monolayer-coated aqueous droplets. In this case, a single bilayer separates two adjacent compartments, while in our system, each artificial cell has a complete bilayer, thus the interface between adjacent cells is a double bilayer better approximating an actual biological tissue. In future work, clusters can be formed by diverse vesicle populations, encapsulating different chemical components, where their intercellular communication can be enabled through synthetic gap junctions, such as α-hemolysin. The thermal convection-based self-organization of vesicles offers a fast and efficient way of forming tissue-like structures.

References

1. Martino, C.; deMello, A. J., Droplet-based microfluidics for artificial cell generation: A brief review. *Interface Focus* **2016,** *6* (4).

2. Xu, C.; Hu, S.; Chen, X., Artificial cells: from basic science to applications. *Materials Today* **2016,** *19* (9), 516-532.

3. Chang, T. M. S., Hemoglobin corpuscles. **1957**.

4. Chang, T. M. S., ARTIFICIAL CELL evolves into nanomedicine, biotherapeutics, blood substitutes, drug delivery, enzyme/gene therapy, cancer therapy, cell/stem cell therapy, nanoparticles, liposomes, bioencapsulation, replicating synthetic cells, cell encapsulation/scaffold, biosorbent/immunosorbent haemoperfusion/plasmapheresis, regenerative medicine, encapsulated microbe, nanobiotechnology, nanotechnology. *Artificial Cells, Nanomedicine and Biotechnology* **2019,** *47* (1), 997-1013.

5. Schwille, P.; Spatz, J.; Landfester, K.; Bodenschatz, E.; Herminghaus, S.; Sourjik, V.; Erb, T. J.; Bastiaens, P.; Lipowsky, R.; Hyman, A.; Dabrock, P.; Baret, J. C.; Vidakovic-Koch, T.; Bieling, P.; Dimova, R.; Mutschler, H.; Robinson, T.; Tang, T. Y. D.; Wegner, S.; Sundmacher, K., MaxSynBio: Avenues Towards Creating Cells from the Bottom Up. *Angewandte Chemie - International Edition* **2018,** *57* (41), 13382-13392.

6. Kobayashi, K.; Ehrlich, S. D.; Albertini, A.; Amati, G.; Andersen, K. K.; Arnaud, M.; Asai, K.; Ashikaga, S.; Aymerich, S.; Bessieres, P.; Boland, F.; Brignell, S. C.; Bron, S.; Bunai, K.; Chapuis, J.; Christiansen, L. C.; Danchin, A.; Débarbouillé, M.; Dervyn, E.; Deuerling, E.; Devine, K.; Devine, S. K.; Dreesen, O.; Errington, J.; Fillinger, S.; Foster, S. J.; Fujita, Y.; Galizzi, A.; Gardan, R.; Eschevins, C.; Fukushima, T.; Haga, K.; Harwood, C. R.; Hecker, M.; Hosoya, D.; Hullo, M. F.; Kakeshita, H.; Karamata, D.; Kasahara, Y.; Kawamura, F.; Koga, K.; Koski, P.; Kuwana, R.; Imamura, D.; Ishimaru, M.; Ishikawa, S.; Ishio, I.; Coq, D. L.; Masson, A.; Mauël, C.; Meima, R.; Mellado, R. P.; Moir, A.; Moriya, S.; Nagakawa, E.; Nanamiya, H.; Nakai, S.; Nygaard, P.; Ogura, M.; Ohanan, T.; O'Reilly, M.; O'Rourke, M.; Pragai, Z.; Pooley, H. M.; Rapoport, G.; Rawlins, J. P.; Rivas, L. A.; Rivolta, C.; Sadaie, A.; Sadaie, Y.; Sarvas, M.; Sato, T.; Saxild, H. H.; Scanlan, E.; Schumann, W.; Seegers, J. F. M. L.; Sekiguchi, J.; Sekowska, A.; Séror, S. J.; Simon, M.; Stragier, P.; Studer, R.; Takamatsu, H.; Tanaka, T.; Takeuchi, M.; Thomaides, H. B.; Vagner, V.; Dijl, J. M. v.; Watabe, K.; Wipat, A.; Yamamoto, H.; Yamamoto, M.; Yamamoto, Y.; Yamane, K.; Yata, K.; Yoshida, K.; Yoshikawa, H.; Zuber, U.; Ogasawara, N., Essential <i>Bacillus</i> <i>subtilis</i> genes. *Proceedings of the National Academy of Sciences* **2003,** *100* (8), 4678-4683.

7. Hutchison, C. A.; Peterson, S. N.; Gill, S. R.; Cline, R. T.; White, O.; Fraser, C. M.; Smith, H. O.; Venter, J. C., Global Transposon Mutagenesis and a Minimal Mycoplasma Genome. *Science* **1999,** *286* (5447), 2165-2169.

8. Gil, R.; Silva, F. J.; Peretó, J.; Moya, A., Determination of the Core of a Minimal Bacterial Gene Set. *Microbiology and Molecular Biology Reviews* **2004,** *68* (3), 518-537.

9. Ji, Y.; Zhang, B.; Van, S. F.; Horn; Warren, P.; Woodnutt, G.; Burnham, M. K. R.; Rosenberg, M., Identification of Critical Staphylococcal Genes Using Conditional Phenotypes Generated by Antisense RNA. *Science* **2001,** *293* (5538), 2266-2269.

10. Wang, X.; Liu, X.; Huang, X., Bioinspired Protein-Based Assembling: Toward Advanced Life-Like Behaviors. *Advanced Materials* **2020,** *32* (25).

11. Loiseau, E.; Schneider Jochen, A. M.; Keber Felix, C.; Pelzl, C.; Massiera, G.; Salbreux, G.; Bausch Andreas, R., Shape remodeling and blebbing of active cytoskeletal vesicles. *Science Advances* **2016,** *2* (4), e1500465.

12. Robinson, T., Microfluidic Handling and Analysis of Giant Vesicles for Use as Artificial Cells: A Review. *Advanced Biosystems* **2019,** *3* (6).

13. Sharma, A. K.; Prasher, P.; Aljabali, A. A.; Mishra, V.; Gandhi, H.; Kumar, S.; Mutalik, S.; Chellappan, D. K.; Tambuwala, M. M.; Dua, K.; Kapoor, D. N., Emerging era of "somes": polymersomes as versatile drug delivery carrier for cancer diagnostics and therapy. *Drug Delivery and Translational Research* **2020,** *10* (5), 1171-1190.

14. Pawar, P. V.; Gohil, S. V.; Jain, J. P.; Kumar, N., Functionalized polymersomes for biomedical applications. *Polymer Chemistry* **2013,** *4* (11), 3160-3176.

15. Ivanov, I.; Castellanos, S. L.; Balasbas, S.; Otrin, L.; Marušič, N.; Vidaković-Koch, T.; Sundmacher, K., Bottom-Up Synthesis of Artificial Cells: Recent Highlights and Future Challenges. *Annual Review of Chemical and Biomolecular Engineering* **2021,** *12* (1), 287-308.

16. Gonzales, D. T.; Yandrapalli, N.; Robinson, T.; Zechner, C.; Tang, T. Y. D., Cell-Free Gene Expression Dynamics in Synthetic Cell Populations. *ACS Synthetic Biology* **2022,** *11* (1), 205-215.

17. Campbell, N. A. U., Lisa A.; Cain, Michael L.; Wasserman, Steven A.; Minorsky, Peter V.; Reece, Jane B., *Biology - A Global Approach*. 11 ed.; Pearson Education Limited: England, 2018.

18. Kubitschke, H.; Morawetz, E. W.; Käs, J. A.; Schnauß, J., Physical Properties of Single Cells and Collective Behavior. In *Quantification of Biophysical Parameters in Medical Imaging*, Sack, I.; Schaeffter, T., Eds. Springer International Publishing: Cham, 2018; pp 89-121.

19. Khain, E.; Katakowski, M.; Hopkins, S.; Szalad, A.; Zheng, X.; Jiang, F.; Chopp, M., Collective behavior of brain tumor cells: The role of hypoxia. *Physical Review E* **2011,** *83* (3), 031920.

20. Deisboeck, T. S.; Couzin, I. D., Collective behavior in cancer cell populations. *Bioessays* **2009,** *31* (2), 190-7.

21. van Ravensteijn, B. G. P.; Voets, I. K.; Kegel, W. K.; Eelkema, R., Out-of-Equilibrium Colloidal Assembly Driven by Chemical Reaction Networks. *Langmuir* **2020,** *36* (36), 10639-10656.

22. Toda, S.; Blauch Lucas, R.; Tang Sindy, K. Y.; Morsut, L.; Lim Wendell, A., Programming self-organizing multicellular structures with synthetic cell-cell signaling. *Science* **2018,** *361* (6398), 156-162.

23. Villar, G.; Graham Alexander, D.; Bayley, H., A Tissue-Like Printed Material. *Science* **2013,** *340* (6128), 48-52.

24. Wang, X.; Tian, L.; Du, H.; Li, M.; Mu, W.; Drinkwater, B. W.; Han, X.; Mann, S., Chemical communication in spatially organized protocell colonies and protocell/living cell micro-arrays. *Chemical Science* **2019,** *10* (41), 9446-9453.

25. Bolognesi, G.; Friddin, M. S.; Salehi-Reyhani, A.; Barlow, N. E.; Brooks, N. J.; Ces, O.; Elani, Y., Sculpting and fusing biomimetic vesicle networks using optical tweezers. *Nature Communications* **2018,** *9* (1), 1882.

26. Alberts, B. J., Alexander; Lewis, Julian; Morgan, David; Raff, Martin; Roberts, Keith; Walter, Peter, *Molecular Biology of The Cell*. 6 ed.; Garland Science, Taylor & Francis Group: 2015.

27. Zhu, Y.; Guo, X.; Liu, J.; Li, F.; Yang, D., Emerging Advances of Cell-Free Systems toward Artificial Cells. *Small Methods* **2020,** *4* (10).

28. Lee, K.-H.; Kim, D.-M., Recent advances in development of cell-free protein synthesis systems for fast and efficient production of recombinant proteins. *FEMS Microbiology Letters* **2018,** *365* (17).

29. Klumpp, S.; Faivre, D., Magnetotactic bacteria: Magnetic navigation on the microscale. *European Physical Journal: Special Topics* **2016,** *225* (11-12), 2173-2188.
30. Li, Q.; Li, S.; Zhang, X.; Xu, W.; Han, X., Programmed magnetic manipulation of vesicles into spatially coded prototissue architectures arrays. *Nature Communications* **2020,** *11* (1), 232.
31. Hu, X.; Zhang, Y.; Xie, Z.; Jing, X.; Bellotti, A.; Gu, Z., Stimuli-Responsive Polymersomes for Biomedical Applications. *Biomacromolecules* **2017,** *18* (3), 649-673.
32. Liu, F.; Kozlovskaya, V.; Medipelli, S.; Xue, B.; Ahmad, F.; Saeed, M.; Cropek, D.; Kharlampieva, E., Temperature-Sensitive Polymersomes for Controlled Delivery of Anticancer Drugs. *Chemistry of Materials* **2015,** *27* (23), 7945-7956.
33. Zhang, L.; Zhang, D.; Yang, Y.; Zhang, Y., Stimuli-Responsive Proteinosomes Based on Biohybrid Shell Cross-Linked Micelles. *Langmuir* **2021,** *37* (13), 3950-3959.
34. Gobbo, P.; Patil, A. J.; Li, M.; Harniman, R.; Briscoe, W. H.; Mann, S., Programmed assembly of synthetic protocells into thermoresponsive prototissues. *Nature Materials* **2018,** *17* (12), 1145-1153.
35. Rideau, E.; Dimova, R.; Schwille, P.; Wurm, F. R.; Landfester, K., Liposomes and polymersomes: a comparative review towards cell mimicking. *Chemical Society Reviews* **2018,** *47* (23), 8572-8610.
36. Lentini, R.; Yeh Martín, N.; Mansy, S. S., Communicating artificial cells. *Current Opinion in Chemical Biology* **2016,** *34*, 53-61.
37. Miesfeld, R. L.; McEvoy, M. M., *Biochemistry*. 2016.
38. Ole G. Mouritsen, L. A. B., *LIFE - AS A MATTER OF FAT*. 2 ed.; Springer Cham: 2016.
39. Węgrzyn, I.; Jeffries, G. D. M.; Nagel, B.; Katterle, M.; Gerrard, S. R.; Brown, T.; Orwar, O.; Jesorka, A., Membrane Protrusion Coarsening and Nanotubulation within Giant Unilamellar Vesicles. *Journal of the American Chemical Society* **2011,** *133* (45), 18046-18049.
40. Campillo, C.; Pépin-Donat, B.; Viallat, A., Responsive viscoelastic giant lipid vesicles filled with a poly(N-isopropylacrylamide) artificial cytoskeleton. *Soft Matter* **2007,** *3* (11), 1421-1427.
41. Reeves, J. P.; Dowben, R. M., Formation and properties of thin-walled phospholipid vesicles. *J Cell Physiol* **1969,** *73* (1), 49-60.
42. Gözen, I.; Köksal, E. S.; Põldsalu, I.; Xue, L.; Spustova, K.; Pedrueza-Villalmanzo, E.; Ryskulov, R.; Meng, F.; Jesorka, A., Protocells: Milestones and Recent Advances. *Small* **2022**.
43. Angelova, M. I.; Dimitrov, D. S., Liposome electroformation. *Faraday Discussions of the Chemical Society* **1986,** *81* (0), 303-311.
44. Méléard, P.; Bagatolli, L. A.; Pott, T., Chapter 9 - Giant Unilamellar Vesicle Electroformation: From Lipid Mixtures to Native Membranes Under Physiological Conditions. In *Methods in Enzymology*, Academic Press: 2009; Vol. 465, pp 161-176.
45. Patil, Y. P.; Jadhav, S., Novel methods for liposome preparation. *Chemistry and Physics of Lipids* **2014,** *177*, 8-18.
46. Blosser, M. C.; Horst, B. G.; Keller, S. L., cDICE method produces giant lipid vesicles under physiological conditions of charged lipids and ionic solutions. *Soft Matter* **2016,** *12* (35), 7364-7371.
47. Litschel, T.; Schwille, P., Protein Reconstitution Inside Giant Unilamellar Vesicles. In *Annual Review of Biophysics*, 2021; Vol. 50, pp 525-548.
48. Deshpande, S.; Caspi, Y.; Meijering, A. E. C.; Dekker, C., Octanol-assisted liposome assembly on chip. *Nature Communications* **2016,** *7* (1), 10447.

49. Stachowiak Jeanne, C.; Richmond David, L.; Li Thomas, H.; Liu Allen, P.; Parekh Sapun, H.; Fletcher Daniel, A., Unilamellar vesicle formation and encapsulation by microfluidic jetting. *Proceedings of the National Academy of Sciences* **2008,** *105* (12), 4697-4702.
50. Abkarian, M.; Loiseau, E.; Massiera, G., Continuous droplet interface crossing encapsulation (cDICE) for high throughput monodisperse vesicle design. *Soft Matter* **2011,** *7* (10), 4610-4614.
51. Van de Cauter, L.; Fanalista, F.; van Buren, L.; De Franceschi, N.; Godino, E.; Bouw, S.; Danelon, C.; Dekker, C.; Koenderink, G. H.; Ganzinger, K. A., Optimized cDICE for Efficient Reconstitution of Biological Systems in Giant Unilamellar Vesicles. *ACS Synthetic Biology* **2021,** *10* (7), 1690-1702.
52. Abkarian, M.; Loiseau, E.; Massiera, G., Continuous droplet interface crossing encapsulation (cDICE) for high throughput monodisperse vesicle design. *Soft Matter* **2011,** *7* (10), 4610.
53. contributors, O. Droplet Microfluidics: T-Junction - Lina Wu. https://openwetware.org/mediawiki/index.php?title=Droplet_Microfluidics:_T-Junction_-_Lina_Wu&oldid=1042804 (accessed 23 April).
54. Claudet, C.; In, M.; Massiera, G., Method to disperse lipids as aggregates in oil for bilayers production. *Eur Phys J E Soft Matter* **2016,** *39* (1), 9.
55. van Swaay, D.; deMello, A., Microfluidic methods for forming liposomes. *Lab on a Chip* **2013,** *13* (5), 752-767.
56. Heskins, M.; Guillet, J. E., Solution Properties of Poly(N-isopropylacrylamide). *Journal of Macromolecular Science: Part A - Chemistry* **1968,** *2* (8), 1441-1455.
57. Lanzalaco, S.; Armelin, E., Poly(N-isopropylacrylamide) and Copolymers: A Review on Recent Progresses in Biomedical Applications. *Gels* **2017,** *3* (4), 36.
58. Cook, M. T.; Haddow, P.; Kirton, S. B.; McAuley, W. J., Polymers Exhibiting Lower Critical Solution Temperatures as a Route to Thermoreversible Gelators for Healthcare. *Advanced Functional Materials* **2021,** *31* (8).
59. Hench, L. L.; West, J. K., The sol-gel process. *Chemical Reviews* **1990,** *90* (1), 33-72.
60. Hoffman, A. S., Hydrogels for biomedical applications. *Advanced Drug Delivery Reviews* **2012,** *64*, 18-23.
61. Haq, M. A.; Su, Y.; Wang, D., Mechanical properties of PNIPAM based hydrogels: A review. *Materials Science and Engineering: C* **2017,** *70*, 842-855.
62. Yin, X.; Stöver, H. D. H., Hydrogel microspheres by thermally induced coacervation of poly(N,N-dimethylacrylamide-co-glycidyl methacrylate) aqueous solutions. *Macromolecules* **2003,** *36* (26), 9817-9822.
63. Wu, T. Y.; Zrimsek, A. B.; Bykov, S. V.; Jakubek, R. S.; Asher, S. A., Hydrophobic Collapse Initiates the Poly(N-isopropylacrylamide) Volume Phase Transition Reaction Coordinate. *J Phys Chem B* **2018,** *122* (11), 3008-3014.
64. Huang, X.; Li, M.; Green, D. C.; Williams, D. S.; Patil, A. J.; Mann, S., Interfacial assembly of protein-polymer nano-conjugates into stimulus-responsive biomimetic protocells. *Nature Communications* **2013,** *4*.
65. Ugrinic, M.; Zambrano, A.; Berger, S.; Mann, S.; Tang, T. Y. D.; Demello, A., Microfluidic formation of proteinosomes. *Chemical Communications* **2018,** *54* (3), 287-290.
66. Saleem, Q.; Liu, B.; Gradinaru, C. C.; Macdonald, P. M., Lipogels: Single-Lipid-Bilayer-Enclosed Hydrogel Spheres. *Biomacromolecules* **2011,** *12* (6), 2364-2374.
67. Dou, Y.; Li, J.; Yuan, B.; Yang, K., Lipid merging, protrusion and vesicle release triggered by shrinking/swelling of poly(N-isopropylacrylamide) microgel particles. *Applied Surface Science* **2014,** *296*, 95-99.

68. Kiser, P. F.; Wilson, G.; Needham, D., A synthetic mimic of the secretory granule for drug delivery. *Nature* **1998,** *394* (6692), 459-462.
69. Kazakov, S.; Kaholek, M.; Teraoka, I.; Levon, K., UV-induced gelation on nanometer scale using liposome reactor. *Macromolecules* **2002,** *35* (5), 1911-1920.
70. Ellis, R. J., Macromolecular crowding: obvious but underappreciated. *Trends in Biochemical Sciences* **2001,** *26* (10), 597-604.
71. Dix, J. A.; Verkman, A. S., Crowding Effects on Diffusion in Solutions and Cells. *Annual Review of Biophysics* **2008,** *37* (1), 247-263.
72. Sing, C. E., Micro- To macro-phase separation transition in sequence-defined coacervates. *Journal of Chemical Physics* **2020,** *152* (2).
73. Rumyantsev, A. M.; Jackson, N. E.; De Pablo, J. J., Polyelectrolyte Complex Coacervates: Recent Developments and New Frontiers. *Annual Review of Condensed Matter Physics* **2021,** *12*, 155-176.
74. Booth, R.; Qiao, Y.; Li, M.; Mann, S., Spatial Positioning and Chemical Coupling in Coacervate-in-Proteinosome Protocells. *Angewandte Chemie - International Edition* **2019,** *58* (27), 9120-9124.
75. Deng, N. N.; Huck, W. T. S., Microfluidic Formation of Monodisperse Coacervate Organelles in Liposomes. *Angewandte Chemie - International Edition* **2017,** *56* (33), 9736-9740.
76. Deshpande, S.; Brandenburg, F.; Lau, A.; Last, M. G. F.; Spoelstra, W. K.; Reese, L.; Wunnava, S.; Dogterom, M.; Dekker, C., Spatiotemporal control of coacervate formation within liposomes. *Nature Communications* **2019,** *10* (1), 1800.
77. Crowe, C. D.; Keating, C. D., Liquid-liquid phase separation in artificial cells. *Interface Focus* **2018,** *8* (5), 20180032.
78. Litschel, T.; Kelley, C. F.; Holz, D.; Adeli Koudehi, M.; Vogel, S. K.; Burbaum, L.; Mizuno, N.; Vavylonis, D.; Schwille, P., Reconstitution of contractile actomyosin rings in vesicles. *Nature Communications* **2021,** *12* (1), 2254.
79. Brushless DC Motor Speed Control System. https://catalog.orientalmotor.com/item/bmu-series-brushless-dc-motor-speed-control/shop-bmu-series-brushless-dc-motors/blm230hp-as-bmud30-c2.
80. Thermo Scientific General Gas Chromatography Tubing and Tools. https://www.fishersci.no/shop/products/general-gas-chromatography-shortix-capillary-column-cutter/10200545.
81. Oesterle, A., Pipette Cookbook 2018. Sutter Instrument: 2018. https://www.sutter.com/MICROPIPETTE/cookbook.html.
82. Microfluidic reservoir adapter. https://darwin-microfluidics.com/collections/microfluidic-reservoirs/products/1-5-ml-eppendorf-microfluidic-reservoir-xs.
83. Infrared radiation. https://www.icnirp.org/en/frequencies/infrared/index.html.
84. Encyclopaedia, T. E. o. Thermal radiation. https://www.britannica.com/science/thermal-radiation.
85. Spustova, K.; Xue, L.; Ryskulov, R.; Jesorka, A.; Gözen, I., Manipulation of Lipid Membranes with Thermal Stimuli. In *Membrane Lipids: Methods and Protocols*, Cranfield, C. G., Ed. Springer US: New York, NY, 2022; pp 209-225.
86. Digital Video Microscope Objective Setups. https://www.edmundoptics.eu/knowledge-center/application-notes/microscopy/digital-video-microscope-objective-setups.
87. Infinity-corrected Optical System. https://www.olympus-ims.com/en/microscope/terms/feature15/.

88. Colding-Christensen, C. S. Fluorescence Microscopy – the Magic of Fluorophores and Filters. https://bitesizebio.com/33529/fluorescence-microscopy-the-magic-of-fluorophores-and-filters/.

89. Lichtman, J. W.; Conchello, J.-A., Fluorescence microscopy. *Nature Methods* **2005,** *2* (12), 910-919.

90. Fellers, T. J. D., Michael W. Introduction to Confocal Microscopy. http://www.olympusconfocal.com/theory/confocalintro.html.

91. Miniewicz, A.; Bartkiewicz, S.; Orlikowska, H.; Dradrach, K., Marangoni effect visualized in two-dimensions Optical tweezers for gas bubbles. *Scientific Reports* **2016,** *6*, 34787.

92. Spustova, K.; Köksal, E. S.; Ainla, A.; Gözen, I., Subcompartmentalization and Pseudo-Division of Model Protocells. *Small* **2021,** *17* (2).

93. Konkoli, Z.; Wegrzyn, I.; Jesorka, A., Forces on an attractive surface generated from a thermoresponsive polymer gel. *AIP Advances* **2014,** *4* (8), 087137.

94. Ormategui, N.; Zhang, S.; Loinaz, I.; Brydson, R.; Nelson, A.; Vakurov, A., Interaction of poly(N-isopropylacrylamide) (pNIPAM) based nanoparticles and their linear polymer precursor with phospholipid membrane models. *Bioelectrochemistry* **2012,** *87*, 211-219.

95. Mihut, A. M.; Dabkowska, A. P.; Crassous, J. J.; Schurtenberger, P.; Nylander, T., Tunable Adsorption of Soft Colloids on Model Biomembranes. *ACS Nano* **2013,** *7* (12), 10752-10763.

96. Polozova, A.; Winnik, F. M., Mechanism of the interaction of hydrophobically-modified poly-(N-isopropylacrylamides) with liposomes. *Biochimica et Biophysica Acta (BBA) - Biomembranes* **1997,** *1326* (2), 213-224.

97. Jesorka, A.; Markström, M.; Orwar, O., Controlling the Internal Structure of Giant Unilamellar Vesicles by Means of Reversible Temperature Dependent Sol−Gel Transition of Internalized Poly(N-isopropyl acrylamide). *Langmuir* **2005,** *21* (4), 1230-1237.

98. Jacobson, K.; Papahadjopoulos, D., Phase transitions and phase separations in phospholipid membranes induced by changes in temperature, pH, and concentration of bivalent cations. *Biochemistry* **1975,** *14* (1), 152-161.

99. Trepat, X.; Chen, Z.; Jacobson, K., Cell migration. *Comprehensive Physiology* **2012,** *2* (4), 2369-2392.

100. SenGupta, S.; Parent, C. A.; Bear, J. E., The principles of directed cell migration. *Nature Reviews Molecular Cell Biology* **2021,** *22* (8), 529-547.

101. Bahat, A.; Eisenbach, M., Sperm thermotaxis. *Molecular and Cellular Endocrinology* **2006,** *252* (1), 115-119.

102. Higazi, A. A. R.; Kniss, D.; Manuppello, J.; Barnathan, E. S.; Cines, D. B., Thermotaxis of human trophoblastic cells. *Placenta* **1996,** *17* (8), 683-687.

103. Kessler, J. O.; Jarvik, L. F.; Fu, T. K.; Matsuyama, S. S., Thermotaxis, chemotaxis and age. *AGE* **1979,** *2* (1), 5-11.

104. Sourjik, V.; Wingreen, N. S., Turning to the cold. *Nature Cell Biology* **2007,** *9* (9), 1029-1031.

105. Zeytounian, R., *Convection in Fluids: A Rational Analysis and Asymptotic Modelling*. 2009; Vol. 90.

106. Maroto, J. A.; Pérez-Muñuzuri, V.; Romero-Cano, M. S., Introductory analysis of Bénard–Marangoni convection. *European Journal of Physics* **2007,** *28* (2), 311-320.

107. Chatterjee, A.; Mears, N.; Yadati, Y.; Iannacchione, G. S., An Overview of Emergent Order in Far-from-Equilibrium Driven Systems: From Kuramoto Oscillators to Rayleigh–Bénard Convection. *Entropy* **2020,** *22* (5), 561.

108. Es Sakhy, R.; El Omari, K.; Le Guer, Y.; Blancher, S., Rayleigh–Bénard–Marangoni convection in an open cylindrical container heated by a non-uniform flux. *International Journal of Thermal Sciences* **2014,** *86*, 198-209.
109. Vela, E.; Hafez, M.; Régnier, S., Laser-Induced Thermocapillary Convection for Mesoscale Manipulation. *International Journal of Optomechatronics* **2009,** *3* (4), 289-302.
110. Venczel, M.; Bognár, G.; Veress, Á., Temperature-Dependent Viscosity Model for Silicone Oil and Its Application in Viscous Dampers. *Processes* **2021,** *9* (2), 331.
111. Toor, A.; Lamb, S.; Helms, B. A.; Russell, T. P., Reconfigurable Microfluidic Droplets Stabilized by Nanoparticle Surfactants. *ACS Nano* **2018,** *12* (3), 2365-2372.

Appendix

Calculation of The Capillary Number

The capillary number is

$$Ca = \frac{\mu V}{\sigma} \qquad (8)$$

The relation between dynamic- and kinetic viscosity is

$$\mu = \nu \cdot \rho \qquad (9)$$

As 80% of the LOS is silicone oil, we use the physical parameters of silicone oil to estimate the capillary number. The silicone oil used for the experiments has $\nu = 5cSt$ at 25 °C. This is equal to $\nu = 5 \cdot 10^{-3}\ m^2 s^{-1}$. The density of silicone oil is 970 kgm^{-3}at 25 °C[110]. This gives

$$\mu_{silicone\ oil} = 5 \cdot 10^{-3}\ m^2 s^{-1} \cdot 970\ kgm^{-3}$$

$$\mu_{silicone\ oil} = 4.85 \cdot 10^{-3}\ Pa\ s$$

The distance from the rotation axis to the capillary tip is r_0. The velocity, V, is the linear velocity of the LOS at the capillary tip, and is related to the angular velocity by

$$V = r_0 \cdot \omega \qquad (10)$$

The rotation speed of $1500\ rpm$, is converted to rad/s:

$$\omega = 1500 \cdot \frac{\pi}{30}\ rad\ s^{-1}$$

$$\omega = 50\pi\ rad\ s^{-1}$$

Given $r_0 = 10.5\ mm$, the linear velocity is

$$V = 10.5 \cdot 10^{-3}\ m \cdot 50\pi\ rad\ s^{-1}$$

$$V = \frac{21}{40}\pi\ ms^{-1} = 1.65\ ms^{-1}$$

We use the physical properties of water to estimate the IAS/LOS interfacial tension. The interfacial tension between water and silicone oil is 25 mN/m[111]. When inserted into Eq. 8 along with the other calculated values, we get

$$Ca = \frac{4.85 \cdot 10^{-3}\ Pa\ s \cdot \frac{21}{40}\pi\ ms^{-1}}{25 \cdot 10^{-3}\ Nm^{-1}}$$

$$\boldsymbol{Ca = 0.32}$$

Calculation of The Droplet Flight Time

The droplet flight time is defined as

$$\tau_F = \frac{9\mu}{(2\Delta\rho R^2\omega^2)\ln\left(\frac{1+e}{r_0}\right)} \tag{11}$$

The difference in density between water and silicone oil is

$$\Delta\rho = \rho_{water} - \rho_{silicone\ oil}$$

$$\Delta\rho = 997\ kgm^{-3} - 970\ kgm^{-3}$$

$$\Delta\rho = 27\ kgm^{-3}$$

The distance the droplet has to travel through the LOS is $e = 6.5\ mm$. For a droplet with radius $R = 7.5\ \mu m$, and a chamber spinning at 1500 rpm, the droplet flight time is

$$\tau_F = \frac{9 \cdot 4.85 \cdot 10^{-3}\ Pa\ s}{(2 \cdot 27\ kgm^{-3} \cdot (7.5 \cdot 10^{-6}\ m)^2 \cdot (50\pi\ rad\ s^{-1})^2 \ln\left(\frac{1 + 6.5 \cdot 10^{-3}\ m}{10.5 \cdot 10^{-3}\ m}\right)}$$

$$\boldsymbol{\tau_F = 128\ s}$$

Parts for the Experimental Set-Op for cDICE

Product name	Product code	Producer/Vendor
Barbed to Male Luer Adapter for Soft-walled Tubing (1/16" ID)	CIL-P-850	Darwin Microfluidics
Borosilicate glass micropipettes (ID 0.78 mm, OD 1.0 mm, length 10 cm)	BF100-78-10	Sutter Instrument
Brushless DC motor with driver	BLM230HP-AS/ BMUD30-C2	Oriental Motor USA Corp
Circular glass slides, Ø 40 mm, 1 mm thick	71861	Electron Microscopy Sciences
Dino-Lite microscope stand	RK-06A/ IDCPRK-06A	Dino-Lite/VWR
Dino-Lite microscope stand, Extension pole	RK-06-PL/ IDCPRK-06-PL	Dino-Lite/VWR
Dino-Lite microscope stand, XY POSITIONING ARM	RK-10-PX/ IDCPRK-10-PX	Dino-Lite/VWR
Fused silica tubing, FSS Standard Polyimide Coating (ID 25 µm, OD 370 µm	Z-FSS-025370/ 888-581594	Postnova/ Norlab OY
Hypodermic needles, HENKE-JECT®, 14G x 3"	HSWA8300021961	VWR
Hypodermic needles, HENKE-JECT®, 18G x 2"	613-2030	VWR

Hypodermic needles, HENKE-JECT®, HENKE-JECT, 22 G x 2"	613-3117	VWR
Microfluidic Fittings 1/4"-28 Kit to 1/16" OD & 3/32" ID	LVF-KFI-06	Darwin Microfluidics
Microfluidic reservoir adapter for Eppendorf tubes	LVF-KPT-XS-2_2	Elveflow/ Darwin Microfluidics
Petri dish, Ø 35, H 10 mm	82.1135.500	Sarstedt
Plug-in reducer (Applicable tube: 3,2 mm OD, Applicable fitting: 4 mm OD)	KQ2R23-04A	SMC Automation
Polymeric tubing cutter		Teknolab
PTFE Tubing 1/16" OD for Microfluidics ((ID 1.0 mm)	BL-PTFE-1610-20	Darwin Microfluidics
PTFE Tubing (20 m, OD 3.2 mm, ID 2.4 mm)	LVF-KTU-11	Darwin Microfluidics
Shortix™ tubing cutter	21386-U	Shortix™/ Sigma Aldrich
Tubing, PEEK, Striped Color-Coded (orange), 1/32" OD x 0.05mm ID, 3m	B.211630-3	Teknolab

Components for Digital Microscope

Product name	Product code	Producer/Vendor
FLIR Flea®3 FL3-U3-13E4M-C 1/1.8" Monochrome USB 3.0 Camera	87-431	FLIR/ Edmund Optics
Mitutoyo to C-mount Camera 152.5 mm Extension Tube	56-992	Edmund Optics
MT-4 Accessory Tube Lens	54-428	Edmund Optics
5x Mitutoyo Plan Apo Infinity Corrected Long WD Objective	46-143	Mitutoyo/ Edmund Optics
Standard Boom Stand	54-120	Edmund Optics
Standard Fixed 1/4-20 Mounting Plate	54-122	Edmund Optics

Chemicals and Other Materials

Product name	Product code	Producer/Vendor
Acetone	1.00012.2500	Sigma-Aldrich
Chloroform	288306	Sigma-Aldrich
D-(+)-Glucose	G5767	Sigma-Aldrich
Decane	30540	Sigma-Aldrich
Egg PC, powder form	840051P	Avanti Polar Lipids/ Sigma-Aldrich

16:0 Liss Rhod PE	810158C	Avanti Polar Lipids/ Sigma-Aldrich
Methanol	20847.320	VWR
Mineral oil	M3516	Sigma-Aldrich
OptiPrep™ Density Gradient Medium	D1556	Sigma-Aldrich
16:0-18:1 PC, (POPC) chloroform	850457C	Avanti Polar Lipids/ Sigma-Aldrich
PDMS kit, Slygard™ 184, silicone elastomer base and -curing agent	24236-10	Electron Microscopy Sciences
Poly(N-isopropylacrylamide), PNIPAAm, Mn = 30.000	806471	Sigma-Aldrich
Silicone oil, viscosity 5 cSt (25 °C)	317667	Sigma-Aldrich
Sucrose	84100	Sigma-Aldrich
SU-8 Developer	Y020100 4000L1PE	MicroChem
WillCo-dish®KIT – Glass Bottom Dish. Size: 50 x 7 mm	KIT-5040 #1.5	WillCo Wells

Technical Drawings of Spinning Device

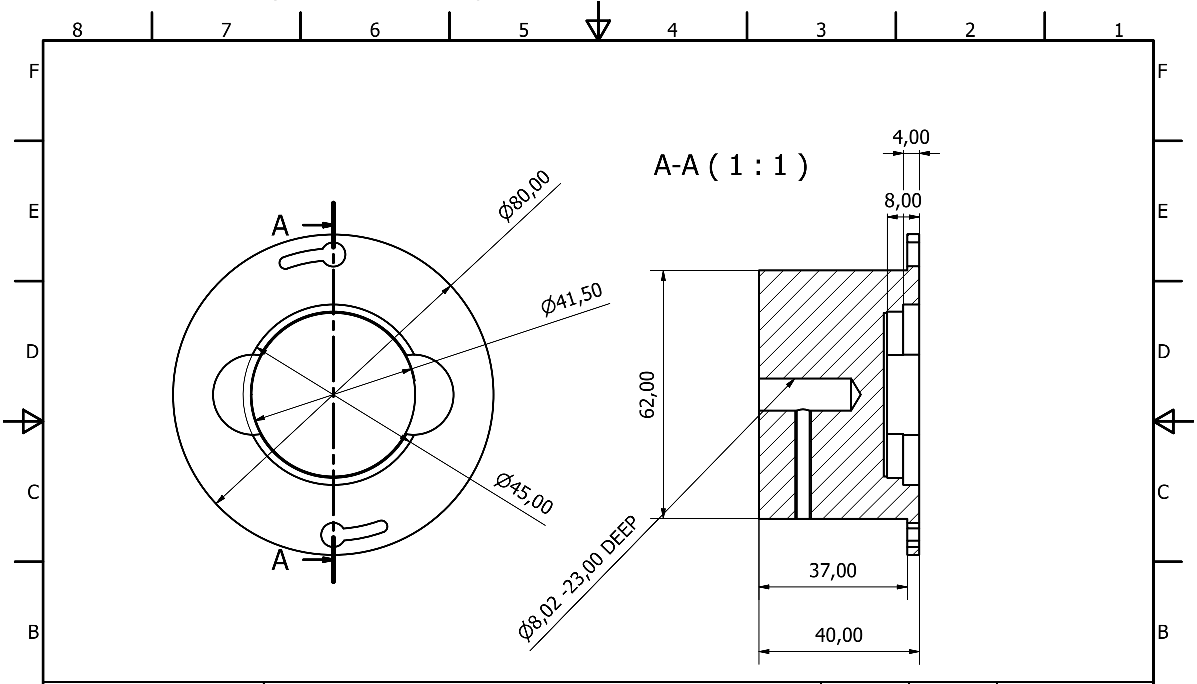

UNLESS OTHERWISE SPECIFIED: 1. DIMENSIONS ARE IN MILLIMETERS 2. DEBURB AND BREAK SHARP EDGES 3. FOR LINEAR DIM.: NS-ISO 2768-M 4. THREAD TOLERANCES: NS/ISO 965-1 5. ALL SURFACES SHALL BE MACHINED		PROJECT	DRAWN BY simekr	DATE 18.03.2021	UiO : Universitetet i Oslo	
		FILENAME sample_holder02.dwg	CHECKED BY	DATE	FORMAT 1 : 1	VIEW PLACEMENT
MATERIAL Aluminum 6061	MASS N/A	PATH Z:\Tegninger\KJEMI\Livsvitenskap\Irep Gözen\Sentrifuge\sample_holder02.dwg	APPROVED BY	DATE	REV	SHEET 1 of 2

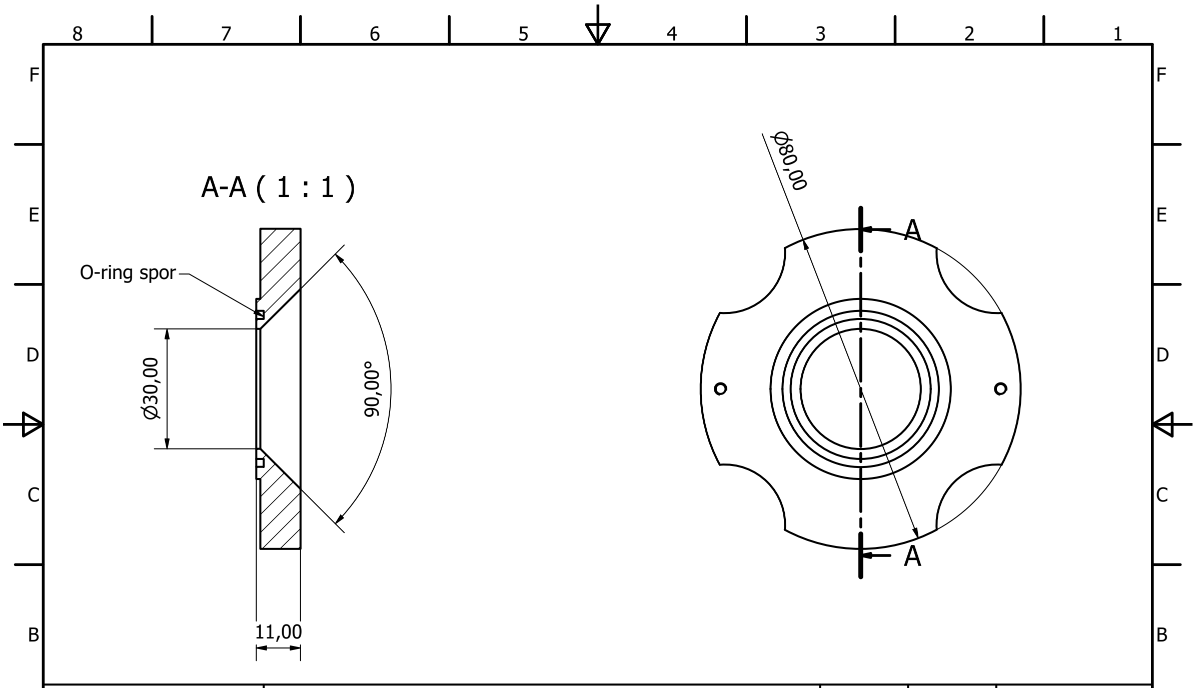

UNLESS OTHERWISE SPECIFIED: 1. DIMENSIONS ARE IN MILLIMETERS 2. DEBURB AND BREAK SHARP EDGES 3. FOR LINEAR DIM.: NS-ISO 2768-M 4. THREAD TOLERANCES: NS/ISO 965-1 5. ALL SURFACES SHALL BE MACHINED		PROJECT	DRAWN BY simekr	DATE 28.03.2022	UiO : Universitetet i Oslo	
		FILENAME sample_lid02.dwg	CHECKED BY	DATE	FORMAT 1 : 1	VIEW PLACEMENT
MATERIAL Aluminum 6061	MASS N/A	PATH Z:\Tegninger\KJEMI\Livsvitenskap\Irep Gözen\Sentrifuge\Bilder\sample_lid02.dwg	APPROVED BY	DATE	REV	SHEET 1 of 2

PARTS LIST

ITEM	QTY	PART NUMBER
1	4	alu profil2
2	2	alu profil
3	2	alu profil3
4	8	aluprofil_hjørne2
5	2	alu profil3-2
6	2	alu profil-2
8	1	sideplate2-top
11	1	Stepmotor kontrolpanel
23	1	sample_holder02
25	1	sample_lid02

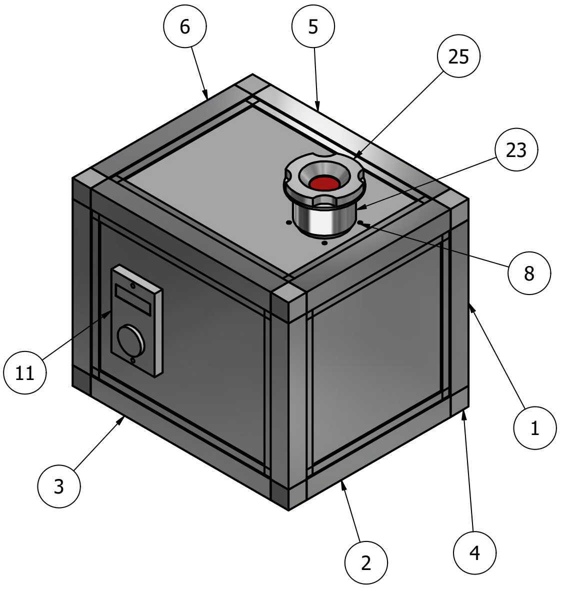

UNLESS OTHERWISE SPECIFIED:
1. DIMENSIONS ARE IN MILLIMETERS
2. DEBURB AND BREAK SHARP EDGES
3. FOR LINEAR DIM.: NS-ISO 2768-M
4. THREAD TOLERANCES: NS/ISO 965-1
5. ALL SURFACES SHALL BE MACHINED

PROJECT		DRAWN BY simekr	DATE 07.04.2021	UiO : Universitetet i Oslo	
FILENAME sentrifugeboks.dwg		CHECKED BY	DATE	FORMAT 1 : 4	VIEW PLACEMENT
MATERIAL	MASS N/A	PATH Z:\Tegninger\KJEMI\Livsvitenskap\Irep Gözen\Sentrifuge\sentrifugeboks.dwg	APPROVED BY	DATE	REV	SHEET 1 of 1

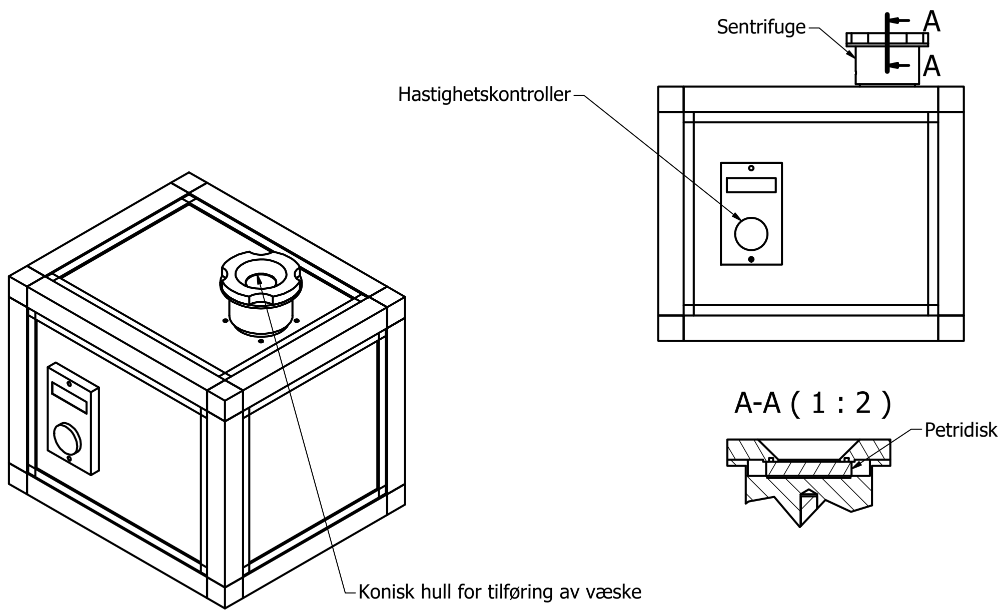

UNLESS OTHERWISE SPECIFIED:
1. DIMENSIONS ARE IN MILLIMETERS
2. DEBURB AND BREAK SHARP EDGES
3. FOR LINEAR DIM.: NS-ISO 2768-M
4. THREAD TOLERANCES: NS/ISO 965-1
5. ALL SURFACES SHALL BE MACHINED

PROJECT		DRAWN BY simekr	DATE 28.03.2022	UiO : Universitetet i Oslo	
FILENAME spinninginstrument.dwg		CHECKED BY	DATE	FORMAT 1 : 4	VIEW PLACEMENT
MATERIAL	MASS N/A	PATH Z:\Tegninger\KJEMI\Livsvitenskap\Irep Gözen\Sentrifuge\Bilder\spinninginstrument.dwg	APPROVED BY	DATE	REV	SHEET 1 of 2